VISUALIZING ZINC DYNAMICS IN CELL DIVISION AND DEVELOPING ZEBRAFISH

A Dissertation
Presented to
The Academic Faculty

by

Daisy M. Bourassa

In Partial Fulfillment
of the Requirements for the Degree
Doctor of Philosophy in the
School of Chemistry and Biochemistry

Georgia Institute of Technology
May 2016

VISUALIZING ZINC DYNAMICS IN CELL DIVISION

AND DEVELOPING ZEBRAFISH

Approved by:

Dr. Christoph Fahrni, Advisor
School of Chemistry and Biochemistry
Georgia Institute of Technology

Dr. Amit Reddi
School of Chemistry and Biochemistry
Georgia Institute of Technology

Dr. Raquel Lieberman
School of Chemistry and Biochemistry
Georgia Institute of Technology

Dr. Chong Shin
School of Biology
Georgia Institute of Technology

Dr. Julia Kubanek
School of Chemistry and Biochemistry
Georgia Institute of Technology

Date Approved: March 23, 2016

In memory of my father, Bob Marsden

ACKNOWLEDGEMENTS

First and foremost, I would like to thank my advisor, Dr. Christoph Fahrni. I am deeply grateful for his mentorship, guidance, and support. I am thankful for him pushing for me to do my best, allowing me to make mistakes and always being there for guidance when I am lost.

To mother and father who have always been my biggest fans. Thank you for always believing in me. You are my number one motivation. I can not take any credit for where I am today without acknowledging you. I am where I am because of your love and support.

I am extremely grateful for my committee members, Dr. Chong Shin, Dr. Raquel Lieberman, Dr. Julia Kubanek and Dr. Amit Reddi. Thank you for all the advice, conversations, last minute speech introductions, interviews about teaching careers, etc. I am deeply appreciative of the time you have all given to help me succeed in my goals.

Thank you to all of the Fahrni Lab members, past and present. Dr. Reagan McRae, Dr. Thomas Morgan and Dr. Pritha Bagchi: I have admired you all for your hard work, dedication, and passion to help others. Pritha, you are such and inspiration and I miss you terribly! Adam McCallum, you have kept me sane amongst the chaos! Thank you for always being there for me.

To my Agnes Scott family: MK, Anna, Senam and Chinyere. You all mean so much to me. I love my job at Agnes and its because I get to work with some of the most inspirational people I have ever met! To my best friend Jonna: as I always say, thank you for teaching me what it means to be an amazing friend. To my best friend Jill: Thank you for always being there for me. No matter what. No questions asked. I can always count on you. To my Simmons Sisters: Necy, Jai-me, Jen Bento, Melissa, Andrea, Anne Marie, Liz, and Libby, I love and miss you all! To Leah and Stephanie: I always know I can count on you girls, thank you for always being there!

And last but certainly not least, thank you Matt Dowd for everything. Words can not express how much you mean to me. Thank you for always supporting me even when my life gets a little crazy, I always have you to to calm the storm. Thank you doesn't cover how grateful I am to have you in my life. I can not take credit for being where I am to day without all the love and support I have always had around me. I am very lucky to have such amazing friends and family. Thank you all from the bottom of my heart!

TABLE OF CONTENTS

Page

LIST OF TABLES

Page

LIST OF SCHEMES

Page

LIST OF FIGURES

Page

LIST OF SYMBOLS AND ABBREVIATIONS

ADH	Alcohol dehydrogenase
ANL	Argonne National Lab
at	Atrium
bv	Blood vessels
cb	Cerebellum
CPA	Carboxypeptidase A
dc	Diencephalon
dpf	Days post fertilization
DTDP	2,2′-Dithiodipyridine
EDS	Electron-probe energy-dispersive spectroscopy
EDTA	Ethylenediaminetetraacetic acid
Egr1	Early growth response 1
EPICS	Experimental Physics and Industrial Control System
ER	Endoplasmic reticulum
ESPT	Excited-state proton transfer
f	Fractional saturation
FBP	Filtered back projection
FP	Fluorescent proteins
FRET	Förster Resonance Energy Transfer
fv	Fourth ventricle
H_2O_2	Hydrogen peroxide
hb	Hindbrain
hpf	Hours post fertilization

hy	Hypothalamus
I	Intensity
IGF-I	Insulin-like growth factor-1
K	Stability constant
K-B	Kirkpatrick-Baez mirror optics
K4M	Type of Lowicryl resin used to embed zebrafish embryos
K_d	Dissociation constant
l	Pathlength
LA-ICP-MS	Laser ablation inductively coupled plasma mass spectrometry
le	Lens
lv	Liver
mc	Mesencephalon
MLEM	Maximum likelihood expectation maximization
mo	Medulla oblongata
MT	Metallothionein
mt	Myotome
my	Myelencephalon
nc	Notochord
NIH 3T3	Mouse fibroblasts
nt	Neural tube
P	Probe
Pc	Pericardial cavity
PC12	Rat pheochromacytoma cells
PCC	Pearson's correlation coefficient
PIXE	Proton beam microprobe – particle induced X-ray emission
PLT	Progressive lowering of temperature methods.

PMMA	Polymethyl methacrylate
R	Ratio
R_{max}	Maximum fluorescence intensity
R_{min}	Minimum fluorescence intensity
Ram-Lak	Ramachandran-Lakshminarayanan
rc	Rhombencephalon
rt	Retina
sc	Spinal chord
SIMS	Secondary ion mass spectrometry
SXRF	Synchrotron X-ray fluorescence
T	Thionein, the apo-form of Metallothionein
tc	Telencephalon
tl	Tail
TPA	Two-photon absorption
TPEM	Two-photon excitation microscopy
TPEN	N,N,N',N'-tetrakis-(2-pyridylmethyl)-ethylenediamine
tv	Third ventricle
X-ray CT	X-ray computed tomography
ye	Yolk extension
yo	Yolk
ysl	Yolk syncytial layer
μ_{em}	Linear attenuation coefficient for the emission
μ_{ex}	Linear attenuation coefficient for the excitation

SUMMARY

The importance of zinc for cellular proliferation and growth is well established.[1] As the maternally derived yolk stores are the primary source of nutrients for the embryo, this pool supplies all developing tissues and organs with zinc, likely orchestrated through an elaborate network of zinc transporters.[2] On a cellular level, at the onset of mitosis there is a 2 to 3-fold increase of zinc in a cell,[3] this too must be facilitated through a regulatory process. In summary, this thesis is about gaining a basic understanding of zinc distribution in two key biological events, cell division and embryogenesis. Where is the zinc and what is the best way to observe and measure the zinc in a biologically relevant manner?

Chapter 1 summarizes the current knowledge surrounding the properties and functions of zinc in nature. This chapter also reviews the vital need of zinc in cell division and cell proliferation as well as outlines the overall approach presented this thesis.

Chapter 2 investigates labile zinc in live NIH 3T3 fibroblasts using a newly developed Zn(II)-selective ratiometric probe capable of two-photon excitation. Cells are monitor during mitosis, thorough characterization of the probe is presented, and fluorescent organelle markers are used to identify localization of labile Zn(II).

Chapter 3 utilizes synchrotron X-ray fluorescence (SXRF) microtomography to image the distribution of zinc, iron and copper with 2 – 3 μm resolution of zebrafish embryos in the pharyngula and hatching periods, approximately 24 and 48 hours post fertilization.[4]

Chapter 4 investigates the distribution of labile zinc during the first 24 hours of zebrafish embryogenesis. Live, real time imaging is used to image labile Zn(II) dynamics and high resolution imaging stacks are acquired on fixed embryos to acquire greater detail in a specific point of development.

Chapter 5 provides conclusions and possible future directions this work may one day lead to.

1. MacDonald, R.S. The role of zinc in growth and cell proliferation. *Journal of Nutrition* **130**, 1500S-1508S (2000).

2. Ho, E., Dukovcic, S., Hobson, B., Wong, C.P., Miller, G., Hardin, K., Traber, M.G. & Tanguay, R.L. Zinc transporter expression in zebrafish (Danio rerio) during development. *Comparative Biochemistry and Physiology C-Toxicology & Pharmacology* **155**, 26-32 (2012).

3. McRae, R., Lai, B. & Fahrni, C.J. Subcellular redistribution and mitotic inheritance of transition metals in proliferating mouse fibroblast cells. *Metallomics* **5**, 52-61 (2013).

4. Bourassa, D., Gleber, S.C., Vogt, S., Yi, H., Will, F., Richter, H., Shin, C.H. & Fahrni, C.J. 3D imaging of transition metals in the zebrafish embryo by X-ray fluorescence microtomography. *Metallomics* **6**, 1648-1655 (2014).

CHAPTER 1

INTRODUCTION

1.1 Importance of Zinc in Biology

Zinc is an essential micronutrient required in all forms of life. After iron, it is the second most abundant biologically important trace element.[1] A bioinformatics study of the human genome published in 2006 predicted that roughly 10% of the proteome binds zinc with significant affinity.[2] Generally, the concentration of the total cellular Zn(II) in mammalian cells ranges between 0.1-0.5 mM.[3] Zinc is not only abundant, but indispensable in many cellular processes, affecting cell proliferation,[4,5] cell differentiation,[6,7] growth[5,8] and development.[9,10]

As a transition metal, zinc belongs to the d-block elements in the periodic chart. Unlike other divalent first-row transition metals, Zn(II) has a full d^{10} electron configuration rendering the metal cation redox inactive.[11] The ability of Zn(II) to catalyze reactions relies on its Lewis acid properties, which are utilized in numerous enzymes for the activation of substrates.[1,11] Due to the lack of ligand field stabilization energy, a consequence of the d^{10} electron configuration, Zn(II) offers a flexible coordination sphere with coordination numbers ranging from 4 to 6, and adopts tetrahedral, trigonal bipyramidal, or octahedral geometries.[12] Given the inherent flexibility of its coordination preferences, Zn(II) readily forms stable complexes with a wide range of ligands. This property has been exploited by nature for stabilizing protein folds such as zinc-finger motifs found in many transcription factors. In conjunction with its Lewis acid properties, Zn(II) acts as a co-factor in many enzymes where it can readily accommodate changes in coordination occurring in the course of a catalytic cycle. Overall, the versatility of Zn(II) allows for three main categories of primary functions in biology: as a structural support of protein folds, a Lewis acid catalyst, and a second messenger in signaling processes.[1]

1.1.1 A Structural Component

Structural zinc binding sites utilize Zn(II) to maintain and increase the stability of a wide range of proteins. Over 20% of zinc enzymes use zinc for structural purposes.[13] These binding sites typically consist of four protein ligands and a tetrahedral Zn(II) center devoid of coordinating water molecules.[14] Cysteine and histidine side chains are the first and second most common ligands, respectively, in a structural zinc binding site.[14] A classic example of a structural zinc binding site is found in alcohol dehydrogenase (ADH), a family of enzymes responsible for the reversible oxidation of alcohols in a variety of biochemical reactions such as the conversion of retinol to retinal in the vision cycle.[15] In this structural binding site, four cysteines of alcohol dehydrogenase bind to zinc to yield a tetrahedral coordination geometry.[12] In addition to the structural zinc site, ADH contains a Zn(II) center in the active site where it plays a critical role in substrate binding and catalytic activity of the enzyme.

Zinc also has a structural role in maintaining the stability of zinc fingers, a common protein domain characterized by a tetrahedral Zn(II) binding site composed of two cysteine and two histidine residues. Although the structure of these small proteins varies widely, classic zinc fingers are characterized by their DNA binding properties, a chain length of roughly 30 amino acids, and a compact zinc binding site surrounded by an α-helix and β-sheet in a "$\beta\beta\alpha$" fold.[16,17] The functions of zinc fingers are diverse and include DNA replication and repair, RNA packaging, activation of transcription, protein folding, and regulation of cell proliferation and apoptosis.[18,19]

1.1.2 A Catalytic Cofactor

Zinc is a catalytic component of over 60% of known zinc-containing proteins. In six main enzyme classes: hydrolases, transferases, oxidoreductase, lyases, ligases and

isomerases, zinc acts as a cofactor.[1,13] In hydrolases, the catalytic zinc site creates a hydroxide anion by lowering the pK_a of a coordinated water molecule, thus facilitating nucleophilic attack on the substrate.[11,13] One example of a zinc-hydrolase is the mononuclear metalloprotease, carboxypeptidase A (CPA).[20] The zinc binding site is located inside this globular protein and contains two histidines, one glutamic acid, and a water molecule.[13] The catalytic mechanism of CPA is classified as an induced-fit model. As the substrate enters the active site, the globular protein closes around it, forcing the substrate into place for hydrolysis aided by the zinc ion and water molecule. The significant change in shape of the CPA active site demonstrates zinc's inherent flexibility of coordination.

ADH, previously mentioned for its use of Zn(II) as a structural component, also contains a Zn(II) center in the active site where it plays a critical role in substrate binding and catalytic activity of this oxidoreductase. Binding of the coenzyme (NAD^+/NADH) induces a conformational change that adjusts the structure of the catalytic zinc site.[21] In this reaction the function of the metal ion differs between the forward and reverse processes. Whereas the activation of an aldehyde for the transfer of a hydride ion requires what Maret et al. refer to as an "electron pull", the activation of the alcohol requires an "electron push".[22] These transitions induce changes of both the geometry and coordination number of the catalytic zinc ion.[23]

1.1.3 A Second Messenger in Signaling Pathways

In addition to its structural and catalytic roles Zn(II) can also act as an extracellular or intracellular signaling mediator, allowing communication to occur between cells in an autocrine, paracrine, or endocrine manner.[24] Zinc signaling is the product of alterations in both intracellular and extracellular zinc concentrations. Some of the first zinc-secreting cells to be characterized were the insulin-secreting cells of the pancreas.[25] In this example

glucose stimuli activate the co-release of zinc and insulin from pancreatic β cells, which can then suppress hepatic insulin and reduce insulin secretion.[26-28] In the central nervous system, Zn(II) ions are released from presynaptic neurons into the synaptic cleft upon membrane depolarization and are believed to modulate synaptic transmission by binding to different transporters and receptor channels on postsynaptic neurons.[25]

Zinc signaling has often been compared to the well-researched calcium signaling. Frederickson et al. even referred to zinc signaling as "the calcium of the 21st century".[25] Similar to calcium, zinc appears to play an important role as an ionic signal in the brain. All calcium channels have some level of zinc permeability, thus allowing the passage of Zn(II) ions through otherwise gated membranes.[25,29,30] As with calcium, an excess of extracellular Zn(II) ions in brain tissue, a condition induced by seizures, can be highly toxic. This is due in part to the ability of Zn(II) to bind and inhibit glyceraldehyde-3-phosphate, an intermediate in several metabolic pathways designed to supply glucose to the brain.[25,31]

1.2 Regulation of Zinc

Given its central role in many fundamental biological processes, it is not surprising that cellular zinc concentrations are tightly controlled and regulated through a sophisticated network of zinc transporters and metalloproteins[32,33] (Figure 1.1). Two families of zinc transporters, the ZIP (Zrt-, Irt- like protein, SLC39A) and ZnT (SLC30A) proteins, are key components of the homeostatic machinery. The ZIP family of proteins is responsible for transporting Zn(II) from the extracellular space or lumen of organelles into the cytosol. Conversely, the ZnT family is responsible for transporting Zn(II) from the cytosol into intracellular organelles or the extracellular space.[3] Additionally, metallothioneins can bind seven Zn(II) ions per protein and appear to be a critical contributors to zinc homeostasis.[34]

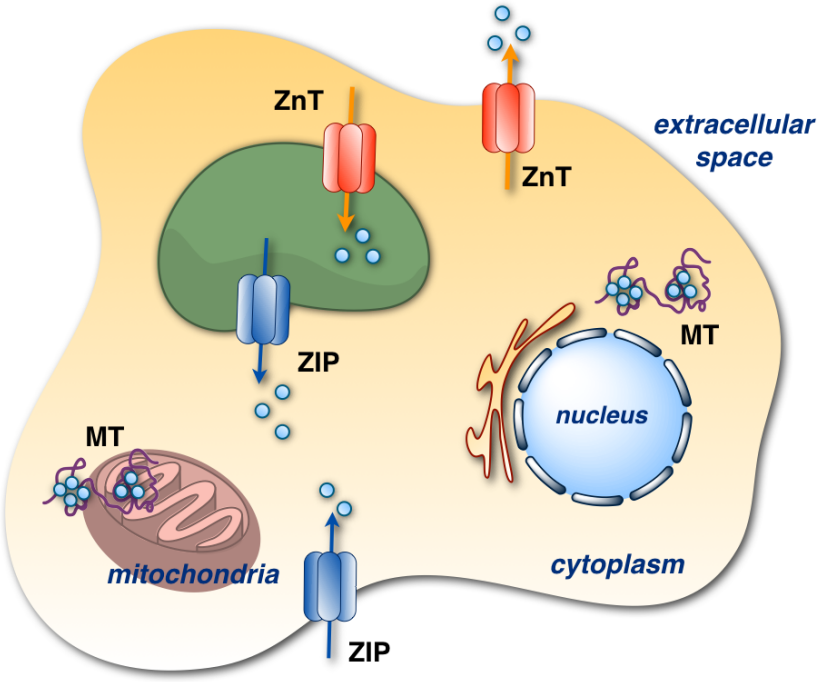

Figure 1.1: Distribution of zinc transporters. The ZIP family (blue arrows) is responsible for transporting Zn(II) into the cytosol and the ZnT family (red arrows) is responsible for transporting Zn(II) out of the cytosol.[3] Seven zinc ions bind to metallothionein (MT) found in the mitochondria, cytosol or nucleus.

1.2.1 Zinc Transporters: ZIP Family

There are currently 14 members of the ZIP family identified in humans, characterized by 8 transmembrane domains and a long, variable loop between domains 3 and 4 that frequently contains a histidine-rich sequence (Figure 1.2A). The function of the variable loop and the mechanism of zinc transport is unclear.[35] The highly conserved sequence of domain 4 is predicted to form an amphipathic helix with a conserved histidine residue. It is possible this region forms an intramembranous metal binding site where metals can pass.[35,36]

Many ZIP transporters have been implicated in diseases. A major focus has been placed on the LIV-1 family of ZIP proteins and the role it may have in breast cancer.[37-43]

Although all nine human LIV-1 family members have been investigated, ZIP6, ZIP7, ZIP10 and ZIP14 appear to certainly have a connection with the disease and saturate the literature in this area.[38-46] For example, ZIP7 is known to promote an aggressive phenotype in breast cancer cells and elevated expression of ZIP6 is associated with invasive, metastatic cancer progression.[46,47]

1.2.2 Zinc Transporters: ZnT Family

In contrast to the ZIP transporters, the ZnT family transports zinc from the cytoplasm into organelles or the extracellular space. These proteins are predicted to have 6 transmembrane domains with a long, variable loop between domains 4 and 5 (Figure 1.2B). Similar to the ZIP proteins, this loop also contains a histidine-rich sequence.[48] Nine ZnT transporters have been identified and characterized.[36,48] Of these nine proteins, the ZnT8 protein has been extensively researched and is classified as a pancreatic β cell-specific zinc transporter.[49,50]

ZnT8 is expressed in the hormone producing pancreatic islet cells 2-3 fold higher than all other tissue examined.[51] The elevated ZnT8 transports zinc into insulin-containing granules in islet β cells where insulin is stored as a hexamer bound with two zinc ions before secretion.[26,28] As mentioned in the Section 1.1.3, zinc and insulin are co-released from pancreatic β cells, which can then lead to the suppression of hepatic insulin and reduction of insulin secretion from the cells.[26-28] While the majority of research in this area agrees that the loss of ZnT8 function may increase the susceptibility to type 2 diabetes,[26,49,51] recent studies of genotyping and sequencing approximately 150,000 individuals report the identification of 12 rare ZnT8 variants that reduced the risk of type 2 diabetes by 65%.[27,52]

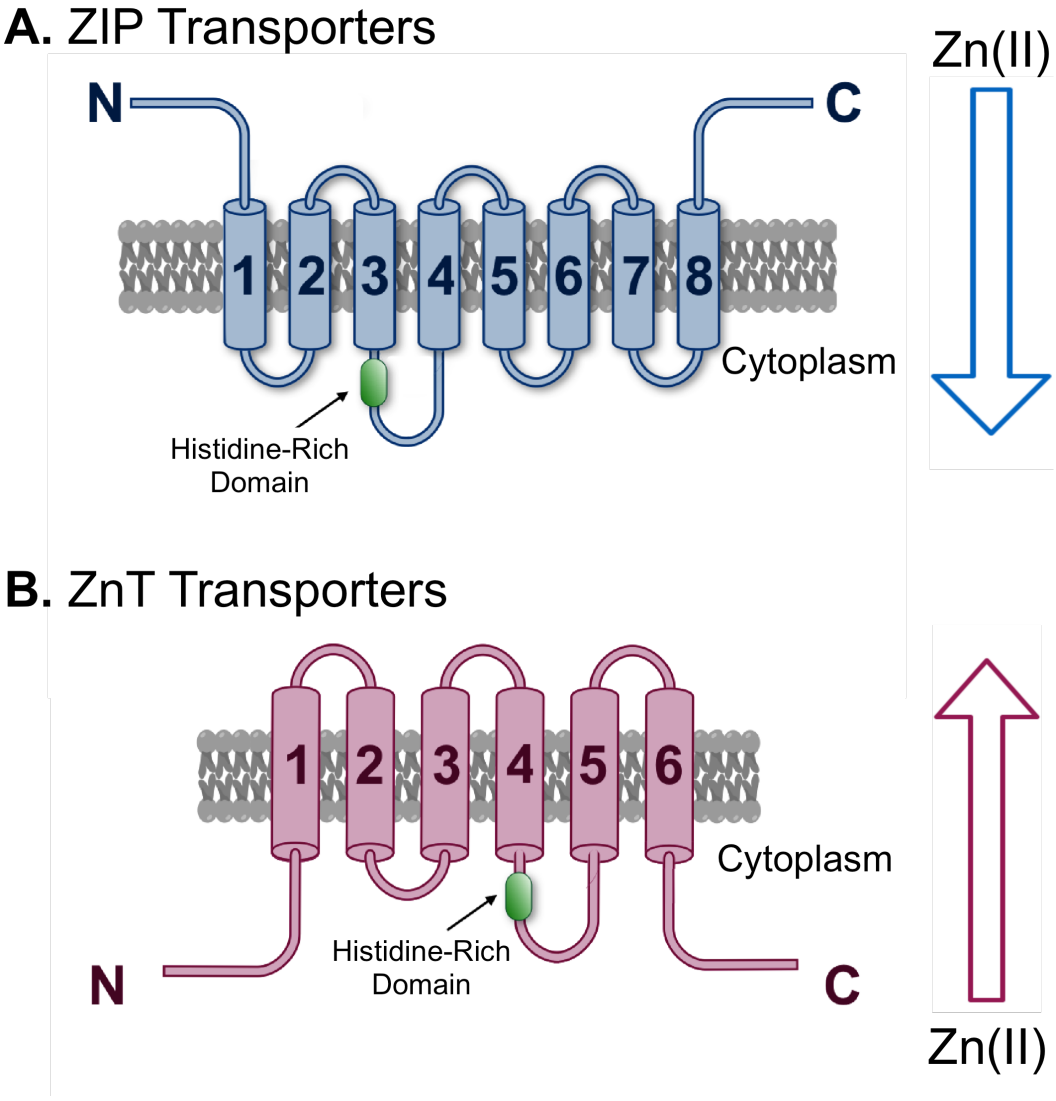

Figure 1.2: Predicted membrane topologies of ZIP and ZnT zinc transporters. **A**. ZIP (SLC39) transporters have eight predicted transmembrane domains (TMDs) and a large histidine-rich domain between TMD3 and TMD4. **B**. ZnT (SLC30) transporters have six predicted TMDs and a large histidine-rich domain between TMD4 and TMD5. The direction of Zn(II) flux in relation to the cytoplasm is illustrated on the right.

1.2.3 Zinc Regulation by Metallothioneins

In addition to the two families of zinc transporter proteins, the family of metal-binding proteins known as metallothioneins (MT) contribute to the absorption, secretion, and overall regulation of zinc ions.[53] The metal binding domain of MT contains 20 highly conserved cysteine residues with sulfhydryl groups capable of binding 7 moles of divalent zinc ions per mol of MT.[34,54,55] The apoprotein, thionein (T), has no defined secondary structure and relies on the binding of the seven zinc ions to shape the protein into a defined three dimensional structure.[56] MTs are primarily located in the cytoplasm and mitochondria; however, their location is regulated by the oxidative state of their environment.[34,57] During oxidative stress, MTs are rapidly translocated from the mitochondria to the nucleus where they are then oxidized and transported to the cytosol.[58] As a metal-trafficking protein, MT can transport zinc from the cytoplasm to the nucleus or the mitochondrial intermembrane space,[59] two intracellular locations for which there are no identified zinc transporters.[60] In addition to metal transport, MTs have been associated with a barrage of functions including metabolism regulation, angiogenesis, cell differentiation, apoptosis, and cell cycle regulation as well as metal storage, detoxification, and homeostasis.[34,53,56,61] With a capacity to bind seven Zn(II) ions simultaneously, MTs actively participate in zinc buffering and can serve as a major source of Zn(II) ions to other metalloproteins and transcription factors.[32,57,62]

1.3 Cell Proliferation

Cell proliferation is essential to many biological processes such as tissue repair, fertilization, embryogenesis, and growth. Although cell replication is intricately regulated in normal tissues, it is an irregular process during the progression of diseases such as cancer,[63] delayed wound healing,[64,65] and growth defects.[66,67] Because of the morbidity and mortality associated with these processes, there is an elevated interest in the

underlying mechanisms of cell cycle progression. Cell proliferation is a tightly controlled process leading to the duplication of cellular DNA and division of a single cell into two identical daughter cells. Cells can exist in either the resting phase, G_0, or the active phase. The replication of mammalian cells is a cyclic process where cells move from G_0 to the first gap phase, G_1, where they prepare for the synthesis phase, S, in which DNA is replicated, followed by the second gap phase, G_2, and finally the mitotic phase, M, in which the DNA separates into chromatids and the cell divides. The progression between phases is highly regulated, containing many "checkpoints" that are controlled by proteins known as cyclins.[68]

1.3.1 Zinc in Cell Proliferation

Zinc plays a direct role in cell cycle progression.[5,6] At the cellular level, zinc is required to progress from G_1 to S phase[69,70] and G_2 to M phase.[71,72] Furthermore, zinc is involved in the formation and function of chromatin,[73,74] transcription of DNA,[73,75] and gene expression.[76-78] For example, zinc is required to stabilize the DNA, RNA and ribosome structure.[75] Many enzymes necessary for DNA and RNA synthesis are also considered metalloenzymes such as RNA polymerase, transcription factor IIIA, and reverse transcriptase.[75] Zinc has been linked to multiple growth factors necessary for DNA synthesis including insulin-like growth factor-I (IGF-I)[79] and zinc deficiencies are reported to impair IGF-I-induced DNA synthesis.[80] Overall, DNA synthesis has been reported to decrease in zinc deficient conditions and increase in the presence of elevated zinc levels.

During cell proliferation, synthesis of the zinc-binding protein metallothionein (MT) is increased.[81] Similar to zinc,[82] MT concentrations are cell cycle dependent, peaking in cytoplasmic concentration during late G1 and G1/S phases.[83] MT has also demonstrated a role in regards to zinc regulation during the cell cycle.[34] Overall, it is suggested MT is a key component in cell proliferation and growth.

1.3.2 Changes in Zinc Levels as a Function of Cell Cycle

To monitor the intracellular Zn(II) concentrations throughout the cell cycle, Li et al. employed the Zn(II)-selective fluorescent probe, FluoZin-3, in synchronized rat pheochromacytoma (PC12) cells.[84] The data revealed cell-cycle dependent fluctuations of cytosolic Zn(II) concentrations, with a spike of Zn(II) during the early G_1 phase and a second at the late G_1/S phase.[84] More recently, McRae et al. investigated total trace metal distribution through various stages of mitosis by performing X-ray fluorescence microscopy (SXRF) studies on non-synchronized proliferating NIH 3T3 fibroblasts[82] (Figure 1.3). These data revealed a distinct redistribution pattern of zinc that was found to be spatially correlated with copper and sulfur densities but not phosphorous. During metaphase, two distinct high-density locations of zinc were found adjacent to the metaphase plate of the cell. The high-density regions of zinc, copper, and sulfur are then relocated to the center of the dividing cell during anaphase. Upon formation of the cleavage furrow, these central pools are divided into similar portions and distributed into the two daughter cells during telophase and cytokinesis.

In addition to the striking redistribution pattern, the data also revealed a 2 to 3-fold increase of zinc during mitosis. Specifically, interphase cells possess roughly 3-4 fmol of total zinc whereas mitotic cells were found to contain zinc levels between 8-10 fmol, implying an active import of zinc at the G2/M transition. These data indicate total zinc concentrations in interphase cells around 1.4–2 mM assuming an average volume of 2 pL for 3T3 cells in solution and an increase to 16-20 mM of total zinc throughout all mitotic stages during which the cell volume shrinks to approximately 0.5 pL.[85]

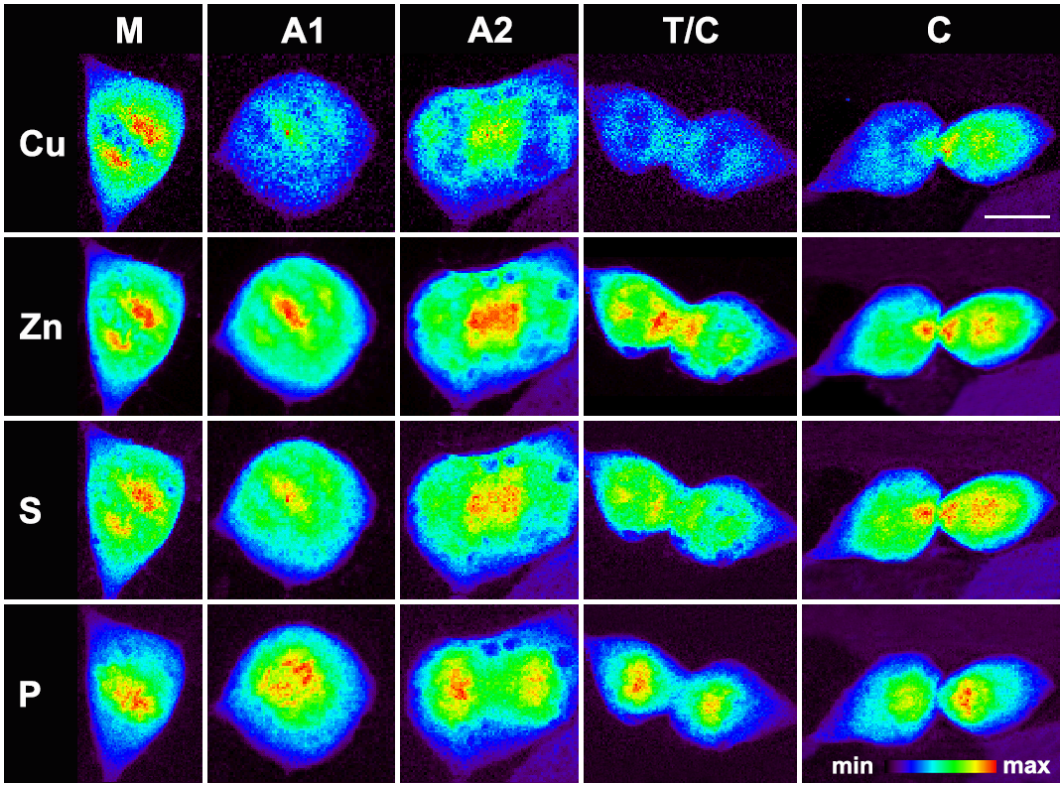

Figure 1.3: SXRF 2D sub-cellular distributions of transition metals. Copper (Cu), zinc (Zn), sulfur (S) and phosphorus (P) during select stages of mitosis: metaphase (M), anaphase part 1 (A1), anaphase part 2 (A2), telophase – cytokinesis (T/C), and cytokinesis (C). Scale bar = 20 μm.

1.4 Zinc in Pregnancy, Growth and Development

Zinc is a well-known vital nutrient during embryogenesis.[9,10,86] The effects of zinc deficiency on the growth and development of cells and whole organisms has been studied for over half of a century. For example, zinc deficiency in rats is estimated to adversely affect up to 90% of all implantation sites in utero and impacts the development of nearly all organ systems with the most extensive malformations found in neural tissue such as the brain and spinal cord.[87,88] Zinc deficiency has led to an array of teratogenic effects in animal models such as structural skeletal malformations, low birth weights, low survival rate, and soft tissue abnormalities.[88,89]

1.4.1 Zinc Requirements in Oocytes and Embryos

As intrinsic parts of embryogenesis, the development and fertilization of the female gamete are both zinc-dependent processes.[90-92] Regulatory fluxes referred to as “zinc sparks” are required in the meiotic cell cycle of a mammalian egg.[93,94] Using oocytes collected from the ovaries of adult mice, Kim et al. determined zinc to act as a key regulator of the oocyte-to-egg and egg-to-embryo transitions.[91] Control and zinc-insufficient oocytes were fertilized in vitro and monitored for development using 5-methylcytidine staining to detect methylated DNA. The absence of fluorescence in both embryos indicated successful fertilization; however, the control embryos advanced to the two-cell stage by 24 hours post fertilization (hpf) while the zinc-insufficient oocytes remained at the pro-nucleus stage immediately following fertilization. Continued observation revealed the control embryos reached the blastocyst stage at 120 hpf, but the zinc-insufficient group had only completed one round of cell division.[91] Therefore, although zinc deficient oocytes are capable of fertilization they are compromised and unable to progress efficiently in embryogenesis indicating zinc’s important role in oocyte development.

1.5 Thesis Objectives

The biological importance of zinc has been well established. It plays an indispensable role in a multitude of biological processes, either as a structural, catalytic, or signaling component. A sophisticated network of transporters controls zinc regulation tightly, and an imbalance in zinc homeostasis is linked to various diseases and abnormalities. Zinc deficiency results in the loss of cell proliferation leading to delayed wound healing, growth malformations, and pregnancy defects. Overall, the distribution and regulation of zinc ions is not trivial and involves high levels of specificity in order to maintain the numerous biological functions dependent on zinc. Visualizing zinc dynamics during processes such as cell division and embryogenesis is the first step towards understanding the cellular transport and control of zinc, which is in turn a prerequisite for a better understanding of the various cellular functions critical to life.

Many fundamental questions regarding zinc homeostasis during cell division and early embryonic development remain unanswered. What regions are associated with increased labile zinc or total zinc demand during different points of embryogenesis? To what extent does labile zinc correlate with total zinc in both single cells and developing embryos? Are subcellular areas with elevated labile zinc visible using a zinc-selective probe in live, dividing cells similar to that found in previous SXRF microscopy studies? Are labile zinc pools spatially correlated with identifiable organelles?

With these questions in mind, the aim of this thesis is to investigate the redistribution of zinc during cell proliferation and early embryonic development. Specifically, labile zinc pools of live NIH 3T3 fibroblasts were monitored using a newly developed Zn(II)-selective probe, Chromis1, and two-photon excited emission ratiometric imaging for the purpose of better understanding labile zinc dynamics on a cellular level. To elucidate the location of the labile pools, comparative fluorescent imaging of Chromis1 and fluorescent markers for mitochondria, lipid droplets and the endoplasmic reticulum

was performed. Additionally, live cell characterization of Chromis1 was a critical piece of this study in order to accurately analyze the data collected. To achieve this end, Chromis1 was evaluated in live cells under excessive exogenous Zn(II) levels, in the presence of a high-affinity chelator, and under oxidative stress in order to promote endogenous Zn(II) release from metalloproteins. Neutralization of Chromis1-treated cells was also performed to examine Chromis1 fluorescence emission response for signs of pH-dependency.

For a further understanding of metal distribution and dynamics in a developing organism, zebrafish embryos were used in both SXRF tomography and live fluorescent imaging experiments. SXRF provides insight into the location of total zinc, iron, and copper in a specimen, thus revealing the areas of high or low metal content during a stage in development. This information may identify particular locations or specific organs with higher demands for these trace nutrients during embryogenesis, which in turn may lead to a better understanding of the development and regulation of function for these particular anatomical structures. Lastly, this work investigates labile zinc dynamics of a developing zebrafish embryo during the first 24 hours of embryogenesis. Complementary to the information gained in SXRF tomography, these data will also contribute to a better understanding of zinc distribution in development. Together, the information collected in this research will provide a clearer picture of zinc distribution in a single cell and throughout embryogenesis.

1.6 Literature Cited

1. Kambe, T., Tsuji, T., Hashimoto, A. & Itsumura, N. The physiological, biochemical, and molecular roles of zinc transporters in zinc homeostasis and metabolism. *Physiological Reviews* **95**, 749-784 (2015).

2. Andreini, C., Banci, L., Bertini, I. & Rosato, A. Counting the zinc-proteins encoded in the human genome. *Journal of Proteome Research* **5**, 196-201 (2006).

3. Eide, D.J. Zinc transporters and the cellular trafficking of zinc. *Biochimica Et Biophysica Acta-Molecular Cell Research* **1763**, 711-722 (2006).

4. Falchuk, K.H., Fawcett, D.W. & Vallee, B.L. Role of zinc in cell-division of Euglena-Gracilis. *Journal of Cell Science* **17**, 57-78 (1975).

5. MacDonald, R.S. The role of zinc in growth and cell proliferation. *Journal of Nutrition* **130**, 1500S-1508S (2000).

6. Beyersmann, D. & Haase, H. Functions of zinc in signaling, proliferation and differentiation of mammalian cells. *Biometals* **14**, 331-341 (2001).

7. Cohen, L., Sekler, I. & Hershfinkel, M. The zinc sensing receptor, ZnR/GPR39, controls proliferation and differentiation of colonocytes and thereby tight junction formation in the colon. *Cell Death & Disease* **5**(2014).

8. Plum, L.M., Rink, L. & Haase, H. The essential toxin: Impact of zinc on human health. *International Journal of Environmental Research and Public Health* **7**, 1342-1365 (2010).

9. Terrin, G., Canani, R.B., Di Chiara, M., Pietravalle, A., Aleandri, V., Conte, F. & De Curtis, M. Zinc in early life: A key element in the fetus and preterm neonate. *Nutrients* **7**, 10427-10446 (2015).

10. Dreosti, I.E., Record, I.R. & Manuel, S.J. Zinc deficiency and the developing embryo. *Biological Trace Element Research* **7**, 103-122 (1985).

11. Hernick, M. & Fierke, C.A. Zinc hydrolases: The mechanisms of zinc-dependent deacetylases. *Archives of Biochemistry and Biophysics* **433**, 71-84 (2005).

12. Holm, R.H., Kennepohl, P. & Solomon, E.I. Structural and functional aspects of metal sites in biology. *Chemical Reviews* **96**, 2239-2314 (1996).

13. Andreini, C. & Bertini, I. A bioinformatics view of zinc enzymes. *Journal of Inorganic Biochemistry* **111**, 150-156 (2012).

14. Auld, D.S. Zinc coordination sphere in biochemical zinc sites. *Biometals* **14**, 271-313 (2001).

15. Christian, P. & West, K.P. Interactions between zinc and vitamin A: An update. *American Journal of Clinical Nutrition* **68**, 435S-441S (1998).

16. Vallee, B.L., Coleman, J.E. & Auld, D.S. Zinc fingers, zinc clusters, and zinc twists in DNA-bonding protein domains. *Proceedings of the National Academy of Sciences of the United States of America* **88**, 999-1003 (1991).

17. Malgieri, G., Palmieri, M., Russo, L., Fattorusso, R., Pedone, P.V. & Isernia, C. The prokaryotic zinc-finger: Structure, function and comparison with the eukaryotic counterpart. *Febs Journal* **282**, 4480-4496 (2015).

18. Krishna, S.S., Majumdar, I. & Grishin, N.V. Structural classification of zinc fingers. *Nucleic Acids Research* **31**, 532-550 (2003).

19. Laity, J.H., Lee, B.M. & Wright, P.E. Zinc finger proteins: New insights into structural and functional diversity. *Current Opinion in Structural Biology* **11**, 39-46 (2001).

20. Christianson, D.W. & Lipscomb, W.N. Carboxypeptidase-A. *Accounts of Chemical Research* **22**, 62-69 (1989).

21. Maret, W. & Zeppezauer, M. Influence of anions and pH on the conformational change of horse liver alcohol-dehydrogenase induced by binding of oxidized nicotinamide adenine-dinucleotide binding of chloride to the catalytic metal-ion. *Biochemistry* **25**, 1584-1588 (1986).

22. Maret, W. & Li, Y. Coordination dynamics of zinc in proteins. *Chemical Reviews* **109**, 4682-4707 (2009).

23. Maret, W. & Makinen, M.W. The pH variation of steady-state kinetic-parameters of site-specific CO2+-reconstituted liver alcohol-dehydrogenase - a mechanistic probe for the assignment of metal-linked ionizations. *Journal of Biological Chemistry* **266**, 20636-20644 (1991).

24. Kambe, T. Introduction: "Zinc Signaling" - The Blossoming Field of Zinc Biology. in *Zinc Signals in Cellular Functions and Disorders* (eds. Fukada, T. & Kambe, T.) 1-5 (Springer, Tokyo, 2014).

25. Frederickson, C.J., Koh, J.Y. & Bush, A.I. The neurobiology of zinc in health and disease. *Nature Reviews Neuroscience* **6**, 449-462 (2005).

26. Tamaki, M., Fujitani, Y., Hara, A., Uchida, T., Tamura, Y., Takeno, K., Kawaguchi, M., Watanabe, T., Ogihara, T., Fukunaka, A., Shimizu, T., Mita, T., Kanazawa, A., Imaizumi, M.O., Abe, T., Kiyonari, H., Hojyo, S., Fukada, T., Kawauchi, T., Nagamatsu, S., Hirano, T., Kawamori, R. & Watada, H. The diabetes-susceptible gene SLC30A8/ZnT8 regulates hepatic insulin clearance. *Journal of Clinical Investigation* **123**, 4513-4524 (2013).

27. Myers, S.A. Zinc transporters and zinc signaling: New insights into their role in type 2 diabetes. *International Journal of Endocrinology* (2015).

28. Fujitani, Y., Tamaki, M., Fukunaka, A. & Watada, H. Zinc and its role in the pathogenesis of type 2 diabetes. in *Zinc Signals in Cellular Functions and Disorders* (eds. Fukada, T. & Kambe, T.) 269 - 283 (Springer, Tokyo, 2014).

29. Weiss, J.H., Sensi, S.L. & Koh, J.Y. Zn2+: A novel ionic mediator of neural injury in brain disease. *Trends in Pharmacological Sciences* **21**, 395-401 (2000).

30. Sensi, S.L., Yin, H.Z. & Weiss, J.H. AMPA/kainate receptor-triggered Zn2+ entry into cortical neurons induces mitochondrial Zn2+ uptake and persistent mitochondrial dysfunction. *European Journal of Neuroscience* **12**, 3813-3818 (2000).

31. Choi, D.W. & Koh, J.Y. Zinc and brain injury. *Annual Review of Neuroscience* **21**, 347-375 (1998).

32. Fukada, T., Yamasaki, S., Nishida, K., Murakami, M. & Hirano, T. Zinc homeostasis and signaling in health and diseases: Zinc signaling. *J. Biol. Inorg. Chem.* **16**, 1123-34 (2011).

33. Lichten, L.A. & Cousins, R.J. Mammalian zinc transporters: Nutritional and physiologic regulation. *Annual Review of Nutrition* **29**, 153-176 (2009).

34. Babula, P., Masarik, M., Adam, V., Eckschlager, T., Stiborova, M., Trnkova, L., Skutkova, H., Provaznik, I., Hubalek, J. & Kizek, R. Mammalian metallothioneins: Properties and functions. *Metallomics* **4**, 739-750 (2012).

35. Guerinot, M.L. The ZIP family of metal transporters. *Biochimica Et Biophysica Acta-Biomembranes* **1465**, 190-198 (2000).

36. Lichten, L.A. & Cousins, R.J. Mammalian zinc transporters: nutritional and physiologic regulation. *Annu. Rev. Nutr.* **29**, 153-76 (2009).

37. Taylor, K., Gee, J. & Kille, P. Zinc and cancer. *Zinc in Human Health* **76**, 283-304 (2011).

38. Levenson, C.W. & Somers, R.C. Nutritionally regulated biomarkers for breast cancer. *Nutrition Reviews* **66**, 163-166 (2008).

39. Taylor, K.M. LIV-1 breast cancer protein belongs to new family of histidine-rich membrane proteins with potential to control intracellular Zn2+ homeostasis. *IUBMB Life* **49**, 249-253 (2000).

40. Taylor, K.M., Hadley, L.J. & Nicholson, R.I. The LIV-1 gene, implicated in metastatic breast cancer, codes for a histidine-rich transmembrane protein. *British Journal of Cancer* **80**, 24-24 (1999).

41. Taylor, K.M., Morgan, H.E., Johnson, A., Hadley, L.J. & Nicholson, R.I. Structure-function analysis of LIV-1, the breast cancer-associated protein that belongs to a new subfamily of zinc transporters. *Biochemical Journal* **375**, 51-59 (2003).

42. Taylor, K.M., Morgan, H.E., Smart, K., Zahari, N.M., Pumford, S., Ellis, I.O., Robertson, J.F.R. & Nicholson, R.I. The emerging role of the LIV-1 subfamily of zinc transporters in breast cancer. *Molecular Medicine* **13**, 396-406 (2007).

43. Taylor, K.M. A distinct role in breast cancer for two LIV-1 family zinc transporters. *Biochemical Society Transactions* **36**, 1247-1251 (2008).

44. Taylor, K.M., Vichova, P., Jordan, N., Hiscox, S., Hendley, R. & Nicholson, R.I. ZIP7-mediated intracellular zinc transport contributes to aberrant growth factor signaling in antihormone-resistant breast cancer cells. *Endocrinology* **149**, 4912-4920 (2008).

45. Taylor, K.M. & Nicholson, R.I. The LZT proteins; the LIV-1 subfamily of zinc transporters. *Biochimica Et Biophysica Acta-Biomembranes* **1611**, 16-30 (2003).

46. Hogstrand, C., Kille, P., Ackland, M.L., Hiscox, S. & Taylor, K.M. A mechanism for epithelial-mesenchymal transition and anoikis resistance in breast cancer triggered by zinc channel ZIP6 and STAT3 (signal transducer and activator of transcription 3). *Biochemical Journal* **455**, 229-237 (2013).

47. Zhao, L., Chen, W., Taylor, K.M., Cai, B. & Li, X. LIV-1 suppression inhibits HeLa cell invasion by targeting ERK1/2-Snail/Slug pathway. *Biochemical and Biophysical Research Communications* **363**, 82-88 (2007).

48. Kambe, T. Molecular architecture and function of ZnT transporters. in *Metal Transporters*, Vol. 69 (eds. Lutsenko, S. & Arguello, J.M.) 199-220 (2012).

49. Chimienti, F., Devergnas, S., Favier, A. & Seve, M. Identification and cloning of a beta-cell-specific zinc transporter, ZnT-8, localized into insulin secretory granules. *Diabetes* **53**, 2330-2337 (2004).

50. Chimienti, F., Devergnas, S., Pattou, F., Schuit, F., Garcia-Cuenca, R., Vandewalle, B., Kerr-Conte, J., Van Lommel, L., Grunwald, D., Favier, A. & Seve, M. In vivo expression and functional characterization of the zinc transporter ZnT8 in glucose-induced insulin secretion. *Journal of Cell Science* **119**, 4199-4206 (2006).

51. Nicolson, T.J., Bellomo, E.A., Wijesekara, N., Loder, M.K., Baldwin, J.M., Gyulkhandanyan, A.V., Koshkin, V., Tarasov, A.I., Carzaniga, R., Kronenberger, K., Taneja, T.K., Xavier, G.D., Libert, S., Froguel, P., Scharfmann, R., Stetsyuk, V., Ravassard, P., Parker, H., Gribble, F.M., Reimann, F., Sladek, R., Hughes, S.J., Johnson, P.R.V., Masseboeuf, M., Burcelin, R., Baldwin, S.A., Liu, M., Lara-Lemus, R., Arvan, P., Schuit, F.C., Wheeler, M.B., Chimienti, F. & Rutter, G.A. Insulin storage and glucose homeostasis in mice null for the granule zinc transporter ZnT8 and studies of the type 2 diabetes-associated variants. *Diabetes* **58**, 2070-2083 (2009).

52. Flannick, J., Thorleifsson, G., Beer, N.L., Jacobs, S.B.R., Grarup, N., Burtt, N.P., Mahajan, A., Fuchsberger, C., Atzmon, G., Benediktsson, R., Blangero, J., Bowden, D.W., Brandslund, I., Brosnan, J., Burslem, F., Chambers, J., Cho, Y.S., Douglas, D.A., Duggirala, R., Dymek, Z., Farjoun, Y., Fennell, T., Fontanillas, P., Forsen, T., Gabriel, S., Glaser, B., Gudbjartsson, D.F., Hanis, C., Hansen, T., Hreidarsson, A.B., Hveem, K., Ingelsson, E., Isomaa, B., Johansson, S., Jorgensen, T., Jorgensen, M.E., Kathiresan, S., Kong, A., Kooner, J., Kravic, J., Laakso, M., Lee, J.Y., Lind, L., Lindgren, C.M., Linneberg, A., Masson, G.,

Meitinger, T., Mohlke, K.L., Molven, A., Morris, A.P., Potluri, S., Rauramaa, R., Ribel-Madsen, R., Richard, A.M., Rolph, T., Saloemaa, V., Segre, A.V., Skarstrand, H., Steinthorsdottir, V., Stringham, H.M., Sulem, P., Tai, E.S., Teo, Y.Y., Teslovich, T., Thorsteinsdottir, U., Trimmer, J.K., Tuomi, T., Tuomilehto, J., Vaziri-Sani, F., Voight, B.F., Boehnke, M., McCarthy, M.I., Njolstad, P.R., Pedersen, O., Groop, L., Cox, D.R., Stefansson, K., Altshuler, D., Go, T.D.C. & Consortium, T.D.-G. Loss-of-function mutations in SLC30A8 protect against type 2 diabetes. *Nature Genetics* **46**, 357-363 (2014).

53. Coyle, P., Philcox, J.C., Carey, L.C. & Rofe, A.M. Metallothionein: The multipurpose protein. *Cellular and Molecular Life Sciences* **59**, 627-647 (2002).

54. Li, Y. & Maret, W. Human metallothionein metallomics. *Journal of Analytical Atomic Spectrometry* **23**, 1055-1062 (2008).

55. Vasak, M. & Meloni, G. Chemistry and biology of mammalian metallothioneins. *Journal of Biological Inorganic Chemistry* **16**, 1067-1078 (2011).

56. Maret, W. Redox biochemistry of mammalian metallothioneins. *Journal of Biological Inorganic Chemistry* **16**, 1079-1086 (2011).

57. Maret, W. Zinc coordination environments in proteins as redox sensors and signal transducers. *Antioxidants & Redox Signaling* **8**, 1419-1441 (2006).

58. Nzengue, Y., Lefebvre, E., Cadet, J., Favier, A., Rachidi, W., Steiman, R. & Guiraud, P. Metallothionein expression in HaCaT and C6 cell lines exposed to cadmium. *Journal of Trace Elements in Medicine and Biology* **23**, 314-323 (2009).

59. Ye, B., Maret, W. & Vallee, B.L. Zinc metallothionein imported into liver mitochondria modulates respiration. *Proceedings of the National Academy of Sciences of the United States of America* **98**, 2317-2322 (2001).

60. Maret, W. Molecular aspects of human cellular zinc homeostasis: Redox control of zinc potentials and zinc signals. *Biometals* **22**, 149-157 (2009).

61. Maret, W. Redox biochemistry of metallothioneins and protein tyrosine phosphatases in growth factor signalling. *Free Radical Biology and Medicine* **53**, S26-S26 (2012).

62. Maret, W. The function of zinc metallothionein: A link between cellular zinc and redox state. *Journal of Nutrition* **130**, 1455S-1458S (2000).

63. Bohnsack, B.L. & Hirschi, K.K. Nutrient regulation of cell cycle progression. *Annual Review of Nutrition* **24**, 433-453 (2004).

64. Martin, P. Wound healing - Aiming for perfect skin regeneration. *Science* **276**, 75-81 (1997).

65. Guo, S. & DiPietro, L.A. Factors affecting wound healing. *Journal of Dental Research* **89**, 219-229 (2010).

66. Lunt, S.Y. & Vander Heiden, M.G. Aerobic glycolysis: Meeting the metabolic requirements of cell proliferation. *Annual Review of Cell and Developmental Biology, Vol 27* **27**, 441-464 (2011).

67. Jorgensen, P. & Tyers, M. How cells coordinate growth and division. *Current Biology* **14**, R1014-R1027 (2004).

68. Johnson, D.G. & Walker, C.L. Cyclins and cell cycle checkpoints. *Annual Review of Pharmacology and Toxicology* **39**, 295-312 (1999).

69. Huesca, M., Lock, L.S., Khine, A.A., Viau, S., Peralta, R., Cukier, I.H., Jin, H., Al-Qawasmeh, R.A., Lee, Y., Wright, J. & Young, A. A novel small molecule with potent anticancer activity inhibits cell growth by modulating intracellular labile zinc homeostasis. *Molecular Cancer Therapeutics* **8**, 2586-2596 (2009).

70. Chesters, J.K. & Petrie, L. A possible role for cyclins in the zinc requirements during G1 and G2 phases of the cell cycle. *Journal of Nutritional Biochemistry* **10**, 279-290 (1999).

71. Chesters, J.K., Petrie, L. & Lipson, K.E. 2 Zinc-dependent steps during G1 to S-phase transition. *Journal of Cellular Physiology* **155**, 445-451 (1993).

72. Sun, L., Chai, Y., Hannigan, R., Bhogaraju, V.K. & Machaca, K. Zinc regulates the ability of Cdc25C to activate MPF/cdk1. *Journal of Cellular Physiology* **213**, 98-104 (2007).

73. Falchuk, K.H. The molecular basis for the role of zinc in developmental biology. *Molecular and Cellular Biochemistry* **188**, 41-48 (1998).

74. Stankiewicz, A.J., Falchuk, K.H. & Vallee, B.L. Composition and structure of zinc-deficient Euglena-Gracilis chromatin. *Biochemistry* **22**, 5150-5156 (1983).

75. Wu, F.Y.H. & Wu, C.W. Zinc in DNA-replication and transcription *Annual Review of Nutrition* **7**, 251-272 (1987).

76. Vallee, B.L. & Falchuk, K.H. Zinc and gene-expression. *Philosophical Transactions of the Royal Society of London Series B-Biological Sciences* **294**, 185-197 (1981).

77. Dreosti, I.E. Zinc and the gene. *Mutation Research-Fundamental and Molecular Mechanisms of Mutagenesis* **475**, 161-167 (2001).

78. Sharif, R., Thomas, P., Zalewski, P. & Fenech, M. The role of zinc in genomic stability. *Mutation Research-Fundamental and Molecular Mechanisms of Mutagenesis* **733**, 111-121 (2012).

79. Haase, H. & Maret, W. Intracellular zinc fluctuations modulate protein tyrosine phosphatase activity in insulin/insulin-like growth factor-1 signaling. *Experimental Cell Research* **291**, 289-298 (2003).

80. Paski, S.C. & Xu, Z.M. Growth factor stimulated cell proliferation is accompanied by an elevated labile intracellular pool of zinc in 3T3 cells. *Canadian Journal of Physiology and Pharmacology* **80**, 790-795 (2002).

81. Jin, R.X., Chow, V.T.K., Tan, P.H., Dheen, S.T., Duan, W. & Bay, B.H. Metallothionein 2A expression is associated with cell proliferation in breast cancer. *Carcinogenesis* **23**, 81-86 (2002).

82. McRae, R., Lai, B. & Fahrni, C.J. Subcellular redistribution and mitotic inheritance of transition metals in proliferating mouse fibroblast cells. *Metallomics* **5**, 52-61 (2013).

83. Nagel, W.W. & Vallee, B.L. Cell-cycle regulation of metallothionein in human colonic-cancer cells. *Proceedings of the National Academy of Sciences of the United States of America* **92**, 579-583 (1995).

84. Li, Y. & Maret, W. Transient fluctuations of intracellular zinc ions in cell proliferation. *Experimental Cell Research* **315**, 2463-2470 (2009).

85. Halter, M., Elliott, J.T., Hubbard, J.B., Tona, A. & Plant, A.L. Cell volume distributions reveal cell growth rates and division times. *Journal of Theoretical Biology* **257**, 124-130 (2009).

86. Uriu-Adams, J.Y. & Keen, C.L. Zinc and reproduction: Effects of zinc deficiency on prenatal and early postnatal development. *Birth Defects Research Part B-Developmental and Reproductive Toxicology* **89**, 313-325 (2010).

87. Falchuk, K.H. & Montorzi, M. Zinc physiology and biochemistry in oocytes and embryos. *Biometals* **14**, 385-395 (2001).

88. Rogers, J.M., Keen, C.L. & Hurley, L.S. Zinc-deficiency in pregnant long-evans hooded rats - Teratogenicity and tissue trace-elements. *Teratology* **31**, 89-100 (1985).

89. Keen, C.L. & Hurley, L.S. Zinc and Reproduction: Effects of Deficiency on Foetal and Postnatal Development. in *Zinc in the Human Body* (ed. Mills, C.F.) 183 - 220 (Springer London, London, 1989).

90. Bernhardt, M.L., Kong, B.Y., Kim, A.M., O'Halloran, T.V. & Woodruff, T.K. A zinc-dependent mechanism regulates meiotic progression in mammalian oocytes. *Biology of Reproduction* **86**(2012).

91. Kim, A.M., Vogt, S., O'Halloran, T.V. & Woodruff, T.K. Zinc availability regulates exit from meiosis in maturing mammalian oocytes. *Nature Chemical Biology* **6**, 674-681 (2010).

92. Kong, B.Y., Bernhardt, M.L., Kim, A.M., O'Halloran, T.V. & Woodruff, T.K. Zinc maintains prophase I arrest in mouse oocytes through regulation of the MOS-MAPK pathway. *Biology of Reproduction* **87**(2012).

93. Kim, A.M., Bernhardt, M.L., Kong, B.Y., Ahn, R.W., Vogt, S., Woodruff, T.K. & O'Halloran, T.V. Zinc sparks are triggered by fertilization and facilitate cell cycle resumption in mammalian eggs. *Acs Chemical Biology* **6**, 716-723 (2011).

94. Que, E.L., Bleher, R., Duncan, F.E., Kong, B.Y., Gleber, S.C., Vogt, S., Chen, S., Garwin, S.A., Bayer, A.R., Dravid, V.P., Woodruff, T.K. & O'Halloran, T.V. Quantitative mapping of zinc fluxes in the mammalian egg reveals the origin of fertilization-induced zinc sparks. *Nature Chemistry* **7**, 130-139 (2015).

CHAPTER 2

PROBING LABILE ZINC POOLS IN PROLIFERATING CELLS

As mentioned in Chapter 1, previous studies using synchrotron X-ray fluorescence (SXRF) microscopy revealed an influx of zinc into NIH 3T3 fibroblasts at the onset of mitosis.[1] Although SXRF was able to reveal the location of total metal content and quantitatively determine a 2 to 3-fold increase of zinc during mitosis, whether the influx of zinc constitutes part of the labile pool remains unclear. The aim of Chapter 2 is to determine if the influx of zinc observed during the onset of mitosis is tightly bound to ligands, or part of the labile pool. Complementary to the previous SXRF experiment the dynamic, labile zinc in proliferating NIH 3T3 fibroblasts was imaged using a recently developed Zn(II)-selective, ratiometric probe capable of two photon excitation (Chromis1). Additionally, an important objective in this chapter was the proper characterization of the probe thereof. Lastly, fluorescent indicators specifically highlighting the endoplasmic reticulum, mitochondria and lipid droplets, are used in combination with Chromis1 to study the location of the labile zinc pools in relation to these select intracellular organelles.

2.1 Background

Zinc is an essential micronutrient required for cell division,[2-6] however the mechanisms of regulation and redistribution of zinc during cell division remain largely elusive. To investigate total trace metal distribution as cells pass through the various stages of mitosis, McRae et al. performed X-ray fluorescence microscopy (SXRF) studies on individual, proliferating NIH 3T3 fibroblasts.[1] The data revealed a distinct redistribution pattern of zinc that was found to be spatially correlated with copper and sulfur densities but not phosphorus as well as a 2 to 3-fold increase of zinc during mitosis. While zinc is required for cell division what could be the purpose of such significant inundation?

Signaling? Catalytic functions? The first step to investigate these types of questions is to determine if the zinc is free and available or already tightly bound to proteins during the influx.

The total zinc content of a cell or biological specimen can be categorized into two different groups: tightly bound to proteins or kinetically labile zinc involved in an exchangeable buffering system.[7-9] The majority of cellular zinc is tightly bound to proteins for catalytic or structural purposes; however, the subpool of labile zinc is critical for signaling and regulating functions.[10] Free zinc ions as well as zinc reversibly bound to proteins constitute the labile pool. Proteins that transport zinc across membranes, distribute zinc amongst organelles, and rely on zinc for regulation will all interact with zinc ions in a reversible manner.[9] Use of synthetic and genetically encoded fluorescent probes have revealed this labile, exchangeable zinc pool in mammalian cells is buffered at picomolar to low nanomolar concentrations.[11-13] Chapter 1 provides more detail about the structural, catalytic, and signaling roles zinc can fulfill.

For a comprehensive understanding of zinc regulation and distribution during cell division, all forms of zinc should be studied. Depending on the method applied, different subsets of zinc pools are detected. SXRF microscopy used to collect the data reported by McRae et al. provides information about the total metal content in the cell without any indication if the zinc is tightly bound to proteins or kinetically labile and involved in the exchangeable buffering system. In order to better understand the purpose of the influx at the onset of mitosis, it is important to determine which of the two categories of zinc are responsible. For this reason, zinc-selective fluorescent probes can be used to selectively detect only the exchangeable zinc pools in the sample.

2.2 Fluorescent Probes for the Detection of Labile Zinc

For the detection of labile cellular Zn(II), synthetic fluorescent probes that can engage in a competitive exchange with the endogenous pool are particularly promising tools. As most laboratories are equipped with standard fluorescence microscopes, this technique is widely accessible and cost effective. Fluorescence detection offers exceptional sensitivity and allows for the detection of fluorophores at the single molecule level. A majority of fluorescent probes function as “turn-on” sensors. Such probes typically consist of a chelator moiety, which selectively binds the metal ion of interest, and a fluorophore that translates the metal binding event into an emission increase. The change in fluorescence emission can be used to estimate the concentration of free Zn(II) ions present in solution; however, there are several limitations for applying this approach towards the determination of free Zn(II) in a cellular environment as outlined in the following section.

Assuming a 1:1 stoichiometry, the solution equilibrium (1) between a probe P and the free buffered Zn(II) ions can be described by the mass action equation (2)

$$\mathrm{P} + \mathrm{Zn(II)} \underset{k_r}{\overset{k_f}{\rightleftharpoons}} \mathrm{PZn(II)} \qquad (1)$$

$$K = \frac{k_f}{k_r} = \frac{[\mathrm{PZn(II)}]}{[\mathrm{P}] \cdot [\mathrm{Zn(II)}]_{free}} \quad \text{and} \quad K_d = \frac{1}{K} = \frac{[\mathrm{P}] \cdot [\mathrm{Zn(II)}]_{free}}{[\mathrm{PZn(II)}]} \qquad (2)$$

where k_f and k_r refer to the forward and reverse rate constants, respectively, K is the stability constant, and [P], [Zn(II)], and [PZn(II)] are the respective concentrations of each species at equilibrium. Furthermore, the fractional saturation f of the probe may be defined as the ratio of the probe-bound Zn(II) and the total probe concentration $[P]_{total}$:

$$f = \frac{[\mathrm{PZn(II)}]}{[P]_{total}} = \frac{[\mathrm{PZn(II)}]}{[\mathrm{P}] + [\mathrm{PZn(II)}]} \tag{3}$$

After combining equations (2) and (3), the fractional saturation f can be expressed as a function of the K_d and the free Zn(II) concentration:

$$f = \frac{[\mathrm{Zn(II)}]_{free}}{K_d + [\mathrm{Zn(II)}]_{free}} \tag{4}$$

If the concentration of $\mathrm{Zn(II)}_{free}$ = K_d, P and PZn(II) are present at equimolar concentrations, the fractional saturation of the probe f is 0.5 (50%). A plot of f vs. $[\mathrm{Zn(II)}]_{free}$ further illustrates that the largest changes of f occur when the free Zn(II) concentrations vary within the vicinity of the K_d (Figure 2.1, $K_d = 10^{-12}$ M), and for this reason, the response of a fluorescent probe is strongest, if its dissociation constant (K_d) is similar compared to the buffered concentration of the Zn(II) pool to be probed.

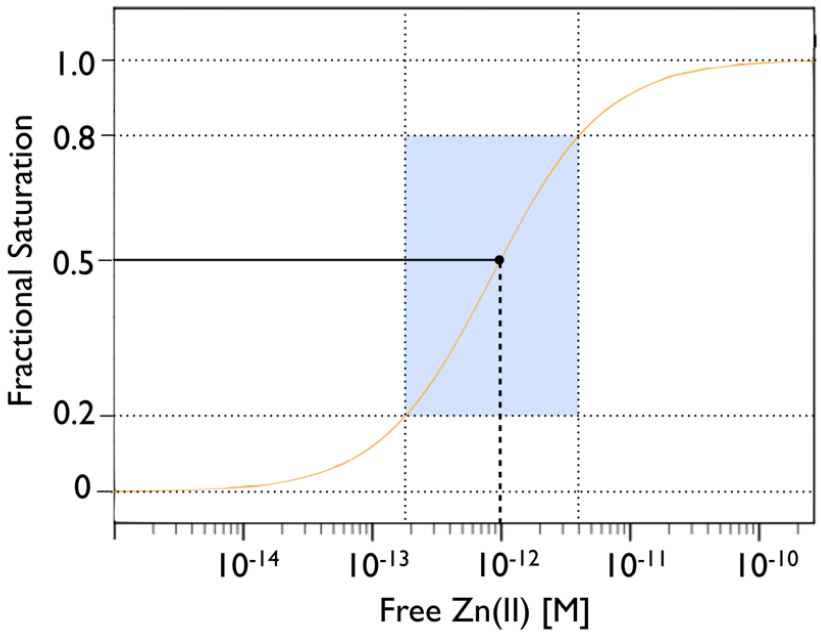

Figure 2.1: Relationship between free Zn(II) concentration and the fractional saturation of a fluorescent probe. With an increase in metal ion concentration, an increase in fluorescence is observed. Shaded blue square represents the ideal K_d range. At 50% fractional saturation, the metal concentration equals K_d of probe.

According to Deranleau, reliable measurements are obtained between 20-80% fractional saturation, whereas outside this range the error increases exponentially.[14,15] Therefore, fluorescent probes with 1:1 binding stoichiometry cover a dynamic range of about two logarithmic units of free Zn(II) concentrations as illustrated with the blue-shaded area in Figure 2.1. If the probe dissociation constant is much higher or lower than the buffered cellular Zn(II) concentrations, the saturation level falls outside the 20-80% window and therefore the probe will not be able to reliably report on dynamic changes or properly reflect differences in the subcellular distribution of Zn(II) pools. Additional factors such as photobleaching, subcellular sequestration, ionophore redistribution or cell-to-cell variability of the probe concentration further hinder the ability to reliably detect dynamic

changes and the distribution of labile Zn(II). These problems may result in misleading staining artifacts that do not reflect the actual cellular zinc status.

2.2.1 Ratiometric Fluorescent Probes

To overcome some of the typical challenges associated with fluorescent probes, Tsien and coworkers introduced the use of ratiometric probes that undergo a spectral shift of the excitation or emission band upon binding the metal ion of interest.[16] The ratio *R* of the fluorescence intensities can then be used to determine the free metal ion concentration according to equation (5) without the knowledge of the probe concentration.

$$[\mathrm{Zn(II)}]_{free} = K_\mathrm{d}\left(\frac{R - R_\mathrm{min}}{R_\mathrm{max} - R}\right)\left(\frac{S_\mathrm{f}}{S_\mathrm{b}}\right) \qquad (5)$$

In equation (5), *R* is the ratio of the two fluorescence intensities at the two excitation or emission wavelengths, K_d is the dissociation constant of the 1:1 Zn(II)-probe complex, R_{min} and R_{max} are the minimum and maximum fluorescence intensity ratios for the free and Zn(II)-saturated probe, and S_f and S_b are instrument dependent parameters that need to be determined through an independent calibration.

A number of ratiometric Zn(II) probes have been developed for biological imaging (Table 1), however, none of these probes have been widely used.

Table 2.1: Zn(II)-responsive ratiometric fluorescent probes

Compound	λ_{ex} (nm)[a]	λ_{em} (nm)[a]	K_d[b]	R_{max}/R_{min}[c]	Ref
Fura-Zin	378 (-48)	510 (0)	2.10 x10^{-6}	9	[17,18]
Indo-Zin	350 (0)	480 (-85)	3.00 x10^{-6}		[17]
ZnAF-R2	365 (-30)	495 (0)	2.80 x10^{-9}	7	[19]
DPA-COUM-4	400 (+31)	484 (+21)	5.00 x10^{-7}		[20]
ZNP1	499	528/624	5.5 x10^{-10}	17.8	[21]
Zinbo-5	337 (39)	407 (36)	2.20 x10^{-9}	33	[22]
CZ1		488/534[d]	2.50 x10^{-10}	8	[23,24]
CZ2		590/535[d]		1.7[e]	[24]
DIPCY	627 (+44)	758 (+7)	2.30 x10^{-8}	1.5	[25]
ZnIC	513	543 (+15)	1.30 x10^{-12}	2.4	[26]
RF3	514 (-19)	540 (-17)	2.20 x10^{-5}	2.4	[27]
ZTRS	360 (0)	483 (+31)	5.70 x10^{-9}	30	[28]

[a]spectral change upon saturation with Zn(II). [b]dissociation constant. [c]dynamic range according to eq. (1). [d]tandem sensing scheme with two fluorophores. [e]value reported in vivo.

As an alternative to small-molecule fluorescent probes, genetically encoded protein-based probes are a major fluorescence-based tool to image Zn(II) in vivo. These biosensors are comprised of one or more fluorescent proteins (FP) fused to a metal binding domain. While binding of the metal triggers a change in fluorescence intensity or wavelength of a single-FP probe, metal binding alters the intermolecular distance or orientation of the donor or acceptor fluorophores of multi-FP probes thus altering the rate of energy transfer between the two.[12,13,29] Therefore, multi-FP probes typically rely upon Förster Resonance Energy Transfer (FRET) to measure the concentration of a particular metal. Similar to ratiometric probes, multi-FP genetically encoded probes can provide

quantitative measurements of buffered ion concentrations using the ratio of two fluorescent intensities, the donor fluorescent intensity and the acceptor fluorescent intensity.

2.2.2 Two-Photon Excitation Microscopy (TPEM)

Compared to conventional single photon excitation, two-photon excitation microscopy (TPEM) offers intrinsic 3D resolution, reduced toxicity, increased specimen penetration, and negligible background fluorescence. Two-photon excitation involves two photons of approximately equal energy simultaneously interacting with a fluorophore, producing an excitation equivalent to the absorption of a single photon possessing twice the energy.[30-32] Thus, two-photon excitation only requires half of the energy or twice the wavelength in order to excite a fluorophore.

Although some of the probes listed in Table 2.1 have been utilized for two-photon imaging, none of them have been characterized in terms of the actual two-photon excited fluorescence response and the two-photon absorption (TPA) cross section. This presents two potential limitations. First, the fluorophore brightness may be compromised due to a low TPA cross section. Second, many of these probes undergo a shift of excitation rather than emission wavelength upon saturation with Zn(II), requiring more than one excitation wavelength rendering these probes unsuitable for two-photon microscopy. To synchronously excite the sample with two multiphoton lasers would be impossible. Unfortunately, few emission ratiometric probes optimized for two-photon excitation exist. For this reason, a new Zn(II)-responsive fluorescent probe, Chromis1, was developed and characterized.

Chromis1

Chromis1-ethyl ester R = CH_2CH_3
Chromis1-acid R = H

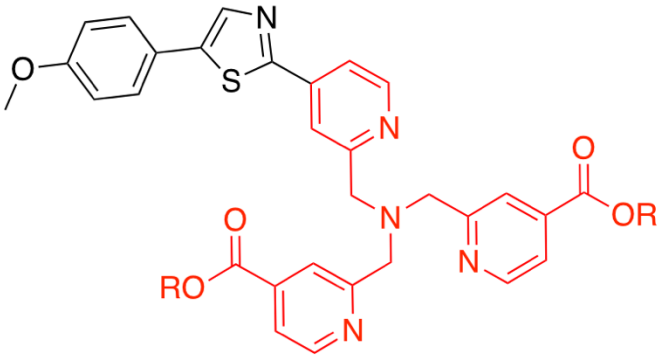

Figure 2.2: Ratiometric Zn(II)-responsive two photon probe for live cell imaging of labile Zn(II) ions, Chromis1. The red piece of the structure indicates the tris(2-picolyl)amine functional group that acts as the zinc binding domain. Synthesis performed by Dr. Sumalekshmy Sarojini.

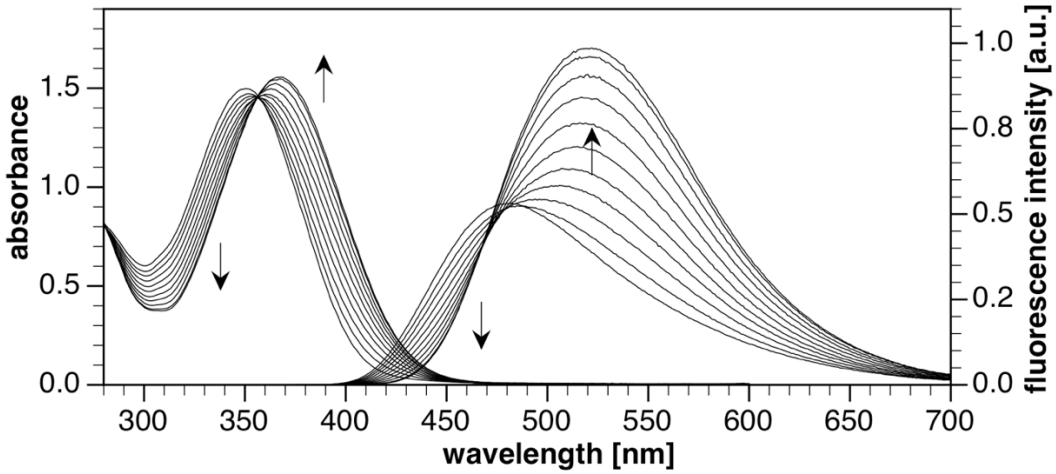

Figure 2.3: Fluorescence emission spectrum of Chromis1 indicating spectral changes upon saturation with Zn(II). Multiple samples of a known probe concentration were incubated overnight in increasing concentrations of Zn(II) buffer. Dr. Sumalekshmy Sarojini recorded fluorimeter measurements with each sample excited at 355 nm. As the Zn(II) concentration increased, a spectral shift and an increase in fluorescence intensity is observed. (10 mM PIPES, pH 7, 0.1 M $KClO_4$)

2.2.3 Zn(II)-Selective Probe, Chromis1

In order to detect and visualize the location and distribution of labile Zn(II) pools in live cells and tissues, a Zn(II)-selective ratiometric fluorescent probe, Chromis1, optimized for two photon excitation at 720-760 nm was developed (Figure 2.2). The tris(2-picolyl)amine functional group of the probe acts as a chelator moiety which permits selective binding of Zn(II) in a 1:1 complex with a K_d around 1.55 nM. Upon saturation with Zn(II), the probe responds with a strong red-shift, approximately 40 nm, of the fluorescence emission, which is suitable for ratiometric quantification (Figure 2.3).

2.3 Establishing Ratiometric Imaging Conditions

Prior to using Chromis1 to monitor labile zinc in proliferating cells, it is important to establish the probe's capabilities in live cell conditions. In order to trust the validity of the data, Chromis1 must first be properly characterized in terms of its permeability, chemical stability, resistance to change in pH, and response rate in both high and low Zn(II) concentrations. To begin, NIH 3T3 mouse fibroblast cells were incubated with 10 μM Chromis1-ester for 15 minutes in 37°C then imaged using a Zeiss LSM710 microscope equipped with a multiphoton laser tuned to 720 nm to initially confirm the probe's permeability. The resulting ratiometric fluorescence images demonstrated intracellular staining by Chromis1-ester throughout the cytoplasm and excluded from the nucleus. To compare, the same experiment was performed using 10 μM Chromis1-acid. As predicted, this derivative was unable to permeate the cell resulting in no detectable fluorescence (Data not shown). Next, a series of time-lapse imaging studies were performed to establish the ability of Chromis1-ester to monitor dynamic changes in intracellular labile Zn(II).

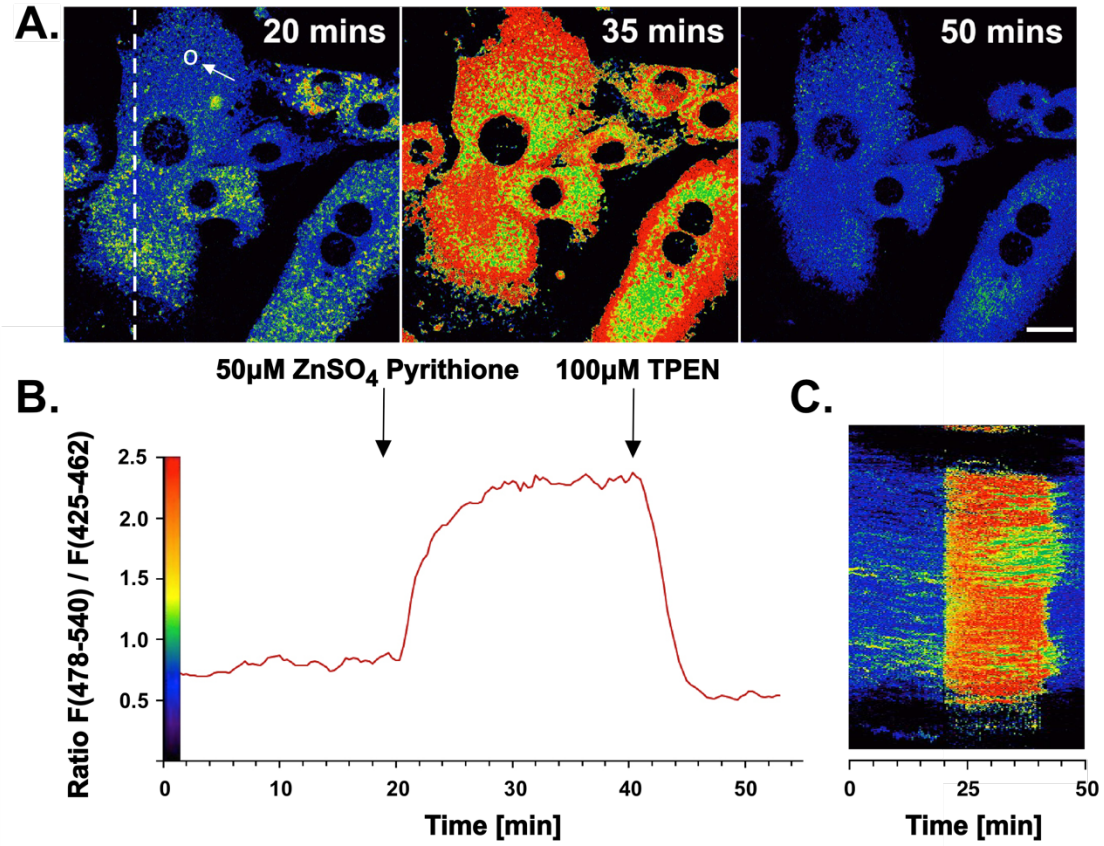

Figure 2.4: Ratiometric response to addition of $ZnSO_4$ and TPEN. Two-photon excited ratiometric imaging of Zn(II) fluxes in live 3T3 fibroblasts. Cells were treated with 10 μM Chromis1-ester then imaged inside of a temperature-controlled chamber mounted on the microscope stage. After 20 minutes, the cells were exposed to a buffer solution containing 100 μM $ZnSO_4$ / pyrithione followed by a second buffer containing 100 μM TPEN at the 41-minute mark. **A**: False color ratiometric images acquired at the indicated time points. **B**: Average intensity ratio change vs. time for the region of interest shown as a circle in the left panel of (A). **C**: False color ratiometric kymograph for the region of interest shown as a dotted line in the left panel of (A). Two-photon excitation occurred at 720 nm, the emission was collected between 425-462 and 478-540 nm. Scale bar = 20 μm.

2.3.1 Calibration of Zn(II)-Selective Probe, Chromis1, in Live Cells

To demonstrate Chromis1-ester as a fluorescent ratiometric probe for two-photon imaging of dynamic cellular Zn(II), time-lapse sequences were acquired of adherent NIH 3T3 cells preloaded with 10 μM of the probe. Images were taken every 20 seconds for roughly 1 hour. After 20 minutes of imaging in basal conditions, cells were exposed to $ZnSO_4$ together with the ionophore pyrithione. This was followed by a perfusion at 41 minutes with a cell permeable, non-fluorescent, high-affinity Zn(II) chelator, N,N,N',N'-tetrakis-(2-pyridylmethyl)-ethylenediamine (TPEN). The image was produced from the ratio of emission intensities at (478 nm – 540 nm) / (425 nm – 462 nm).

Cells grown under basal conditions initially indicate a low intensity ratio of 0.6 dispersed uniformly throughout the cytoplasm (Figure 2.4). This ratio changes in a manner dependent upon the availability of Zn(II) within the cell. After perfusion with $ZnSO_4$/pyrithione, the fluorescence ratio increased more than 3-fold reaching 2.5. To confirm the change of fluorescence intensity resulted from the increased concentration of Zn(II)-Chromis1, cells were then treated with TPEN. Perfusion with TPEN led to a complete reversal of the intensity ratio down to 0.5, slightly lower than that of the unbound probe under basal conditions.

Effectively, the two-photon ratiometric images confirm intracellular zinc availability can be readily gauged using this Zn(II)-selective probe. This experiment also demonstrated Chromis1-ester to be robust and nontoxic to the cells. The probe did not photobleach and cells were healthy and alive after almost an hour of imaging. A plot of the fluorescence intensity ratio vs. time revealed surprisingly rapid dynamics, both for Zn(II) binding and release which each occurred in seconds (Figure 2.4B). In conjunction with the false color images, this plot indicated the TPEN successfully returned the ratio to lower than basal level, therefore the response was completely reversible. This reveals the probe has an appropriate binding affinity capable of releasing Zn(II). Furthermore, the

decrease in ratio lower than basal conditions indicates the Chromis1-ester was initially detecting endogenous zinc. Using equation (5) from section 2.2.1, the buffered Zn(II) concentration can be calculated as approximately 300 pM. Additionally, Chromis1-ester demonstrated the ability to monitor a high dynamic range of zinc fluctuations. Figure 2.4 illustrates a ratio change from 0.6 to 2.4, corresponding to a 4-fold increase of detection level. Due to the difficulties balancing this large of a dynamic range on the microscope, Chromis1-ester fluorescence was over exposed at the highest ratio when imaging. With the proper equipment and settings Chromis1-ester could reveal an even larger dynamic range of zinc fluctuations. Lastly, the cytosolic staining of Chromis1-ester appears to be punctate and localized in subcellular compartments, presumably the probe is lipophilic and transitions into membranes. To further investigate where Chromis1-ester is inside the cell, a series of localization studies with Chromis1-ester and other fluorescent indicators of organelles was performed.

2.3.2 Elucidation of the Subcellular Localization of Chromis1-Ester

The punctate staining pattern observed for Chromis1-ester in the previous experiments suggests it is localized to specific cellular structures. After the characterization in NIH 3T3 fibroblasts, the ratiometric Zn(II)-selective probe can now be utilized to asses the intracellular location of Chromis1-ester and subsequently reveal the locations of labile Zn(II) pools. Using both plasmid transfection and live cell fluorescent markers, the purpose of this study is to elucidate the location of Chromis1-ester compared to mitochondria, endoplasmic reticulum (ER) and lipid droplets.

2.3.2.1 Spatial Correlation of Chromis1-Ester and Mitochondria

Zn(II) pools are essential for sustaining mitochondrial protein functions. Mitochondria house numerous Zn(II) dependent enzymes,[33,34] primarily metallothioneins

(MTs), a major source of labile zinc.[35,36] This family of metal-binding proteins is capable of reversibly binding seven Zn(II) ions simultaneously and creating labile pools for other metalloproteins and transcription factors to bind. For these reasons, mitochondria are a reasonable target location to examine for colocalization with Chromis1-ester.

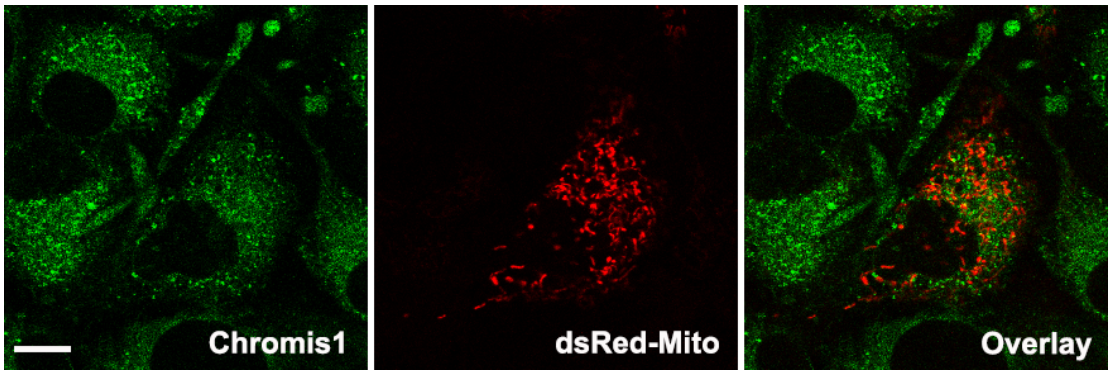

Figure 2.5: Spatial correlation analysis of Chromis1-ester with mitochondria in 3T3 cells. (Left) Epifluorescence image of Chromis1-ester excited via a pulsed IR/multiphoton laser tuned to 720 nm, emission collected 400 - 498 nm. (Center) Epifluorescence image of mitochondria labeled via transfection of pDs_Red2-mito, excited at 561 nm, emission collected 570 - 700 nm. (Right) Overlay image indicating the negligible amount of spatial correlation between Chromis1-ester and pDs_Red2-mito in orange/yellow color, corresponding to a Pearson correlation coefficient of 0.19. Scale bar = 20 μm.

Cells were transfected with the pDs_Red2-mito plasmid for mitochondria before treatment with Chromis1-ester and undergoing live cell fluorescent imaging. Fluorescence emission of Chromis1-ester and the fluorescent organelle marker were collected simultaneously with the laser and filter settings switching on a line-by-line basis. In the resulting images, Chromis1-ester produces a strong fluorescence pattern distributed throughout the cytoplasm. Mitochondria are distinct intracellular structures made clearly visible in fluorescence microscopy from the pDs_Red2-mito plasmid. As illustrated in Figure 2.5, fluorescent imaging revealed Chromis1-ester and mitochondria are not

correlated in location. Chromis1-ester (green) and the dsRed-Mito expression (red) are distinct in the overlay image. No spatial correlation (indicated by yellow) is observed. Additionally, pixel-by-pixel analysis was performed for a quantitative assessment of the degree of correlation between the two images. Using the Coloc2 plugin of ImageJ[37] software, Pearson's correlation coefficient (PCC) can be calculated as a measurement of the linear correlation between two variables. PCC values range between +1 and -1, where 1 represents a complete positive correlation, 0 is no correlation at all and -1 is a total negative correlation.[38,39] For the Chromis1-ester vs. dsRed-Mito comparison, Coloc2 calculated a PCC of 0.19, therefore indicating a very low, almost negligible correlation.

2.3.2.2 Spatial Correlation of Chromis1-Ester and Endoplasmic Reticulum

Labile Zn(II) pools have been identified at the endoplasmic reticulum (ER). Results based on ratiometric imaging using a genetically encoded sensor, ER-ZapCY1, estimate 0.9 pM of Zn(II) in the ER of HeLa cells.[12] Labile Zn(II) is also implicated as a second messenger from the ER required for signaling in the tyrosine kinase pathways.[40] Regulated by ZIP7, zinc is released from intracellular stores in the ER resulting in Zn(II)-mediated inactivation of protein phosphatases, consequentially allowing for the activation of multiple tyrosine kinases.[41]

Similar to the mitochondrial imaging, cells were transfected with pEYFP-ER plasmids following treatment with Chromis1-ester for live cell imaging. Fluorescence emission of Chromis1-ester and the fluorescent ER marker were collected simultaneously with the laser and filter settings switching on a line-by-line basis. As with mitochondria, Chromis1-ester and the ER have limited spatial correlation (Figure 2.6). Chromis1-ester (green) and the EYFP-ER expression (red) are distinct in the overlay image. No spatial correlation (indicated by yellow) is observed and a PCC value of 0.38 was calculated using the ImageJ plugin, Coloc2, indicating a very low, almost negligible correlation.

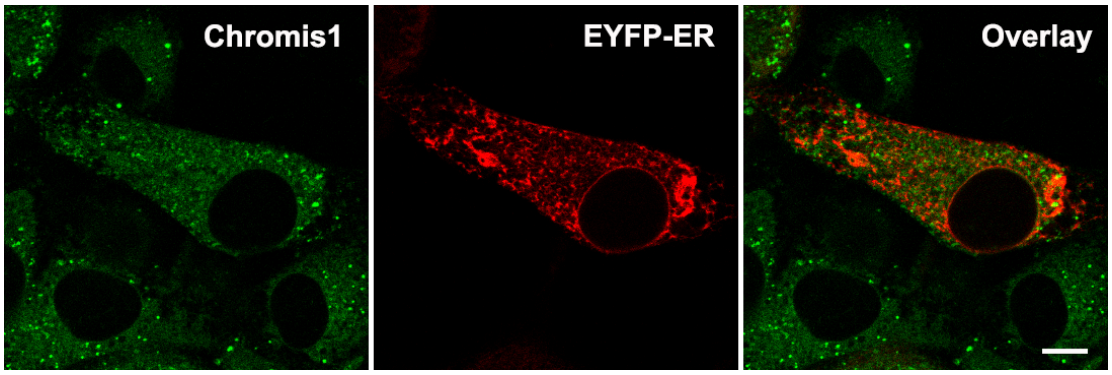

Figure 2.6: Spatial correlation analysis of Chromis1-ester with ER in NIH 3T3 fibroblasts. (Left) Epifluorescence image of Chromis1-ester excited via a pulsed IR/multiphoton laser tuned to 720 nm, emission collected 400 - 498 nm. (Center) Epifluorescence image of ER labeled via transfection of pEYFP-ER, excited at 514 nm, emission collected 525 – 675 nm. (Right) Overlay image indicating the amount of spatial correlation between Chromis1-ester and pEYFP-ER in orange/yellow color, corresponding to a Pearson correlation coefficient of 0.38. Scale bar = 20 μm.

2.3.2.3 Spatial Correlation of Chromis1-Ester and Lipid Droplets

Lastly, cells were co-stained with Chromis1-ester and BODIPY 493/503, a fluorescent indicator of neutral lipids. Fluorescence emission of Chromis1-ester and BODIPY 493/503 were collected simultaneously with the laser and filters settings switching on a line-by-line basis. As illustrated in Figure 2.7, a substantial degree of spatial correlation, indicated in yellow, between Chromis1-ester (green) and BODIPY 493/503 (red) was observed. Additionally, a PCC value of 0.67 was calculated using the ImageJ plugin, Coloc2, quantitatively suggesting Chromis1-ester is more spatially correlated with lipid droplets than it is with mitochondria or ER.

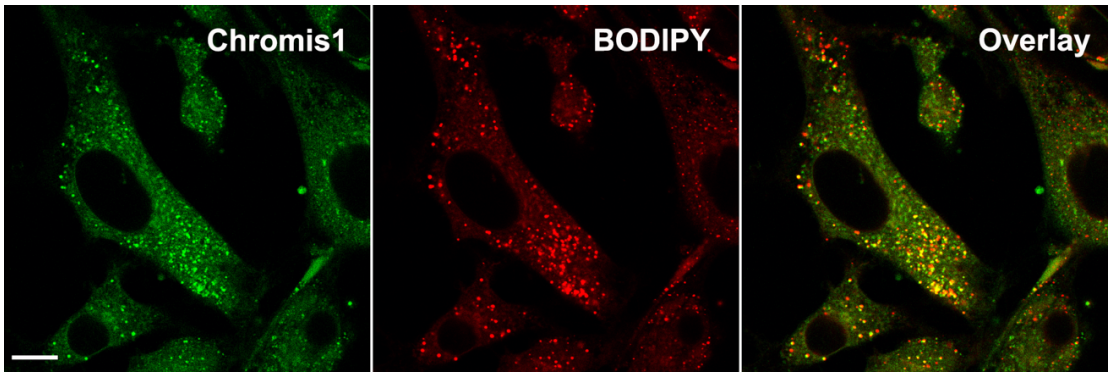

Figure 2.7: Spatial correlation analysis of Chromis1-ester with lipid droplets in NIH 3T3 fibroblasts. (Left) Epifluorescence image of Chromis1-ester excited via a pulsed IR/multiphoton laser tuned to 720 nm, emission collected 400 - 498 nm. (Center) Epifluorescence image of lipid droplets labeled via BODIPY 493/503, excited at 488 nm, emission collected 525 – 675 nm. (Right) Overlay image indicating the amount of spatial correlation between Chromis1-ester and BODIPY 493/503 in orange/yellow color, corresponding to a Pearson Correlation Coefficient of 0.67. Scale bar = 20 μm.

2.3.3 Neutralization to Exclude pH Sensitivity

Potentiometric studies of Chromis1-acid revealed protonation constants of 5.5 and 1.2 (Scheme 2.1), where the latter could be attributed to protonation of the fluorophore pyridine nitrogen (data not shown). Although the double-protonated probe is non-fluorescent, the charge-transfer character of the emissive state results in excited state protonation of the fluorophore to produce a weak red-shifted fluorescence emission (Scheme 2.2). While intracellular pH levels are maintained at approximately 7.4 in the cytosol,[42,43] lysosomes and other acidic compartments contain proton pumps that lower the pH to 5.0.[44] Presumably due the increased lipophilicity compared to the acid form, Chromis1-ester is distributed throughout the cytoplasm and appears as punctate staining, likely associated with the membrane of vesicular structures or organelles, possibly lysosomes. Although emitting with significantly lower quantum yield, the red-shifted emission of the proton transfer species, which is the dominant form at lower pH, might

yield an intensity ratio increase similar to the one observed for the Zn(II)-bound probe. In order to test whether the fluorescence intensity ratio of Chromis1-ester is affected by a rapid change of the pH in acidic compartments, a neutralization study was performed using Bafilomycin and LysoTracker Red.

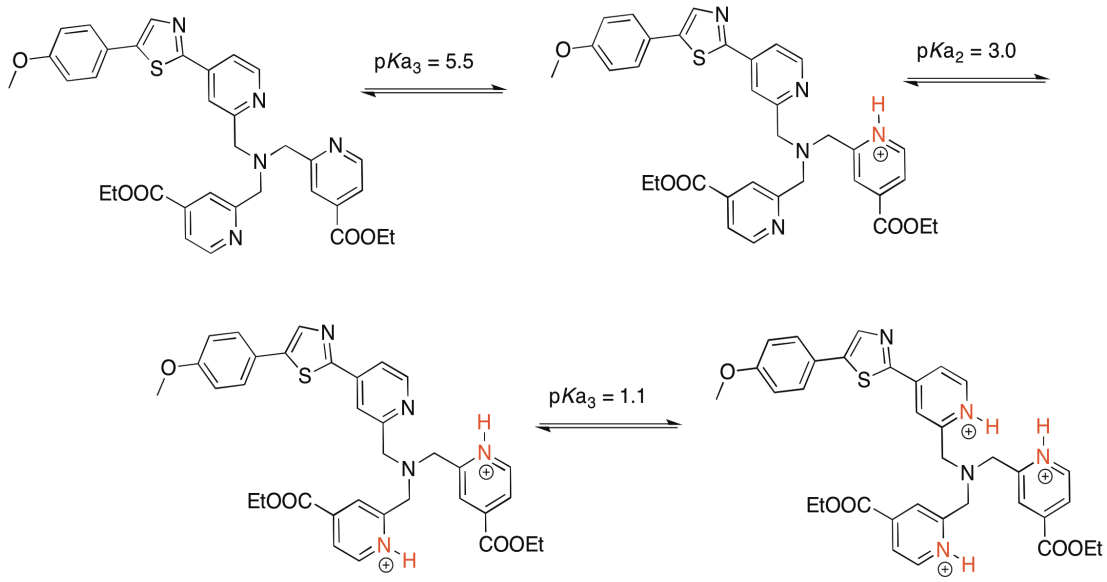

Scheme 2.1: Protonation constants of Chromis1.

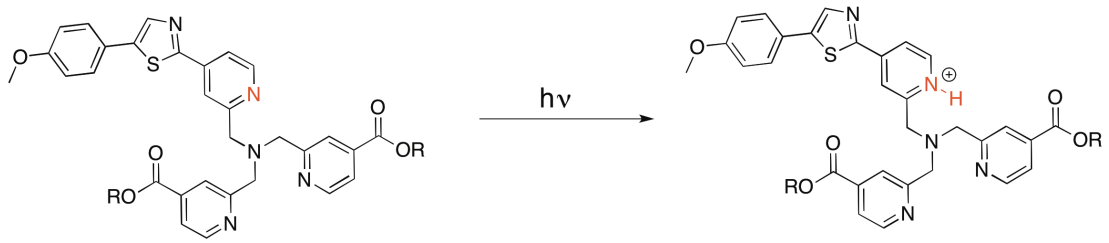

Scheme 2.2: Excited state proton transfer (ESPT) of Chromis1.

Bafilomycin acts as a specific inhibitor of vacuolar-type H^+-ATPase, thus rapidly neutralizing acidic compartments, including lysosomes, in cells.[45] Additionally, commercially available LysoTracker dyes can be used to track acidic organelles.[46] These sensors consist of a fluorophore linked to a weak base that is only partially protonated at neutral pH. As cell permeable probes, LysoTracker dyes can be used to identify acidic compartments in live cells based on standard fluorescence microscopy imaging approaches. With absorption and emission maximums at 577 nm and 590 nm, respectively, LysoTracker Red was specifically selected due to the lack of spectral overlap with Chromis1-ester. To rule out pH dependence of the Zn(II)-selective probe, NIH 3T3 fibroblasts co-stained with Chromis1-ester and LysoTracker Red were imaged in real-time before and after the addition of Bafilomycin. Cells stained with LysoTracker Red have a distinct fluorescence in basal conditions that attenuates dramatically when neutralized by the introduction of Bafilomycin. The emission ratio response of Chromis1-ester will determine the probe's sensitivity to intracellular fluctuations of pH. If attenuation occurs, the Zn(II)-selective sensor is sensitive to changes in pH, however, retaining its fluorescence intensity ratio after neutralization will suggest that Chromis1-ester is not associated with acidic compartments.

NIH 3T3 cells were treated with 10 μM Chromis1-ester and 6 nM LysoTracker Red for 60 minutes at 37°C in a 5% CO_2 atmosphere. The cells were then transferred to a temperature-controlled chamber mounted on the microscope stage. Both Chromis1-ester and LysoTracker Red could not be imaged simultaneously. The two-photon laser excitation of Chromis1-ester at 720 nm was followed by 561 nm excitation of LysoTracker Red, alternating between two channels after each complete scan. Each individual scan took 20 seconds to complete, therefore each set of Chromis1-ester and LysoTracker Red images took 40 seconds. After 15 minutes of imaging under basal conditions, Bafilomycin was added to the imaging dish to a final concentration of 900 nM.

As indicated in Figure 2.8, the addition of Bafilomycin caused immediate attenuation of LysoTracker Red emission, therefore, indicating the successful inhibition of vacuolar-type H^+-ATPase and intracellular neutralization. A sharp line across the resulting kymograph (Figure 2.8B) illustrates the abrupt change in LysoTracker Red emission. Conversely, negligible change is detected in the fluorescence emission of Chromis1-ester after neutralization (Figure 2.8C). This suggests the fluorescence emission of Chromis1-ester during live cell imaging is not a product of fluctuations in pH.

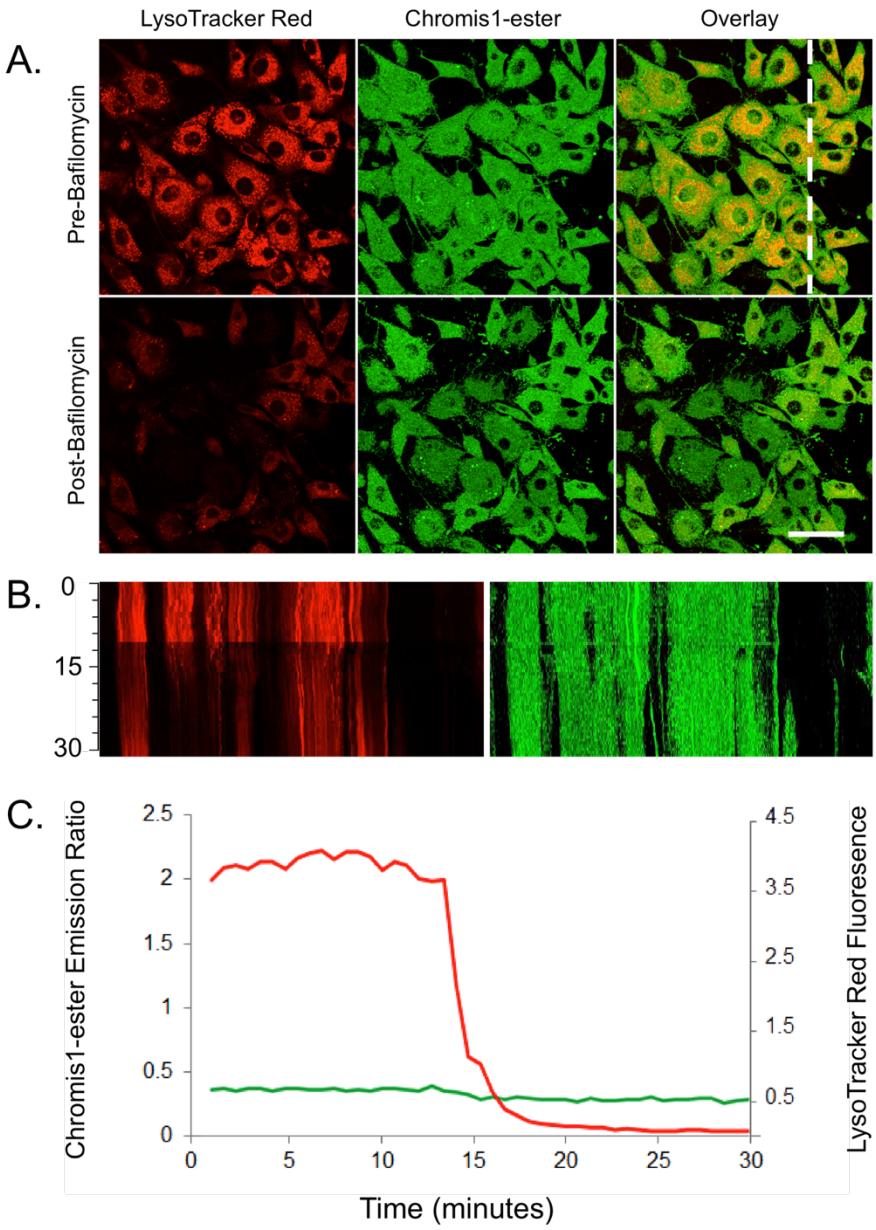

Figure 2.8: Chromis1-ester response to neutralization via Bafilomycin. Imaging of Chromis1-ester and LysoTracker Red treated live NIH 3T3 fibroblasts. Cells were pre-treated with 10 µM Chromis1-ester and 6 nM LysoTracker Red then imagined in a temperature-controlled chamber using a Zeiss LSM710. The cells were then exposed to 900 nM Bafilomycin. **A:** False color imaging pre- and post-Bafilomycin addition of LysoTracker Red (left), Chromis1-ester (center) and an overlay of the two (right). Scale bar = 50 µm. **B.** False color kymographs of LysoTracker Red (left) and Chromis1-ester (right) for the region of interest shown as a dotted white line in upper right panel of (A). Time scale on the far left, 0 – 30 minutes. **C.** Average intensity of emission ratio of Chromis1-ester (green line) and the fluorescence of LysoTracker Red (red line) over the 30 minutes of time-lapse imagining. Two-photon excitation of Chromis1-ester occurred at 720 nm and emission was collected between 425-462 and 478-540 nm. LysoTracker Red was excited using a 561 nm laser and emission was collected between 584-612 nm.

2.4 Monitoring Endogenous Zn(II)

The previous experiment monitoring exogenous changes in zinc concentration confirmed the ability of Chromis1-ester to detect high concentrations (100 μM) of $ZnSO_4$/pyrithione added to the imaging media. Before adding the exogenous zinc, the probe appears to primarily be in apo-form, not bound to any zinc at all. The exogenous zinc inundated the cells and saturated Chromis1-ester almost entirely. While this does confirm the probe can detect fluctuations in zinc, it is unknown if Chromis1-ester can detect endogenous zinc changes. It is important to determine if Chromis1-ester can detect zinc ion transients when they are induced specifically in biologically meaningful ways before assuming the probe can detect fluctuations that occur naturally.

2.4.1 Oxidative Stress Induced Release of Endogenous Zn(II)

In order to induce intracellular zinc ion fluctuations in a biologically relevant manner, strong oxidizing agents were applied to the cells to oxidize the zinc/thiolate sites in redox regulated proteins, such as metallothionein (MT), resulting in zinc dissociation (Scheme 2.3).[47,48] This procedure mimics the naturally occurring oxidative chemical processes that regulate and mobilize zinc from MT. Specifically, redox reactions will occur between the sulfur compounds of different oxidation states and consequentially, the disulfides will release zinc from the zinc/thiolate sites by thiol/disulfide exchange reactions.[49,50] The free zinc would then be accessible to Chromis1-ester, allowing the probe to detect the increase in available zinc and undergo a shift in emission. For these experiments hydrogen peroxide (H_2O_2) and 2,2′-dithiodipyridine (DTDP) were applied individually and an influx of available Zn(II) for Chromis1-ester to bind was expected to increase in the ratio similar to what is observed with the addition of exogenous Zn(II) (Figure 2.4).

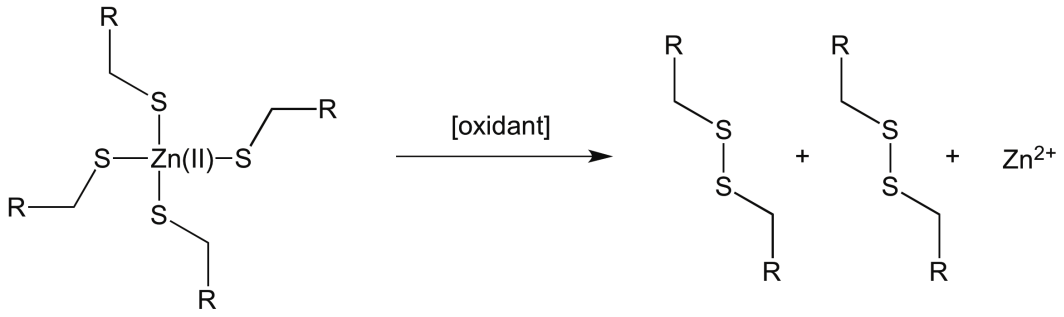

Scheme 2.3: Proposed mechanism of zinc dissociation by oxidation of sulfur donors.

NIH 3T3 cells were grown glass bottom culture dishes (MatTek), treated with 10 μM Chromis1-ester for 30 minutes at 37°C and transferred to a temperature-controlled chamber mounted on the microscope stage. Images were acquired every 20 seconds. During basal imaging the cells indicate a low intensity ratio of 0.6 dispersed uniformly throughout the cell cytoplasm (Figure 2.9). After 33 minutes acquiring images of cells under basal conditions, the cells were exposed to a buffer solution containing 50 μM H_2O_2, causing the fluorescence ratio to increase to as high as 2.5 around both the extracellular and intracellular membranes surrounding the nucleus. The ratio in the cytoplasm reached approximately 1.6. Roughly 25 minutes after the addition of H_2O_2, the ratio decreased independent of any additional reagents reaching approximately 0.7 after 45 minutes.

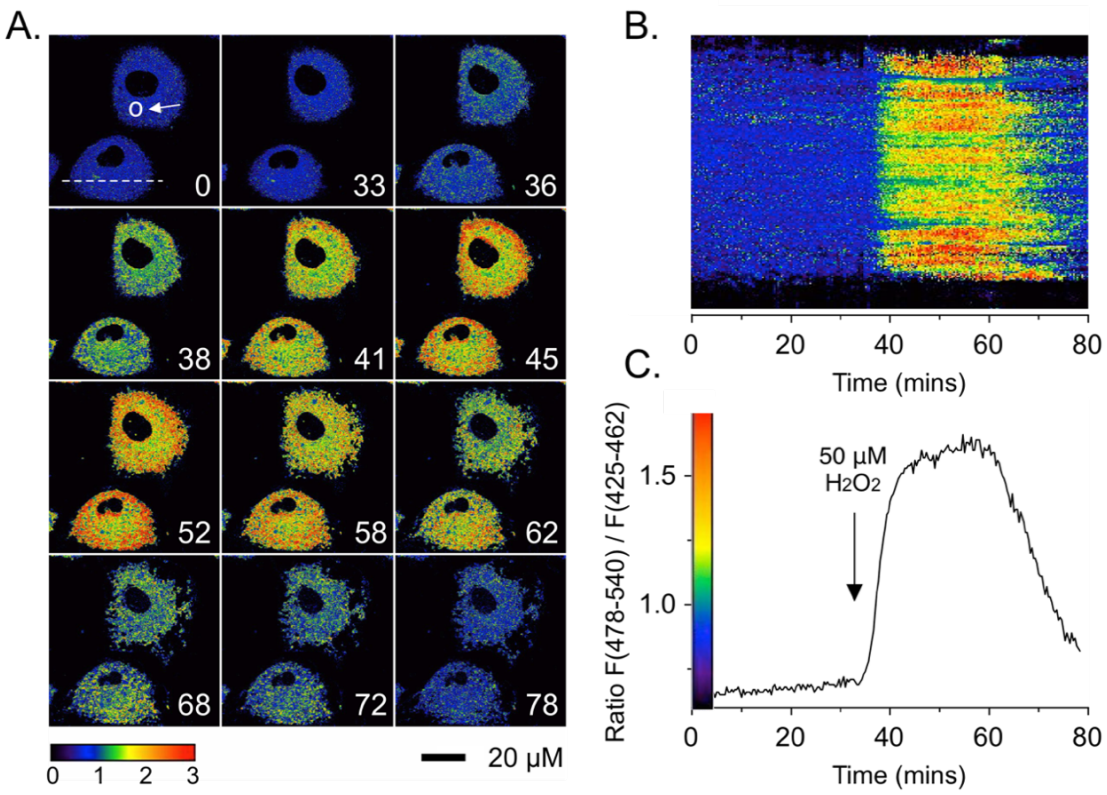

Figure 2.9: Ratiometric response to oxidative stress via H_2O_2. Two-photon excited ratiometric imaging of Zn(II) fluxes in live NIH 3T3 fibroblasts. Cells were pre-treated with 10 µM Chromis1-ester (30 min) and imaged in a temperature-controlled chamber using a Zeiss LSM710. The cells were then exposed to a buffer solution containing 50 µM H_2O_2. **A**: False color ratiometric images acquired at the indicated time points (minutes in lower right corner of images). **B**: False color ratiometric kymograph for the region of interest indicated by the dotted line in the upper left panel of (A). **C:** Average intensity ratio change vs. time from region of interest indicated by the white circle in the upper left panel of (A). Two-photon excitation occurred at 720 nm. Emission was collected between 425-462 and 478-540 nm.

Further oxidative stress experiments were performed using DTDP to induce a release of endogenous intracellular Zn(II). NIH 3T3 cells were treated with 10 μM Chromis1-ester for 30 minutes at 37°C and transferred to a temperature-controlled chamber mounted on the microscope stage. After 10 minutes of imaging under basal conditions cells were exposed to a buffer solution containing 100 μM DTDP (Figure 2.10), causing the fluorescence ratio to increase from a basal ratio of 0.5 to as high as 1.8 around both the extracellular and intracellular membranes surrounding the nucleus. The ratio in the cytoplasm reached approximately 1.5. Roughly 40 minutes after the addition DTDP, the ratio began to decrease independent of any additional reagents. Approximately 70 minutes following the addition of DTDP, the ratio completely returned to 0.5.

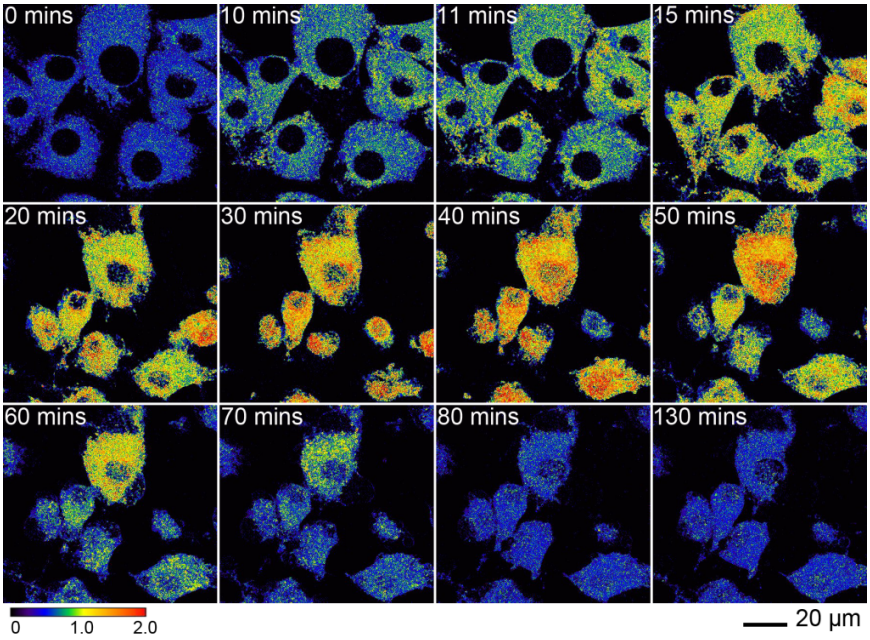

Figure 2.10: Ratiometric response to oxidative stress via DTDP. Two-photon excited ratiometric imaging of endogenous Zn(II) fluxes in live fibroblasts induced by DTDP. Cells were pre-treated with 10 μM Chromis1-ester (30 min) and imagined in a temperature-controlled chamber using a Zeiss LSM710. After 10 minutes of imaging under basal conditions, the cells were exposed to a buffer solution containing 100 μM DTDP. False color ratiometric images acquired at the indicated time points. Two-photon excitation occurred at 720 nm. Emission was collected between 425-462 and 478-540 nm.

2.4.2 Imaging Labile Zn(II) in Mitosis

As previously mentioned, zinc is essential to cell proliferation and cell-cycle dependent zinc fluxes have been observed. SXRF microscopy on NIH 3T3 fibroblasts in various stages of cell division revealed a 2 to 3-fold increase along with distinct redistribution patterns of zinc during mitosis.[1] It is unclear if this influx of zinc is tightly bound to proteins or labile. Chromis1-ester was used to investigate labile zinc distribution of live, dividing cells.

NIH 3T3 cells were grown on glass bottom culture dishes, treated with 10 μM Chromis1-ester for 30 minutes at 37°C with 5% CO_2 and transferred to a temperature-controlled chamber mounted on the microscope stage. Cells were maintained in this incubation chamber on the Zeiss LSM710 microscope stage for the duration of the experiment. Images were acquired every 5 seconds for approximately 15 minutes using a 63x objective. As illustrated in Figure 2.11A and Figure 2.11B, cells in G_1 and M phases appear to retain a steady ratio between 0.50 and 0.65, indicating mostly the apo-form of Chromis1-ester, throughout the duration of imaging. Faint vesicular structures noticeable in the dividing fibroblast have a slightly higher ratio than the rest of the cell.

Additional experiments using similar preparation protocols were performed to visualize proliferating cells in a larger area over an extended amount of time. Images in this experiments were acquired every 2 minutes over four and a half hours using a 20x objective. Chromis1-ester was not toxic to the cells, nor did it attenuate or photobleach, keeping its initial fluorescence for the duration of the experiment. Outliers were also observed with some cells demonstrating higher ratios than others (Figure 2.11C).

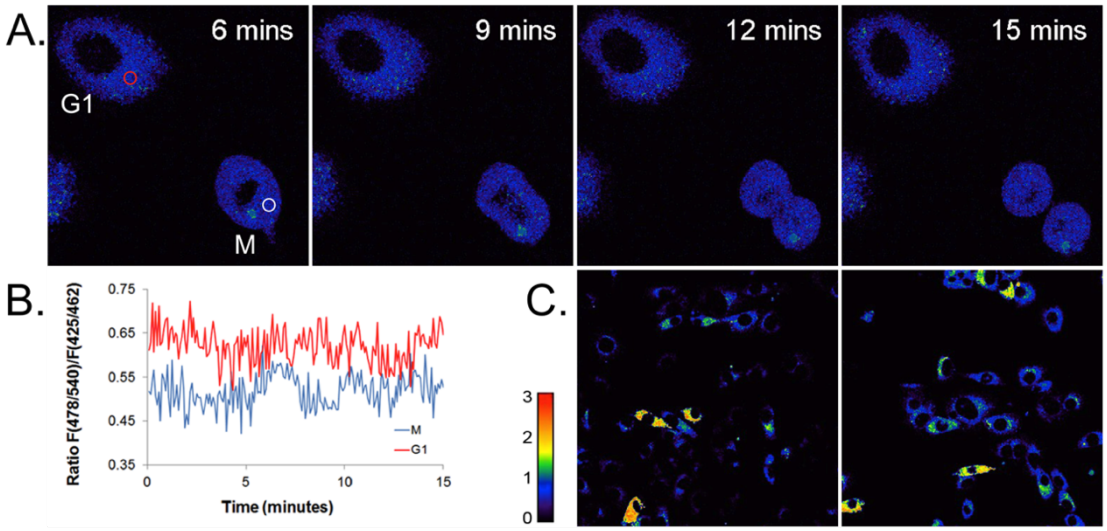

Figure 2.11: Live cell imaging of labile zinc during mitosis. Two-photon excited ratiometric imaging of Zn(II) in live NIH 3T3 fibroblasts. Cells were grown on glass bottom culture dishes, incubated with 10 μM Chromis1-ester (30 min), and transferred to a temperature-controlled chamber mounted on the microscope stage. All images were obtained in basal conditions. **A**: False color ratiometric images acquired at the indicated time points using a 63x objective. Cell labeled "G1" does not divide, while cell labeled "M" divides in 15 minutes. **B**: Average intensity ratio change vs. time for the regions of interest (ROI) shown as circles in the left panel of (A). The ROI of the G1 cell is denoted with a red circle in (A) and a red line in (B). The ROI of the M cell is denoted with a white circle in (A) and a blue line in (B). The ratio of the G1 cell averages between 0.55 - 0.70 and the dividing cell, M, averages between 0.45 - 0.60. **C**: Overview of two large areas on the dish using a 20x objective demonstrating the heterogeneous distribution of zinc between cells. Two-photon excitation occurred at 720 nm, the emission was collected between 425 - 462 and 478 - 540 nm.

2.5 Conclusions

Chromis1-ester has been thoroughly characterized in NIH 3T3 fibroblasts as a ratiometric Zn(II)-selective probe capable of detecting both exogenous and endogenous zinc fluxes. In a neutralization experiment, Chromis1-ester confirmed it is not sensitive to intracellular pH fluctuations. Localization experiments revealed a small amount of spatial correlation in Zn(II) labile pools and lipid droplets, but not with mitochondria or the ER. Additionally, proliferating NIH 3T3 fibroblasts were imaged over extended periods of time without photobleaching of Chromis1-ester or noticeable harm to the cells. These data also revealed some cells to have a higher ratio than others, indicating a heterogeneous distribution of labile Zn(II) between individual cells. Lastly, neither the 2 to 3-fold influx nor the distinct redistribution pattern of zinc observed by SXRF microscopy in dividing cells was reproduced by the labile Zn(II) visualized via Chromis1-ester. Therefore, the influx of Zn(II) observed in the SXRF microscopy data is likely bound to ligands with a higher affinity than the Zn(II)-selective fluorescent probe, Chromis1-ester.

2.6 Materials and Methods

2.6.1 Cell Culture and Reagents

NIH 3T3 mouse fibroblasts were cultured in Dulbecco's modified Eagle's medium (DMEM, GIBCO) supplemented with 10% bovine serum (GIBCO), penicillin/streptomycin (50 IU/mL), 200 μM L-glutamine, and 100 μM sodium pyruvate at 37°C under an atmosphere of humidified air containing 5% CO_2. Imaging media was prepared using fully supplemented (10% bovine serum, 50 IU/mL penicillin/streptomycin, 200 μM L-glutamine, and 100 μM sodium pyruvate) DMEM containing 25 mM HEPES buffer and without phenyl-red. Both the culture media and imaging media were sterilized by filtration through 0.2 μm filters.

2.6.2 In Situ Characterization of Chromis1

NIH 3T3 mouse fibroblasts were grown on glass bottom culture dishes (MatTek) to 70% confluency then incubated with 10 μM Chromis1-ester in un-supplemented DMEM for 15 minutes at 37˚C in a 5% CO_2 atmosphere. DMEM/Chromis1 was then aspirated and replaced with pre-warmed imaging media before mounting the dish on the microscope stage enclosed in an incubation box equipped to maintain 37˚C and humid, 5% CO_2 atmosphere. All imaging experiments were performed using a Zeiss LSM Confocal/NLO 710 microscope with a pulsed IR/multiphoton laser tuned to 720 nm for excitation of Chromis1-ester. Both 20x and 63x (oil-immersion) objectives were used. The fluorescence emission of Chromis1-ester was collected in two separate channels simultaneously: (1) 425-462 nm and (2) 478-540 nm.

Ratiometric emission response was stimulated via $ZnSO_4$:pyrithione (100 μM:10 μM), followed by a perfusion with 100 μM of a cell permeable, non-fluorescent, high-affinity Zn(II) chelator, N,N,N',N'-tetrakis-(2-pyridylmethyl)-ethylenediamine (TPEN). Oxidative stress response was stimulated by exposure to a buffer solution containing either 50 μM hydrogen peroxide (H_2O_2) or 100 μM 2,2′-dithiodipyridine (DTDP). The effect of pH was monitored using cells simultaneously treated with 10 μM Chromis1-ester and 6 nM LysoTracker Red (Invitrogen) in DMEM (without additives) for 60 minutes at 37°C in a 5% CO_2 atmosphere. After roughly 15 minutes of imaging under basal conditions in fully supplemented imaging media, 900 nM of Bafilomycin (Sigma) was added to the dish.

2.6.3 Localization of Chromis1

NIH 3T3 mouse fibroblasts were cultured onto glass bottom dishes (MatTek). Upon reaching 30-40% confluency, cells were transfected using 200 μL non-supplemented DMEM, 4 μL Turbofect (Thermo Scientific) and 2 μg of either pDs_Red2-mito or pEYFP-ER plasmids for mitochondria or ER respectively. After 24 hours, the regular growth media

supplemented with the plasmid was replaced with pre-warmed imaging media and cells were imaged on a Zeiss LSM Confocal/NLO 710 microscope with a 63x oil-immersion objective. Fluorescence emissions of both Chromis1-ester and the fluorescent organelle marker were collected simultaneously with the laser and filters settings switching on a line-by-line basis. Chromis1-ester: excitation via a pulsed IR/multiphoton laser tuned to 720 nm, emission collected from 400 - 498 nm. pDs_Red2-mito: excitation at 561 nm, emission collected from 570 - 700 nm. pEYFP-ER: excitation at 514 nm, emission collected from 525 - 675 nm.

Cells were co-stained with 10 μM Chromis1-ester and 2 μM BODIPY 493/503 (4,4-Difluoro-1,3,5,7,8-Pentamethyl-4-Bora-3a,4a-Diaza-*s*-Indacene, Molecular Probes), a fluorescent indicator of neutral lipids, for 30 minutes. Fluorescence emission of Chromis1 and BODIPY 493/503 were collected simultaneously with the laser and filters settings switching on a line-by-line basis. Chromis1-ester: excitation via a pulsed IR/multiphoton laser tuned to 720 nm, emission collected from 400 - 498 nm. BODIPY 493/503: excitation at 488 nm, emission collected from 525 - 675 nm.

2.6.4 Image Processing

The quantitative image analysis software package, Image J,[37] was used to analyze the change in the fluorescence emission ratio of Chromis1 over time. The ratio values and their corresponding time points were graphed using ProFit software.

2.7 Literature Cited

1. McRae, R., Lai, B. & Fahrni, C.J. Subcellular redistribution and mitotic inheritance of transition metals in proliferating mouse fibroblast cells. *Metallomics* **5**, 52-61 (2013).

2. MacDonald, R.S. The role of zinc in growth and cell proliferation. *Journal of Nutrition* **130**, 1500S-1508S (2000).

3. Beyersmann, D. & Haase, H. Functions of zinc in signaling, proliferation and differentiation of mammalian cells. *Biometals* **14**, 331-341 (2001).

4. Paski, S.C. & Xu, Z.M. Labile intracellular zinc is associated with 3T3 cell growth. *Journal of Nutritional Biochemistry* **12**, 655-661 (2001).

5. Wang, Y.H., Li, K.J., Mao, L., Hu, X., Zhao, W.J., Hu, A., Lian, H.Z. & Zheng, W.J. Effects of exogenous zinc on cell cycle, apoptosis and viability of MDAMB231, HepG2 and 293 T Cells. *Biological Trace Element Research* **154**, 418-426 (2013).

6. Li, Y. & Maret, W. Transient fluctuations of intracellular zinc ions in cell proliferation. *Experimental Cell Research* **315**, 2463-2470 (2009).

7. Colvin, R.A., Holmes, W.R., Fontaine, C.P. & Maret, W. Cytosolic zinc buffering and muffling: Their role in intracellular zinc homeostasis. *Metallomics* **2**, 306-317 (2010).

8. Krezel, A. & Maret, W. Zinc-buffering capacity of a eukaryotic cell at physiological pZn. *Journal of Biological Inorganic Chemistry* **11**, 1049-1062 (2006).

9. Maret, W. Analyzing free zinc(II) ion concentrations in cell biology with fluorescent chelating molecules. *Metallomics* **7**, 202-211 (2015).

10. Kambe, T. Introduction: "Zinc Signaling" - The Blossoming Field of Zinc Biology. in *Zinc Signals in Cellular Functions and Disorders* (eds. Fukada, T. & Kambe, T.) 1-5 (Springer, Tokyo, 2014).

11. Krezel, A. & Maret, W. Zinc-buffering capacity of a eukaryotic cell at physiological pZn. *J. Biol. Inorg. Chem.* **11**, 1049-1062 (2006).

12. Qin, Y., Dittmer, P.J., Park, J.G., Jansen, K.B. & Palmer, A.E. Measuring steady-state and dynamic endoplasmic reticulum and Golgi Zn2+ with genetically encoded sensors. *Proceedings of the National Academy of Sciences of the United States of America* **108**, 7351-7356 (2011).

13. Vinkenborg, J.L., Nicolson, T.J., Bellomo, E.A., Koay, M.S., Rutter, G.A. & Merkx, M. Genetically encoded FRET sensors to monitor intracellular Zn2+ homeostasis. *Nature Methods* **6**, 737-U10 (2009).

14. Deranlea, D.A. Theory of measurement of weak molecular complexes .2. Consequences of multiple equilibria. *Journal of the American Chemical Society* **91**, 4050 (1969).

15. Deranleau, D.A. Theory of measurement of weak molecular complexes .I. General considerations. *Journal of the American Chemical Society* **91**, 4044 (1969).

16. Grynkiewicz, G., Poenie, M. & Tsien, R.Y. A new generation of Ca2+ indicators with greatly improved fluorescence properties. *Journal of Biological Chemistry* **260**, 3440-3450 (1985).

17. Gee, K.R., Zhou, Z.L., Ton-That, D., Sensi, S.L. & Weiss, J.H. Measuring zinc in living cells. A new generation of sensitive and selective fluorescent probes. *Cell Calcium* **31**, 245-251 (2002).

18. Thompson, R.B., Peterson, D., Mahoney, W., Cramer, M., Maliwal, B.P., Suh, S.W., Frederickson, C., Fierke, C. & Herman, P. Fluorescent zinc indicators for neurobiology. *Journal of Neuroscience Methods* **118**, 63-75 (2002).

19. Maruyama, S., Kikuchi, K., Hirano, T., Urano, Y. & Nagano, T. A novel, cell-permeable, fluorescent probe for ratiometric imaging of zinc ion. *Journal of the American Chemical Society* **124**, 10650-10651 (2002).

20. Lim, N.C. & Bruckner, C. DPA-substituted coumarins as chemosensors for zinc(II): Modulation of the chemosensory characteristics by variation of the position of the chelate on the coumarin. *Chemical Communications*, 1094-1095 (2004).

21. Chang, C.J., Jaworski, J., Nolan, E.M., Sheng, M. & Lippard, S.J. A tautomeric zinc sensor for ratiometric fluorescence imaging: Application to nitric oxide-induced release of intracellular zinc. *Proceedings of the National Academy of Sciences of the United States of America* **101**, 1129-1134 (2004).

22. Taki, M., Wolford, J.L. & O'Halloran, T.V. Emission ratiometric imaging of intracellular zinc: Design of a benzoxazole fluorescent sensor and its application in two-photon microscopy. *Journal of the American Chemical Society* **126**, 712-713 (2004).

23. Woodroofe, C.C. & Lippard, S.J. A novel two-fluorophore approach to ratiometric sensing of Zn2+. *Journal of the American Chemical Society* **125**, 11458-11459 (2003).

24. Woodroofe, C.C., Won, A.C. & Lippard, S.J. Esterase-activated two-fluorophore system for ratiometric sensing of biological zinc(II). *Inorganic Chemistry* **44**, 3112-3120 (2005).

25. Kiyose, K., Kojima, H., Urano, Y. & Nagano, T. Development of a ratiometric fluorescent zinc ion probe in near-infrared region, based on tricarbocyanine chromophore. *Journal of the American Chemical Society* **128**, 6548-6549 (2006).

26. Komatsu, K., Urano, Y., Kojima, H. & Nagano, T. Development of an iminocoumarin-based zinc sensor suitable for ratiometric fluorescence imaging of

neuronal zinc. *Journal of the American Chemical Society* **129**, 13447-13454 (2007).

27. Tomat, E. & Lippard, S.J. Ratiometric and intensity-based zinc sensors built on rhodol and rhodamine platforms. *Inorganic Chemistry* **49**, 9113-9115 (2010).

28. Xu, Z., Baek, K.-H., Kim, H.N., Cui, J., Qian, X., Spring, D.R., Shin, I. & Yoon, J. Zn2+-Triggered amide tautomerization produces a highly Zn2+-selective, cell-permeable, and ratiometric fluorescent sensor. *Journal of the American Chemical Society* **132**, 601-610 (2010).

29. Dittmer, P.J., Miranda, J.G., Gorski, J.A. & Palmer, A.E. Genetically encoded sensors to elucidate spatial distribution of cellular zinc. *Journal of Biological Chemistry* **284**, 16289-16297 (2009).

30. Zipfel, W.R., Williams, R.M. & Webb, W.W. Nonlinear magic: multiphoton microscopy in the biosciences. *Nature Biotechnology* **21**, 1368-1376 (2003).

31. Oheim, M., Michael, D.J., Geisbauer, M., Madsen, D. & Chow, R.H. Principles of two-photon excitation fluorescence microscopy and other nonlinear imaging approaches. *Advanced Drug Delivery Reviews* **58**, 788-808 (2006).

32. Tauer, U. Advantages and risks of multiphoton microscopy in physiology. *Experimental Physiology* **87**, 709-714 (2002).

33. Pierrel, F., Cobine, P.A. & Winge, D.R. Metal Ion availability in mitochondria. *Biometals* **20**, 675-682 (2007).

34. Atkinson, A. & Winge, D.R. Metal acquisition and availability in the mitochondria. *Chemical Reviews* **109**, 4708-4721 (2009).

35. Babula, P., Masarik, M., Adam, V., Eckschlager, T., Stiborova, M., Trnkova, L., Skutkova, H., Provaznik, I., Hubalek, J. & Kizek, R. Mammalian metallothioneins: Properties and functions. *Metallomics* **4**, 739-750 (2012).

36. Maret, W. Zinc coordination environments in proteins as redox sensors and signal transducers. *Antioxidants & Redox Signaling* **8**, 1419-1441 (2006).

37. Schneider, C.A., Rasband, W.S. & Eliceiri, K.W. NIH Image to ImageJ: 25 years of image analysis. *Nature Methods* **9**, 671-675 (2012).

38. Adler, J. & Parmryd, I. Quantifying colocalization by correlation: The Pearson correlation coefficient is superior to the Mander's overlap coefficient. *Cytometry Part A* **77A**, 733-742 (2010).

39. Dunn, K.W., Kamocka, M.M. & McDonald, J.H. A practical guide to evaluating colocalization in biological microscopy. *American Journal of Physiology-Cell Physiology* **300**, C723-C742 (2011).

40. Yamasaki, S., Sakata-Sogawa, K., Hasegawa, A., Suzuki, T., Kabu, K., Sato, E., Kurosaki, T., Yamashita, S., Tokunaga, M., Nishida, K. & Hirano, T. Zinc is a novel intracellular second messenger. *Journal of Cell Biology* **177**, 637-645 (2007).

41. Hogstrand, C., Kille, P., Nicholson, R.I. & Taylor, K.M. Zinc transporters and cancer: A potential role for ZIP7 as a hub for tyrosine kinase activation. *Trends in Molecular Medicine* **15**, 101-111 (2009).

42. Lin, H.-J., Herman, P. & Lakowicz, J.R. Fluorescence lifetime-resolved pH imaging of living cells. *Cytometry Part A* **52A**, 77-89 (2003).

43. Roos, A. & Boron, W.F. Intracellular pH. *Physiological Reviews* **61**, 296-434 (1981).

44. Cooper, G.M. *The Cell: A Molecular Approach*, (ASM Press, 2000).

45. Yoshimori, T., Yamamoto, A., Moriyama, Y., Futai, M. & Tashiro, Y. Bafilomycin-A1, a specific inhibitor of vacuolar-type H+-ATPase, inhibits acidification and protein-degradation in lysosomes of cultured-cells. *Journal of Biological Chemistry* **266**, 17707-17712 (1991).

46. Diwu, Z., Zhang, Y.-z. & Hauglan, R.P. Novel probes and methods. *Cytometry* **18**, 74-77 (1994).

47. Krezel, A., Hao, Q. & Maret, W. Zinc/thiolate redox biochemistry of metallothionein and the control of zinc ion fluctuations in cell signaling. *Archives of Biochemistry and Biophysics* **463**, 188-200 (2007).

48. Maret, W. The function of zinc metallothionein: A link between cellular zinc and redox state. *Journal of Nutrition* **130**, 1455S-1458S (2000).

49. Maret, W. Metallothionein disulfide interactions, oxidative stress, and the mobalization of cellular zinc. *Neurochemistry International* **27**, 111-117 (1995).

50. Maret, W. Oxidative metal release from metallothionein via zinc thiol-disulfide interchange. *Proceedings of the National Academy of Sciences of the United States of America* **91**, 237-241 (1994).

CHAPTER 3

3D IMAGING OF TRANSITION METALS IN THE ZEBRAFISH EMBRYO BY X-RAY FLUORESCENCE MICROTOMOGRAPHY

Previous X-ray fluorescence imaging studies of NIH 3T3 fibroblasts revealed an intriguing redistribution of zinc and copper during cell division with a 2 to 3-fold increase of zinc at the onset of mitosis compared to interphase cells.[1] In the case of in vitro cell cultures, the increased zinc demand can be readily met through import of exogenous zinc from the surrounding growth medium. In contrast, developing embryos of fish, reptiles, birds, or primitive mammals are self-sufficient during early development and retrieve most nutrients from the yolk enclosed within an extraembryonic membrane.[2,3] As the essential transition metal requirements vary widely between organs,[4,5] the developing embryo is most likely forced to redistribute the limited supply of trace nutrients during development to meet these demands.

In this chapter, synchrotron X-ray fluorescence (SXRF) microtomography is utilized to image the distribution of zinc, iron and copper with 2 – 3 μm resolution of zebrafish embryos in the pharyngula and hatching periods, approximately 24 and 48 hours post fertilization (hpf) respectively. Using both the established progressive lowering of temperature method (PLT) with femtosecond-based two-photon laser sectioning the specimen's structural integrity is preserved inside a polymer block. Post-acquisition data processing was accomplished using the iterative maximum likelihood expectation maximization (MLEM) algorithm, reducing the noise level and streak artifacts allowing data to be clearly visualized and examined in a true three-dimensional state. These data revealed new insights into the spatial distribution of transition metals during these key time points in embryogenesis.

3.1 Background

Transition metals, such as zinc, iron, and copper, are vital trace nutrients necessary for all forms of life. They are essential components of numerous enzymes, proteins and reactions required for cell proliferation,[6,7] cell differentiation,[8,9] growth[7,10] and development.[11-13] For example, the availability of zinc, iron or copper can have great impacts during pregnancy. Deficiencies of any one of these essential nutrients can lead to severe complications including low birth weight, premature delivery, and structural and biochemical abnormalities of the fetus.[12,14,15] Despite the established importance of transition metals in development, little is understood regarding the redistribution and organization of zinc, iron and copper during embryogenesis. To understand the regulating mechanisms of transition metal homeostasis, a detailed knowledge of the metal ion distribution inside cells, tissues and whole organisms is essential.

Zebrafish present an ideal model system when studying metal distribution during embryogenesis. These embryos develop as lecithotrophic organisms requiring only the nutrition found in their yolk sac.[2] Zebrafish can survive on this nutrition source for 3 - 4 days post fertilization (dpf) before the embryo requires exogenous feeding.[16] They are essentially a closed system already containing all essential nutrients, including trace metals, needed for the first few days of development.

What begins as a single cell containing a defined, fixed amount of trace metals develops into a multicellular organism comprised of various cells, tissues, and organs all with varying trace metal requirements.[4,5] Given the limited external supply of nutrients during embryogenesis, developing organs most likely redistribute zinc from neighboring cells to satisfy their increased demand, thus raising the question of how the limited supplies of zinc in a fertilized egg is redistributed in the course of embryonic development. The ability to image this elemental distribution in biological samples can be challenging due to the small size of embryos and the small amount of trace metals

each embryo contains. Bulk analysis techniques do not provide a detailed image of the metal ion distribution inside an individual embryo, therefore microanalytical techniques are ideal.

3.1.1 Microanalytical Techniques Used for Trace Metal Imaging

While numerous microanalytical techniques exist, each presents its own set of advantages and limitations. When selecting an analytical technique one must consider the method's sensitivity to detect trace concentrations of elements, spatial resolution to clearly visualize metals within cellular structures, and selectivity to accurately detect multiple elements. Electron-probe energy-dispersive spectroscopy (EDS), laser ablation – inductively coupled plasma – mass spectrometry (LA-ICP-MS), secondary ion mass spectrometry (SIMS), proton beam microprobe – particle induced X-ray emission (PIXE), and synchrotron x-ray fluorescence (SXRF) microscopy, are each capable of quantitatively mapping the trace elemental distributions within biological samples at micron to submicron resolution.[17-24]

In order to study the trace metal distribution of zebrafish embryos, a quantitative, sensitive (< 1 μg/g) method with high spatial resolution capable of imaging thick (>1 mm), hydrated biological samples is required. These restrictions eliminate most available microanalytical techniques as suitable methods (Table 3.1). EDS utilizes scanning electron microscopes fitted with energy dispersive X-ray detectors to determine the elemental composition of a sample.[25] While EDS is capable of very fine spatial resolution of 0.03 μm and is well-suited for cellular localization imaging, this technique is not sensitive enough. Furthermore, only vacuum compatible materials can be analyzed due to the sample chamber under vacuum pressure, a requirement of all electron column techniques.[26] PIXE uses nuclear microprobes to simultaneously detect over 20 elements. Using a tightly focused proton beam, this method stimulates X-ray emission

while scanning across the surface of the sample, therefore detecting the lateral distribution of elements.[27] The proton beam utilized in PIXE has a 10-fold improvement of sensitivity compared to EDS. This method also does not posses the analytical depth required for imaging zebrafish. Additionally, PIXE requires the sample to be analyzed under vacuum pressure, thereby eliminating the option to use hydrated specimens.[27] SIMS uses a focused primary ion beam consisting of heavy particles to bombard the specimen causing charged particles (secondary ions) to be ejected from the sample surface. The secondary ions are then introduced to a mass spectrometer detector where they are identified by their mass-to-charge ratio to determine the elemental, isotopic, or molecular composition of the sample.[28] Capable of submicron spatial resolution (50 nm) and an analytical depth of 0.1 μm, SIMS is only utilized for sub-cellular localization studies of specimen such as thin cells or tissues.[29] Similar to EDS and PIXE, hydrated samples are not compatible with SIMS due to the required vacuum sample chamber. LA-ICP-MS is another widely used mass spectrometry technique for elemental analysis.[30-33] In this method, a short-pulsed, high-power laser beam instantaneously converts a finite volume of a solid sample into its vapor phase constituents. The ablated particles are then transferred to a second excitation source where a plasma torch further decomposes the particles into individual atomic ions. The ions are subsequently introduced to a mass spectrometer detector where they are identified by their mass-to-charge ratio.[31] The advantages of this technique are an analytical depth of 200 μm, the ability to apply this method directly to the solid sample and to quantitatively distinguish between individual isotopes with high accuracy and precision while a disadvantage is destroying the sample in the process.[30]

Table 3.1: Spatially resolved microanalytical techniques for quantitative imaging of trace metals[23,34,35]

Analytical Method	Detection Limit (µg/g)	Spatial Resolution (µm)	Analytical Depth (µm)	Quantification
Electron-probe energy-dispersive spectroscopy (EDS)[26,36]	100 - 1000	0.03	0.1 – 1	Semiquantitative
Proton beam microprobe – particle induced X-ray emission (PIXE)[27,37-40]	1 - 10	0.2 – 2	10 – 100	Quantitative
Synchrotron X-ray fluorescence microscopy (SXRF)[24]	0.1 – 1	0.03 – 0.2	> 100	Quantitative
Secondary ion mass spectrometry (SIMS)[28,41-43]	0.1 – 1	0.05 – 0.15	0.1	Quantitative
Laser ablation - inductively coupled plasma - mass spectrometry (LA-ICP-MS)[33,44-51]	0.01	> 1	200	Semiquantitative

While all of these techniques have their advantages, with a sensitivity of 0.1 - 1 µg/g and a spatial resolution of 0.03 – 0.2 µm, SXRF was the optimal choice. This limit of detection allows for study at the single cell level of embryos. Capable of an analytical depth greater than 100 µm and ability of analyzing hydrated samples, this technique is ideal for thick biological tissues such as zebrafish.

3.1.2 Synchrotron X-Ray Fluorescence Microtomography

Synchrotron X-ray fluorescence (SXRF) based imaging allows for the quantification of trace metals within hydrated cells and tissue sections to yield 2D distribution maps at submicron spatial resolution.[18-20,24] In this method, atoms of a sample are directly excited by an external X-ray source resulting in the expulsion of a core shell electron, creating a vacancy in the orbital and consequentially resulting in a

high energy, unstable configuration of the atom. To restore equilibrium, an electron from a higher energy, outer orbital fills the vacancy left by the expelled electron. In the process, the excess energy from the outer orbital electron is released in the form of a characteristic fluorescence emission unique to the specific element.

SXRF microtomography utilizes the two-dimensional SXRF information collected from many neighboring sections to create three-dimensional volumetric data. SXRF microscopy operates in the hard X-ray energy regime. This technique has been used to visualize the elemental distributions of thick hydrated tissues or small organisms such as nematodes[52] and 3 μm thick zebrafish eye sections;[53] however, the resulting 2D maps correspond to projections of the integrated metal content along the excitation trajectory and thus fail to provide unambiguous insights into the actual 3D structural organization. With advancements in X-ray imaging technology, such as the development of multi-element detectors electronics with improved sensitivity and 3rd generation synchrotron radiation light sources, visualization of 3D elemental distributions based on tomographic projections became possible.[54,55] For example, SXRF microtomography has been employed to study the iron distribution in wild-type and mutant *Arabidopsis* seeds lacking an iron uptake transporter,[56] and more recently, de Jonge et al. succeeded in visualizing the quantitative 3D elemental distribution in a diatom[57] and in *C. elegans*.[58]

In all previous examples, the elemental distribution was reconstructed from 2D SXRF projection maps, which were acquired by scanning the specimen through the stationary beam at varying projection angles. This approach requires that the sample has sufficient mechanical stability for mounting on a rotational stage. Additionally, long data acquisition times and matrix effects can create inhibitive challenges when applying SXRF tomography to obtain 3D elemental distributions. Therefore, although this method permits quantitative imaging of hydrated biological samples, SXRF tomography is

restricted to mechanically stable specimens capable of withstanding the long data acquisition times with microprecision.

3.1.3 X-Ray Fluorescence Imaging Optics

X-ray fluorescence imaging optics determines the ability to achieve desirable resolution or photon flux. Two of the most common methods of focusing X-ray beams to a submicron spot include Kirkpatrick-Baez (K-B) mirrors and Fresnel zone plates. A Fresnel zone plate consists of a series of concentric rings. These rings, referred to as "zones", become increasingly narrower the larger the radii and alternate between opaque and transparent. They are specifically spaced so the diffracted light by the transparent zones constructively interferes at the desired focus. As X-rays hit the Fresnel zone plate it will diffract around the opaque zones. With this method, focal length is dependent on the X-ray energy. Alternatively, K-B mirrors consist of two spherical or cylindrical mirrors in a crossed configuration where the surface of the first mirror is aligned horizontally and the second is aligned vertically.[59] Both mirrors are curved elliptically in order to set the horizontal focus line of the first mirror and the vertical focus line of the second mirror in the same plane to create a single focal point. These curved mirrors have adjustable bend radii to achieve optimum focus at different wavelengths. This system typically produces beam sizes focused to 1-5 μm but can create focal diameters as small as 50 nm.[60] Both the Fresnel zone plate and the K-B mirrors have advantages and limitations. The Fresnel zone plate offers higher resolution at the expense of photon flux, while conversely, K-B mirrors offer more flux but at the cost of resolution.

3.1.4 Synchrotron X-Ray Fluorescence Instrument Setup

Synchrotron radiation X-ray fluorescence (SXRF) microscopy was preformed at the 2-ID-E beamline of the Advance Photon Source located at the Argonne National Laboratory (ANL). This specific beamline is equipped with a number of essential components such as the undulator, double monochromator, Fresnel zone plate, and silicon drift detector (Figure 3.1). The undulator consists of periodic dipole magnets used to generate a static magnetic field at specific harmonics, forcing the electrons to undergo oscillations and radiate energy. The adjacent double monochromator then narrows the spectrum of radiation to a selected wavelength. Together, the undulator and double monochromator provide high brilliance X-rays with a tunable energy range between 8-20 keV. The sample is mounted on an aluminum stick and placed onto a rotational stage located inside a helium-filled chamber in order to reduce scatter signals from air. The Fresnel zone plate works to focus the high-energy X-ray beam to a submicron spot on the sample. The resulting emitted X-ray emission spectrum is then collected with an energy dispersive silicon drift detector. By raster scanning the specimen through the incident X-ray beam at a series of projection angles, quantitative elemental density maps can be generated. The raw data collected is then processed with MAPS[61] and MATLAB software packages.

Although the 2-ID-E beamline offers a resolution of 0.2 μm, the total acquisition time for a sample as large as a zebrafish embryo is approximately 25 hours for each projection. To circumvent this hindrance, decreasing resolution to 2 μm reduces total acquisition time to under 2 hours per projection. For the initial data set, 60 projections were collected over approximately 100 hours. A resolution of 0.2 μm would require more than 60 projections for proper reconstruction; however, 60 projections at 25 hours would take more than 60 days to complete. Therefore, larger biological samples are unable to utilize this high spatial resolution due to prohibitively long acquisition times. Acquisition

of the copper distribution in the original 24 hpf embryo was successful, but the increased size of the 48 hpf embryo proved challenging in obtaining similar distribution information at a reasonable resolution in a practical amount of time.

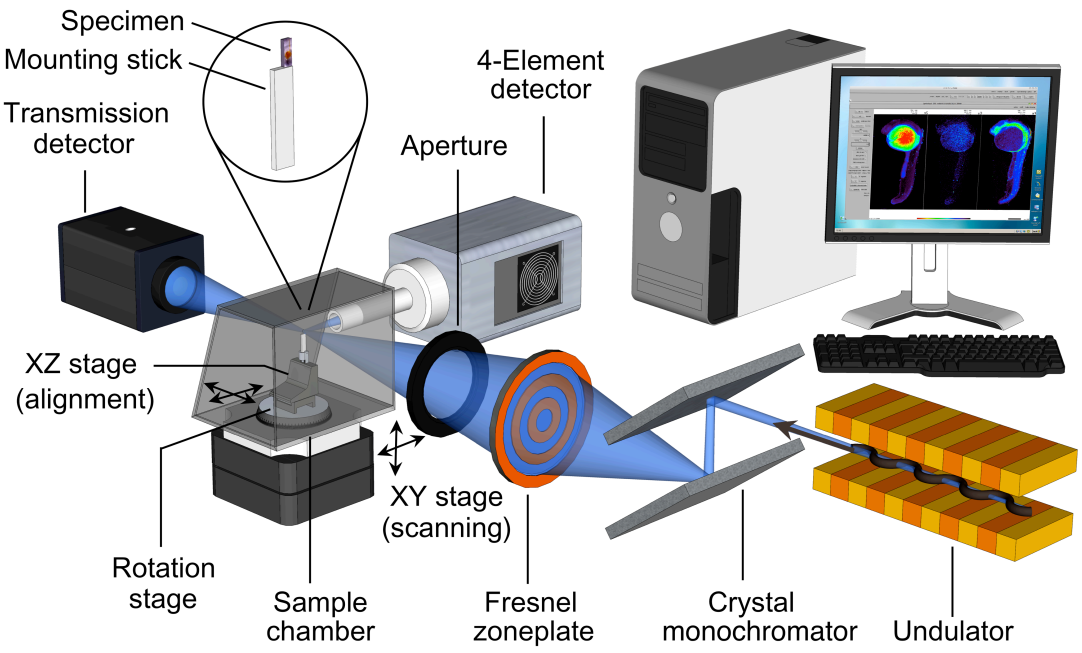

Figure 3.1: Schematic illustration of the X-ray fluorescence tomography instrument at the 2-ID-E beamline at the Advanced Photon Source (Argonne National Laboratory, USA). The embedded specimen was attached to an aluminum stick (circle inset) and mounted on the *xz*/rotation stage. As the stage rotates, the sample is raster-scanned through the focused beam for each projection angle. The emitted photons were subsequently captured by an energy-dispersive X-ray detector. Raw data was processed with MAPS[61] and MATLAB software packages.

To achieve the highest resolution possible at the 2-ID-E station would require inhibitive long data acquisition times. For this reason, the large embryo samples required 2-3 μm step sizes despite the beam focused to 300 nm, consequentially under-sampling the total elemental content. Using a larger sample such as a 72 hpf embryo would result in an even lower signal to noise ratio with higher data acquisition times.

3.2 Visualizing 3D Transition Metal Distribution in a Zebrafish Embryo

3.2.1 Specimen Preparation

Standard SXRF sample preparation often involves inherently thin samples, such as cells or thinly sliced tissue attached directly to a silicon nitride window. Preparations of this nature are not suitable for large samples such as zebrafish embryos and inhibit the ability to acquire projections over a full 180 degrees, thus, preventing the acquisition of truly three-dimensional data. Other methods of sample preparation include sealing the specimen in a liquid suspension in order to obtain projections over the full 180-360 degrees. Lengthy data acquisition times along with the essential micro-precision stability of the sample eliminate this technique due to the potential movement of the soft, flexible specimens such as a zebrafish embryo. In order to preserve its structure and position for long periods of time, the embryo must be embedded in a durable material. The composition of this material is important. This polymer must be resilient to high energy X-rays and contribute minimal fluorescence attenuation during the SXRF experiments. Attenuation of the signal from the resin can cause a misinterpretation of data by underestimating the metal content.

The sample preparation was performed in collaboration with Dr. Hong Yi from the Integrated Electron Microscopy Core at Emory University. Initially, high-pressure freezing was utilized in an attempt to preserve the zebrafish embryos at 24 hours post

fertilization (hpf) but led to fractures, likely due to insufficient cooling rates associated with specimens of this size. Alternatively, the dechorionated embryos were fixed first in paraformaldehyde solution followed by embedding using progressive lowering of temperature (PLT) methods.[62] Using PLT, samples were embedded in Lowicryl resin followed by UV polymerization from established protocols.

Further complications arise after embedding the sample in the Lowicryl resin. The polymer block must be cut down to reduce the amount of material between the X-rays and the actual zebrafish specimen. The block is so small it cannot be cut down by hand and any knife would leave trace metal behind interfering with the data analysis of the sample itself. The specimen must also be attached to an aluminum stick provided by the ANL that is required for mounting the sample on the rotational stage for data acquisition at the beamline.

To address this concern, the polymer embedded sample was shipped to Germany where it was cut down in size using a two-photon laser-based microtome system developed by Rowiak (TissueSurgeon, ROWIAK GmbH, Hannover, Germany). The sample was mounted on a microscope slide and trimmed using this femtosecond laser microtome for a close and contact free cut. As illustrated in Figure 3.2, the embedded embryo was excised using 4 lateral contact-free line sections (A) followed by a coplanar section on the ventral side that released the cube from the resin block (B). The extraneous resin was successfully removed at a distance of 60 μm away from the embryo while preserving the integrity of the embryo as shown by the near-infrared brightfield micrograph (C). Once excised from the larger polymer, the specimen was then mounted onto a thin aluminum arm with a drop of epoxy glue. This sample holder is then screwed into place on a kinematic stage at the 2-ID-E beamline of the Advanced Photon Source (Argonne National Lab, USA) allowing it to rotate to the required positions for acquiring SXRF data sets.

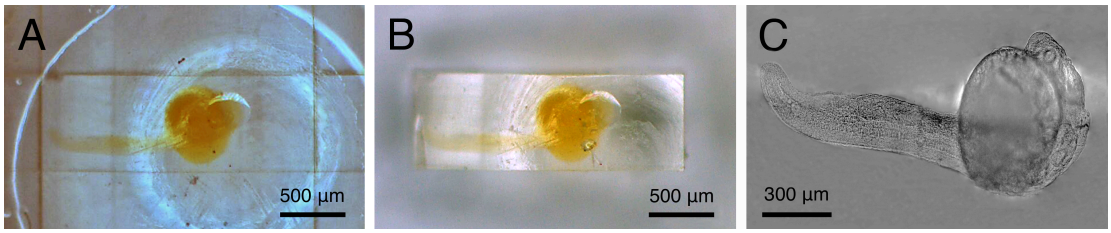

Figure 3.2: Preparation of resin embedded specimens for SXRF tomography using a femtosecond laser sectioning microtome system (TissueSurgeon, LLS Rowiak LaserLabSolutions, Germany). A zebrafish embryo at 24 hpf was fixed and embedded in resin (Lowicryl K4M) by the progressive lowering of temperature method (PLT). The cured resin block was mounted on a microscope slide and trimmed by 4 contact-free lateral line sections **A** followed by a coplanar section on the ventral side of the embryo **B**. The near-infrared (800 nm) brightfield image **C** confirmed the integrity of the specimen.

3.2.2 Data Acquisition

The completed SXRF tomographic data set of the zebrafish embryo 24 hpf was composed of 60 projections spread over an angular space of 180°. The data were collected in two batches with a 3 degree offset and 6 degree intervals. The sample itself is rotated to each position where a sinogram is then acquired. For each orientation, the specimen was translated horizontally through the stationary beam with excitation at 10 keV and a step size of 2 µm, which required over 100 hours for the collection of approximately 20 million individual emission spectra.

Gaussian fitting of the raw emission spectra data for each image pixel was processed through the MAPS software package to generate elemental maps within the zebrafish embryo. Matching X-ray emission lines to Gaussian peaks, the fluorescence signals for each element could be charted. Because the cross section of the resin block varies as a function of the acquisition angle, the integrated fluorescence intensity was non-uniform across the projection series. To correct for the attenuation differences, each projection was normalized to the maximum integrated emission intensity. The resulting

elemental distributions were calibrated to elemental area densities (μg cm^{-2}) by comparing sample signal strength of X-ray fluorescence to those of thin film standards SRM 1832 and 1833 of the National Bureau of Standards (NBS/NIST, Gaithersburg). Based on this procedure, a total zinc content of 7.1 ng was determined, which is in agreement with the average zinc content of ~7.3 ng at 24 hpf reported in the literature.[63]

3.2.3 Tomographic Reconstruction

The SXRF microtomography data collected could, in theory, be processed with the same algorithms developed for absorption-based X-ray computed tomography (X-ray CT). A common approach for the three-dimensional reconstruction of X-ray CT data is the filtered back projection (FBP) algorithm. A derivation of the philosophy behind pencil-beam reconstruction, beams are emitted in a cylindrical arrangement to create differences in grey values in pixels crossed by the beam. FBP produces blurred trans-axial images, where filtering and varying interpolation techniques render higher resolution projections that are used for reconstruction.[64]

As illustrated in Figure 3.3, this method is not well suited for reconstruction of fluorescence-based projections, often producing artifacts in the reconstructed images. The Iterative Maximum Likelihood Expectation Maximization (MLEM) algorithm was found to be most suitable for the reconstruction of the SXRF data to reduce artifacts and noise. This method derives a correction function from a sinogram and guessed model, then uses the function again and adjusts to a better guess. The process is repeated several times, each time trying to correct the model and find the best guess.

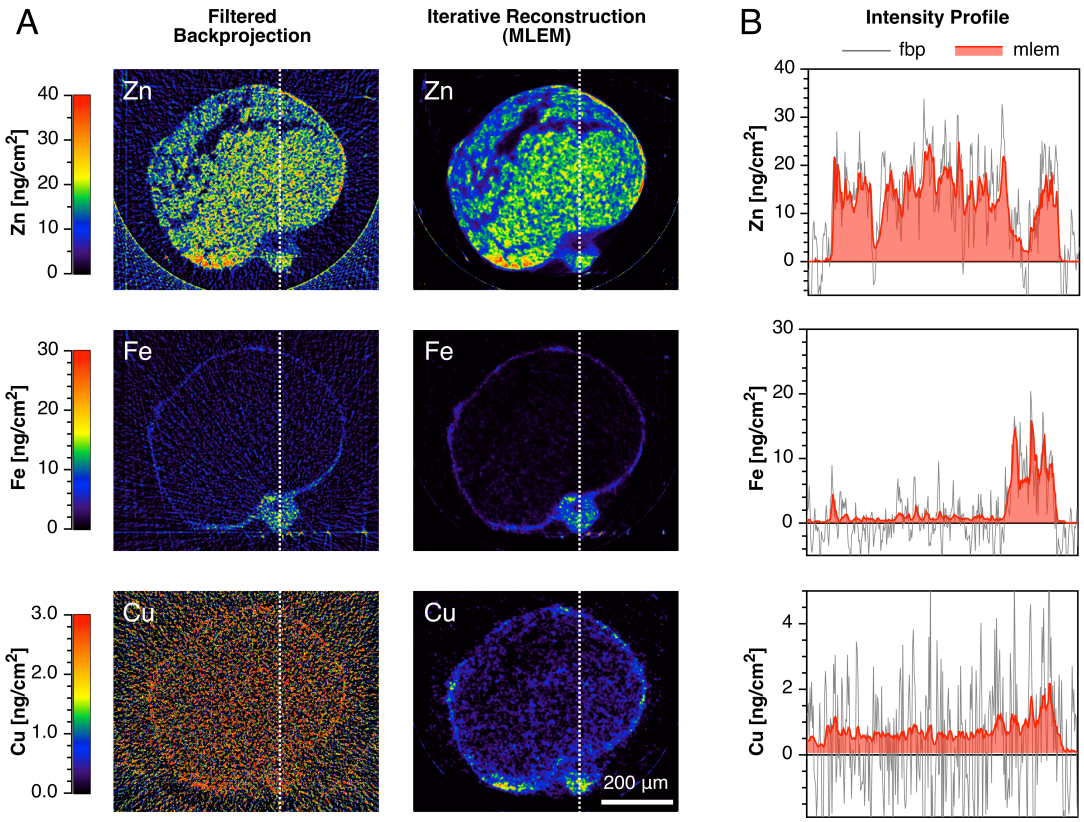

Figure 3.3: Tomographic reconstruction of the elemental densities of zinc, iron and copper in the zebrafish embryo 24 hpf. Reconstructions based on the corresponding SXRF emission projection data sets. **A**. Comparison of the reprojected elemental densities based on a filtered back projection algorithm with Ramachandran–Lakshminarayanan (‘‘Ram–Lak’’) ramp-filter and an iterative maximum likelihood expectation maximization (MLEM) algorithm. The MLEM algorithm leads to significantly improved reconstructions in the case of noisy datasets. **B**. Intensity profile of the reconstructed density images shown in (A) along the white dashed line. The fluorescence detector was positioned on the left side relative to the reconstructed images of panel (A).

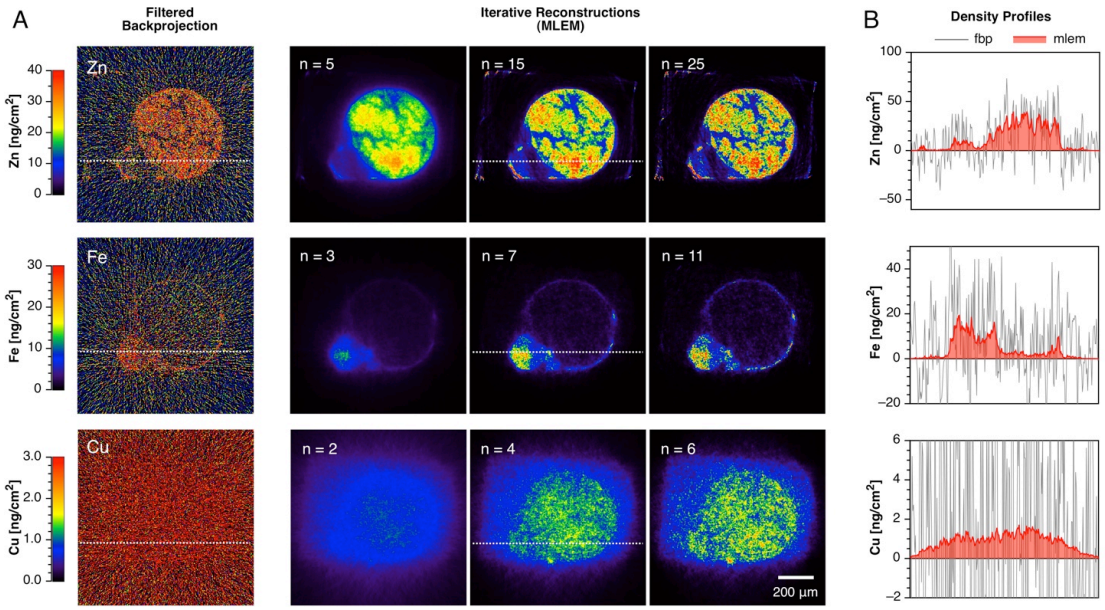

Figure 3.4: Tomographic reconstruction of the elemental densities of zinc, iron and copper in the zebrafish embryo 48 hpf. Reconstruction is based on a single-line sinogram using the iterative maximum likelihood expectation maximization (MLEM) algorithm. **A**. Comparison of the reprojected elemental densities based on a filtered back projection algorithm with Ram–Lak ramp-filter and the MLEM algorithm. The latter leads to significantly improved reconstructions for noisy datasets. **B.** Density profiles of the reconstructed images shown in (A) along the white dashed line. The fluorescence detector was positioned on the left side relative to the reconstructed images of panel (A).

In addition to being less sensitive towards projection noise compared to FBP, the MLEM algorithm has the advantage to yield back projections with only positive densities as illustrated with the profiles in Figure 3.4. As the MLEM algorithm approaches convergence with increasing iteration numbers, there is also a concomitant increase of the noise amplitude. Conversely, the noise level is reduced at lower iteration values but at the expense of image resolution. For this reason, the optimal iteration number differs depending on the noise level of the raw sinogram and must be determined empirically. Based on this approach, a compromise between sharpness and noise level was determined and the zinc, iron and copper distributions were reconstructed for the 24 hpf

embryo using 70, 30 and 15 iterations respectively and iteration values of 15 for zinc and 7 for iron were used for the 48 hpf embryo.

As the total amount of copper in most organisms is lower, by approximately one order of magnitude, than zinc and iron, it is not surprising that the signal-to-noise ratio of the copper Kα emission sinogram is much lower compared to the iron and zinc data. Concluding from the MLEM reconstructions of the 48 hpf embryo shown in Figure 3.4, the number of photons collected within the copper Kα spectral region was insufficient to arrive at meaningful elemental densities, regardless of the number of iterations. By comparison, FBP of the same set of sinograms resulted in reconstructed densities with much higher noise amplitudes, to the extent that the noise partially or completely obscured the elemental density distributions in the reconstructed images.

3.2.4 Attenuation Correction

The collected photon counts from the acquired raw data must be compared to relative standards and converted to elemental content. The Lowicryl resin used for embedding the specimen results in attenuation of both the excitation and fluorescence emission intensities in an energy-dependent manner, altering the data interpretation of the converted elemental content. To compensate for the loss of photons due to matrix absorption, element specific linear scaling factors were applied to the raw projections. According to the Beer-Lambert law (1), the intensity *I* of the X-ray beam is attenuated as a function of the pathlength *l* in an exponential fashion with

$$I = I_0 \cdot e^{-l\mu} \quad (1)$$

where I_0 corresponds to the incident beam intensity, and μ is the energy-dependent linear attenuation coefficient of the specimen and embedding material. As the sample rotates, the angular position of the specimen relative to the incident beam and emission detector changes. The attenuation of the excitation and emission intensities for a given volume element will vary for each tomographic projection. In a cylindrical sample, the attenuation of photons emitted at the axis of rotation remains constant regardless of angular position. Emission intensity *I* at the detector is given by the geometric mean according to equation (2)

$$I = I_0 \cdot e^{-\frac{l}{2}(\mu_{ex}+\mu_{em})} \quad (2)$$

where μ_{ex} and μ_{em} are the linear attenuation coefficients for the material at the respective excitation and emission energies. These coefficients together represent the total attenuation. Half of the pathlength *l*/2 represents the center point of rotation. To compensate for the attenuation of photons at *l*/2, a linear scaling factor *f* is applied according to equation (3)

$$f = e^{\frac{l}{2}(\mu_{ex}+\mu_{em})} \quad (3)$$

Linear attenuation correction is only a useful approximation if the sample is uniform in shape, characterized by short pathlengths and small attenuation coefficients at the emission energies of the elements of interest. According to previous attenuation simulations, using a phantom embedded within polymethyl methacrylate (PMMA) with square-shaped cross section, the attenuation corrected elemental concentrations should

be accurate within an error margin of 20% or better for zinc, copper, and iron for this size of specimen. [65]

To estimate the linear attenuation coefficient μ_{ex} of the Lowicryl resin for the excitation beam at 10 keV, the difference in photon flux before and after passing through the sample was measured. As illustrated with Figure 3.5, the intensity drops by approximately 20% if the resin block is positioned at a 0° or 180° angle relative to the incoming beam, and by approximately 30% at a 90° angle. From the attenuation profiles shown in Figure 3.5B, the corresponding pathlength *l* of the cuboid-shaped resin block and the average attenuated intensities for each of the three angular orientations can be determined. On the basis of these, Beer-Lambert's law (1) may be applied and the average attenuation coefficient μ_{ex} (10 keV) for Lowicryl was determined to be 3.96 ± 0.04 cm^{-1}, a value that is in good agreement with previous measurements.

The attenuation coefficients for the element specific Kα emissions of zinc, copper, and iron were obtained from simulations with the software WinXCOM assuming PMMA as matrix material with a density of 1.18 g/cm^3 to yield the values $\mu_{ZnK\alpha}$ = 6.09 cm^{-1}, $\mu_{CuK\alpha}$ = 7.52 cm^{-1}, and $\mu_{FeK\alpha}$ = 15.00 cm^{-1}, respectively. Figure 3.6 illustrates the energy-dependent attenuation of the excitation beam and the Kα emissions of zinc, copper, and iron as a function of the pathlength through the matrix based on the estimated attenuation coefficients. The corresponding attenuation length, defined as the depth into a material where the X-ray intensity falls to 1/e of the initial value (37%), decreases from 2.5 mm for the incident beam to 0.67 mm for the Kα emission of iron. Altogether, these data demonstrate that Lowicryl is well suited as an X-ray compatible matrix material for imaging the biologically relevant first-row transition elements in specimens of up to approximately 1 mm of thickness.

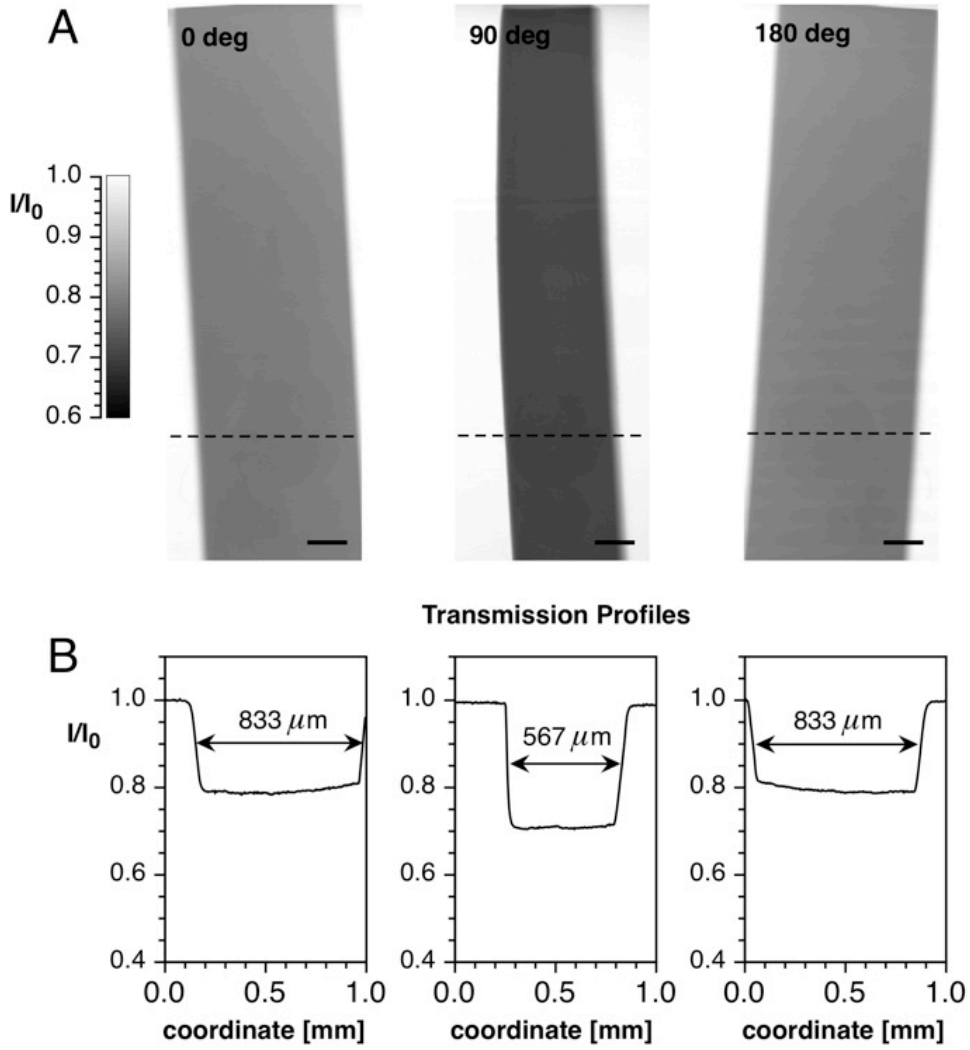

Figure 3.5: Attenuation of the incident X-ray beam (10 keV) by the Lowicryl resin matrix. **A.** Absorption contrast images of the resin block at 0°, 90°, and 180° orientations relative to the incident beam. Scale bar: 200 µm. **B.** Transmission profiles across the image coordinate marked with a dashed line in panel (A). Note that compared to the matrix, absorption by the zebrafish embryo is negligible.

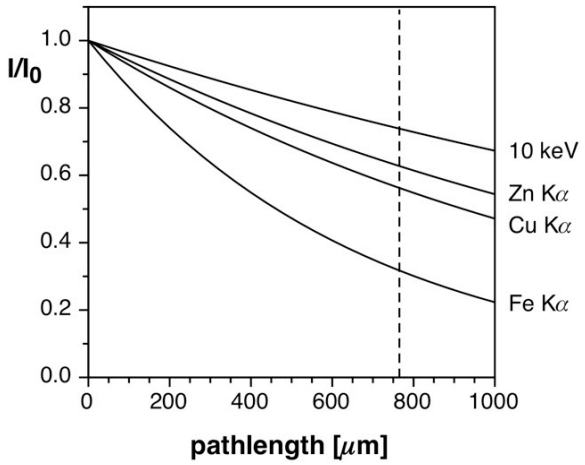

Figure 3.6: Energy-dependent attenuation of photons passing through a PMMA matrix as a function of pathlength. Calculated according to equation (1). The following attenuation coefficients were used for the plot: μ_{10keV} = 3.96 cm^{-1}, $\mu_{ZnK\alpha}$ = 6.09 cm^{-1}, $\mu_{CuK\alpha}$ = 7.52 cm^{-1}, and $\mu_{FeK\alpha}$ = 15.00 cm^{-1}. The dashed line indicates the average pathlength of the resin matrix (l = 740 µm).

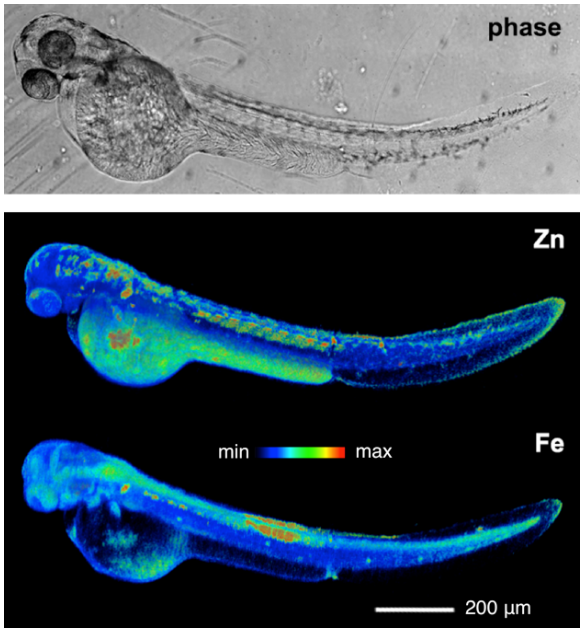

Figure 3.7: Zinc and iron distribution within the zebrafish embryo at 48 hpf. Reconstructed on the basis of 60 tomographic projections using an iterative maximum likelihood expectation maximization (MLEM) algorithm. The false-color calibration bar reflects a dynamic range from 0 - 2 mM for Zn and 0 - 1 mM for Fe. For comparison, the phase image (top) shows the resin-embedded embryo along the same projection axis.

3.3 Volumetric Transition Metal Reconstructions

Using the optimal number of iterations, the MLEM algorithm was applied to each of the 815 line-sinograms to generate complete 3D elemental distributions for zinc and iron for the 48 hpf embryo (Figure 3.7). To arrive at actual elemental concentrations, the raw photon counts were compared with the emission intensity of a thin film standard containing known amounts of zinc, copper, and iron. Corresponding linear scaling factors were applied as described in the previous paragraph to compensate for signal attenuation by the Lowicryl resin. Based on the calibrated volumetric data, which entail over 63 million voxels with the dimension 3.5 x 3.5 x 3.5 μm^3, a total zinc content of ~8.2 ng was determined. This value is in good agreement with the average zinc content reported in the literature for an embryo at this stage of development.[63]

In order to assess the quality of the reconstructed volumetric data sets, projections of the zinc and iron densities at an angle of 0 degree relative to the incident beam were calculated (Figure 3.8 and Figure 3.9). A comparison with the raw data acquired at the same projection angle revealed an overall small error for the difference image. As illustrated by the intensity profile shown in Figure 3.8B and Figure 3.9B, the error was dominated by the increased noise-amplitude of the unprocessed data rather than a systematic deviation due to reconstruction artifacts.

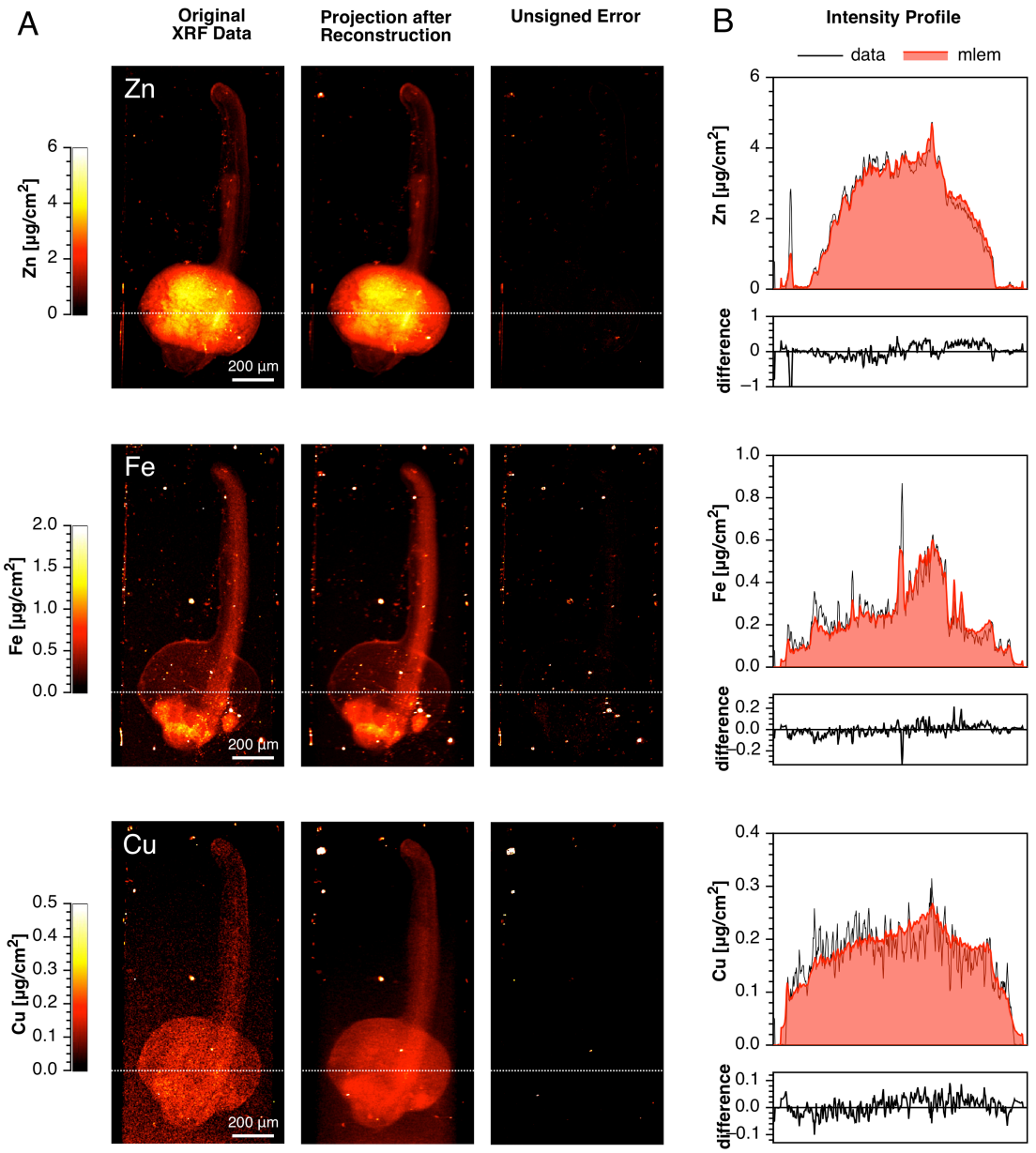

Figure 3.8: Comparison of the experimental and reconstructed elemental densities at a projection angle of 0 degree in the 24 hpf embryo. **A:** The volumetric distribution of each element was reconstructed using the iterative maximum likelihood expectation maximization (MLEM) algorithm, and the reconstructed data were projected at the same angle as the measured data (2nd column). The 3rd column illustrates the unsigned error in the form of difference images. The panels for each element are based on different density scales as indicated by the calibration bars on the left. **B:** Intensity profiles of the experimental (black) and reconstructed data (red) across the dashed line indicated in the projection images. The graph below each profile illustrates the signed difference between the experimental and reconstructed profiles.

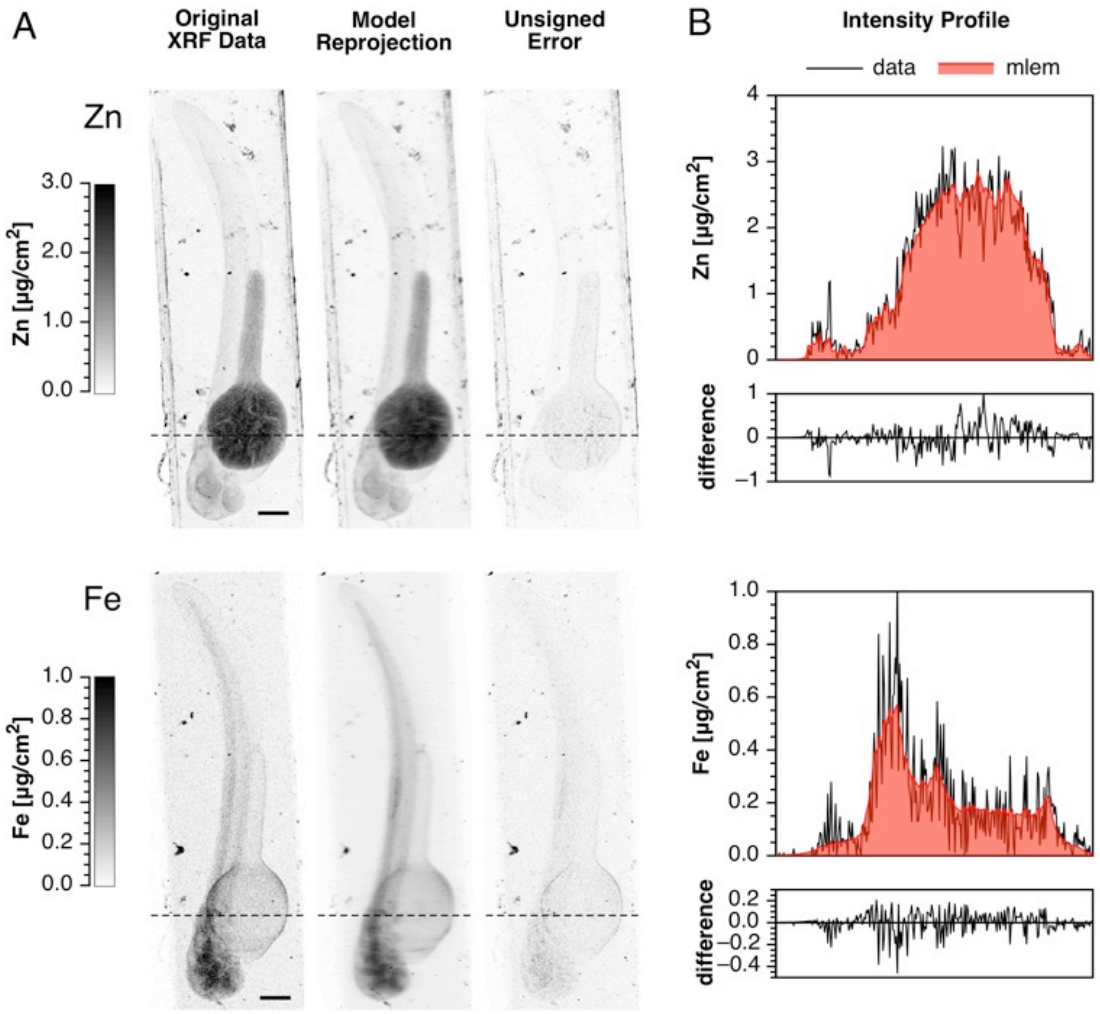

Figure 3.9: Comparison of the experimental and reconstructed elemental densities at a projection angle of 0 degree in the 48 hpf embryo. **A:** The volumetric distribution of each element was reconstructed using the iterative maximum likelihood expectation maximization (MLEM) algorithm, and the reconstructed data were projected at the same angle as the measured data (2nd column). The 3rd column illustrates the unsigned error in the form of difference images. The panels for each element are based on different density scales as indicated by the calibration bars on the left. **B:** Intensity profiles of the experimental (black) and reconstructed data (red) across the dashed line indicated in the projection images. The graph below each profile illustrates the signed difference between the experimental and reconstructed profiles.

3.3.1 Pharyngula Period, 24 Hours Post Fertilization

At 24 hpf, the embryo has just transitioned out of segmentation and into the pharyngula period, which is characterized by a well-developed notochord, elongated tail and a brain sculpted into distinguishable lobes and ventricles.[66] To illustrate the most pertinent aspects of the zinc, iron, and copper distributions, Figure 3.10 shows a series of virtual sagittal, coronal and transverse sections of the embryo. The position of each slice is depicted in column A in the form of a 3D rendering, and the corresponding 2D elemental maps are illustrated in column B. To accommodate the differences in dynamic range between the elements, the false-color maps are reproduced with different concentration scales. Furthermore, column C features normalized dual-color overlays to visualize the relative spatial relationships between pairs of elements.

Among the three metals, zinc is the most abundant with concentrations approaching 7 mM (Figure 3.10B). The most significant pool, comprising more than 80% of the total zinc content, is found in the yolk (yo) and yolk extension (ye) (Figure 3.10, 1st and 2nd row). The early pharyngula period is also marked by the formation of the circulatory system, and the presence blood vessels (bv) can be recognized as voids within the zinc distribution of the yolk. These blood vessels, such as the common cardinal veins or ducts of Cuvier, carry blood ventrally across the yolk to supply blood to the heart.[67] The zinc distribution can be further correlated with structures of the nervous system such as the notochord (nc), the neural tube (nt), and the brain. Similar to the blood vessels, the notochord region is marked by a low metal content, whereas the neural tube is set apart by areas of high zinc (Figure 3.10B, 1st row, transverse section). The ventricles of the brain appear as voids within the zinc maps; specifically, the third (tv) and fourth (fv) ventricles can be identified in the sagittal section (Figure 3.10B, 1st row). While the ventricles uniformly exhibit low trace metal levels, various regions of the grey matter can be identified, including the mesencephalon (mc), cerebellum (cb), the

telencephalon (tc) and diencephalon (dc) of the forebrain, and the rhombencephalon (rc) of the hindbrain. Finally, the sagittal section (Figure 3.10, 3rd row) reveals a distinct accumulation of zinc at the tip of the tail (tl), mostly localized to peripheral cell layers. Altogether, this area exhibits the highest concentration of zinc within the embryo.

By comparison, the iron distribution appears less localized with maximum concentrations not exceeding 2 mM. As evident from the overlays in Figure 3.10C (1st column), iron and zinc are distributed in an anti-correlated fashion throughout most regions of the embryo. A detailed analysis revealed two distinct populations of voxels with anti-correlated zinc and iron contents as well as a low Pearson's correlation coefficient of 0.117 (Figure 3.11). The highest concentration of iron can be found in the medial region of the tail as well as in areas of the brain, whereas the yolk and yolk extension are characterized by overall low iron levels. Instead, both structures are surrounded by a thin iron veneer, which does not overlap with regions of high zinc. Similarly, the areas of high zinc at the tip of the tail are low in iron and set apart from the iron-rich regions in the medial body. Although zinc and iron are anti-correlated throughout most of the embryo, there are still a few notable similarities. For example, the notochord appears to be void of iron, whereas the neighboring neural tube contains much higher concentrations. Similar to zinc, the anatomical features of the brain can be readily recognized based on the iron distribution.

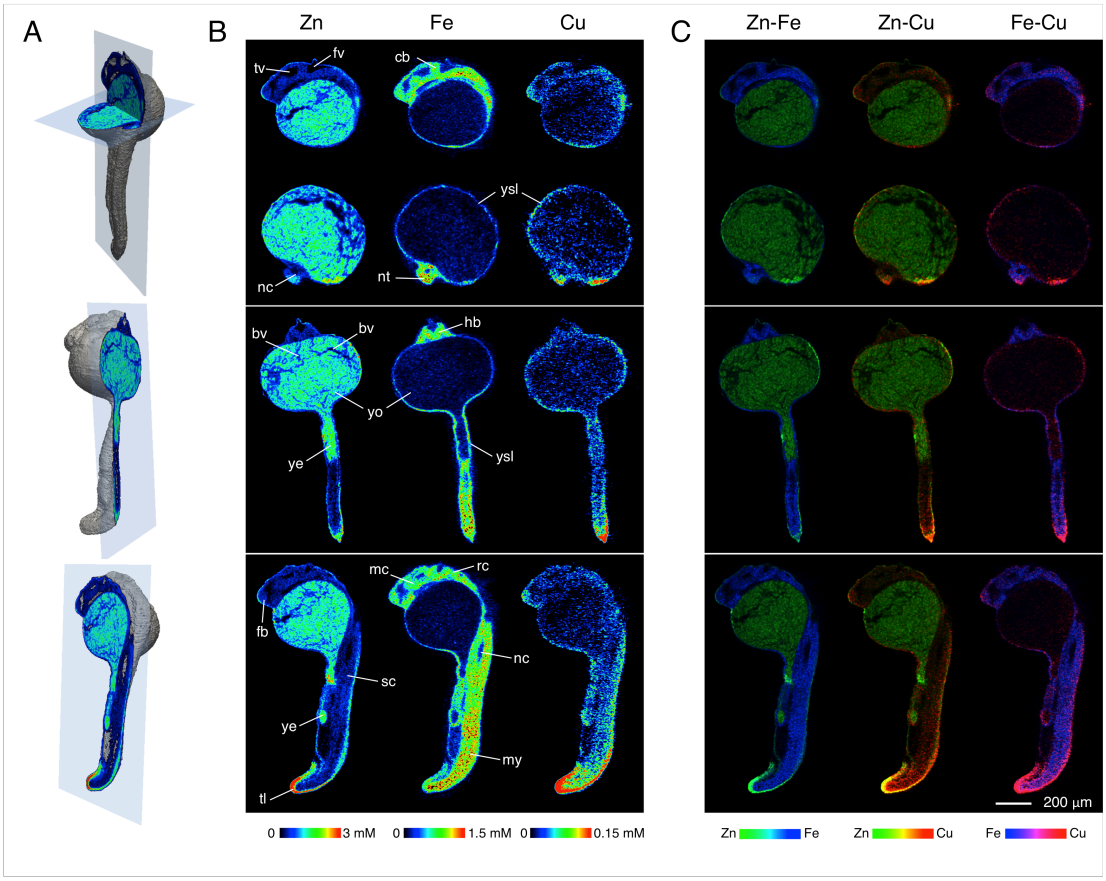

Figure 3.10: Visualization of elemental distribution in a zebrafish embryo (24hpf) by X-ray fluorescence tomography. Reconstructed using MLEM algorithm. **A.** 3D-rendering of the embryo indicating the spatial orientation of the virtual slices that are displayed in panels B and C. Slices include a sagittal and transverse section (top), coronal section (middle), and a second sagittal section offset to the left (bottom). **B.** Elemental distributions of Zn, Fe, and Cu for each of the 4 slices. Individual concentration scales for each element are displayed at the bottom of each column. Abbreviations: third ventricle (tv), fourth ventricle (fv), cerebellum (cb), notochord (nc), neural tube (nt), yolk syncytial layer (ysl), blood vessels (bv) hindbrain (hb), yolk (yo), yolk extension (ye), myosine (my), telencephalon (tc), mesencephalon (mc), diencephalon (dc), rhombencephalon (rc), spinal chord (sc) and tail (tl). **C.** False color overlays of the elemental distributions of Zn, Fe, and Cu indicating regions of spatial correlation. The concentration scales of each element were normalized and color-coded as follows: Zn (green), Fe (blue), and Cu (red). Areas of spatial correlation appear in the corresponding mixed hues.

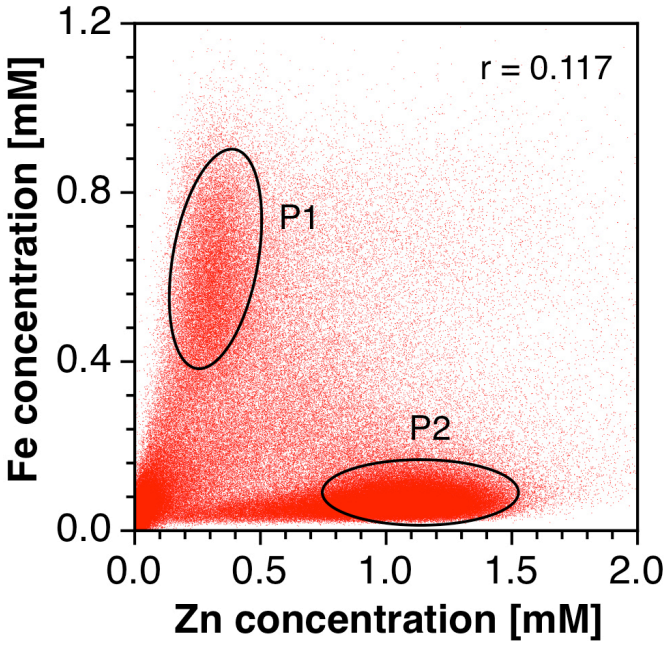

Figure 3.11: Scatter plot illustrating the correlation between the Zn and Fe distribution in a zebrafish embryo at 24 hpf. Each pixel indicates the elemental concentration of a voxel in the reconstructed data set. Due to the large size of the original data set, the voxels were binned by a factor of 64 to yield a total of 1.95 million pixels. The Pearson's correlation coefficient r was calculated based on the binned data set.

Given the low concentration of copper throughout the embryo, the reconstructed data set is of lower quality and characterized by a significant level of background noise. Nevertheless, the 3D model revealed distinct regions that could be correlated with the zinc and iron distributions. Most notable is the high concentration of copper located at the tip of the tail also observed for zinc. The high degree of spatial correlation between the two metals is apparent in the overlay plot as orange-yellow regions (Figure 3.10C, 3rd row). Similar to iron, the copper concentration within the yolk and yolk extension is low, but appears increased within a peripheral layer surrounding both structures.

3.3.2 Hatching Period, 48 Hours Post Fertilization

The reconstructed volumetric data shown in Figure 3.7 reveal distinct differences in the zinc and iron distributions, most notably regions of elevated concentrations appear mutually exclusive. While the highest levels of zinc are found in the yolk and yolk extension, the iron concentration in both regions remains low. Conversely, areas with increased iron levels, including the myotome extending along the dorsal side or various regions of the brain, are consistently low in zinc. To provide a more detailed picture of the elemental localizations and how these regions relate to specific anatomical features, Figure 3.12 and Figure 3.13 reveal a series of virtual sagittal, coronal and transverse sections of the embryo. The 3D renderings in column A represent isodensity surfaces of zinc to illustrate the position of each section corresponding to the 2D elemental maps arranged in column B.

The yolk (yo) and yolk extension (ye) constitute approximately 83% of the total zinc content in the embryo at this stage of development. High levels of zinc, which range between 0.5 and 1.5 mM, are evident in both the sagittal and coronal sections depicted in Figure 3.12. The blood vessels throughout the yolk appear as voids. In contrast, the yolk syncytial layer (ysl) exhibits a higher concentration of iron, likely due to enhanced expression of the iron transporters ferroportin1 and transferrin in the YSL.[68,69] A blue-green false color overlay indicates strong anti-correlation between the iron (blue) and zinc (green) levels throughout this region of the embryo (Figure 3.12C), an observation that is similar to the elemental distribution found at 24 hpf.[65] Anterior to the yolk sac, the pericardial cavity (pc) is notably void of both zinc and iron. This cavity contains the heart and is filled with pericardial fluid, composed primarily of lactate dehydrogenase and other non-metalloproteins.[70] Additionally, transverse sectioning of the elemental reconstructions in Figure 3.13 reveals the single atrium (at) of the heart located inside the pericardial cavity. Based on the overlay image of both zinc and iron,

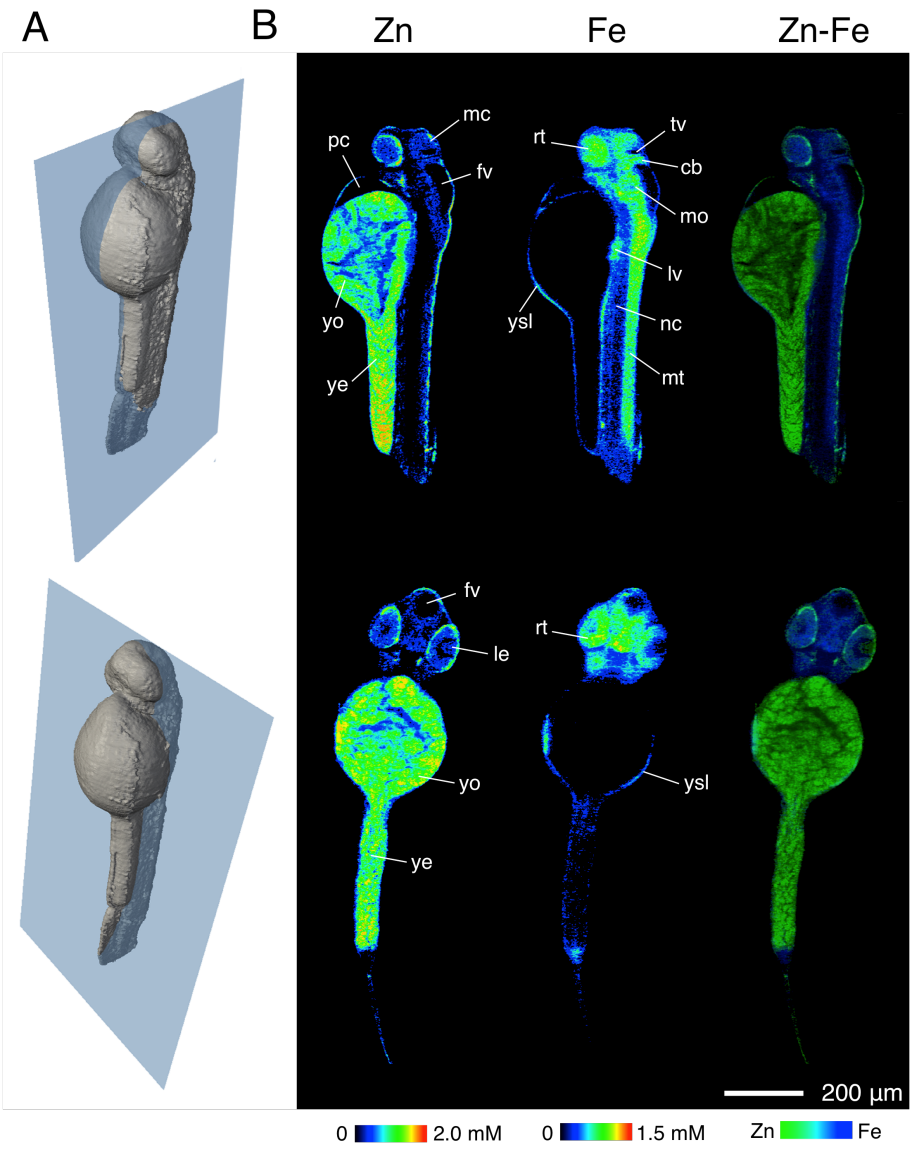

Figure 3.12: Visualization of elemental distribution in a zebrafish embryo (48 hpf) by X-ray fluorescence tomography. Reconstructed using MLEM algorithm. **A**. 3D-rendering of the embryo indicating the spatial orientation of the virtual slices that are displayed in panel **B.** Slices include a sagittal section (top) and a coronal section (bottom). B. Elemental distributions of Zn and Fe for each of the 2 slices. Individual concentration scales for each element are displayed at the bottom of each column. Abbreviations: Mesencephalon (mc), retina (rt), third ventricle (tv), cerebellum (cb), fourth ventricle (fv), pericardial cavity (pc), yolk (yo), yolk extension (ye), yolk syncytial layer (ysl), medulla oblongata (mo), liver (lv), notochord (nc), myotome (mt), and lens (le). The third column contains false color overlays of the elemental distributions of Zn and Fe indicating regions of spatial correlation. The concentration scales of each element were normalized and color-coded as Zn (green) and Fe (blue). Areas of spatial correlation appear in the corresponding mixed hue.

the atrium is rich in zinc. Moreover, the liver (lv) appears as a prominent, iron rich anatomical feature of the 48 hpf embryo. At this stage of embryogenesis, liver morphogenesis is well underway and is characterized by visible liver rudiments, continued budding, and the early formation of the hepatic duct.[71] As a major storage site of ferritin, the primary protein responsible for intracellular iron storage and release, this organ is readily identified in the iron distribution map. In contrast, at 24 hpf the zebrafish liver is described as only a flat endoderm in the pharyngeal region and cannot be readily recognized within the elemental distributions previously reported for this stage of development.[65]

The development of the lens (le) and the retina (rt) give rise to distinct differences in the 24 hpf and 48 hpf elemental maps of the embryo. At 48 hpf, the lens has detached from the overlying ectoderm and developed into a large spherical structure separate from the retina.[72] These structures are easily distinguished in the reconstructions due to the elevated concentrations of zinc and iron. Notably, the zinc distribution map indicates a higher level of zinc in the outer layers of the retina with concentrations ranging between 1 and 1.5 mM. SXRF microscopy studies on 3 μm thick eye sections from a zebrafish 5 days post fertilization (dpf) also indicated increased zinc concentrations in the retinal pigment epithelium.[53] Additionally, SXRF microscopy studies on 30 μm-thick freeze-dried cryosections of rat retina revealed a similar distribution with increased zinc concentrations in the retinal pigment epithelium as well as the photoreceptor inner segment and outer limiting membrane.[73] Although these studies also indicated increased levels of iron in the outer layers, the results show a more uniform distribution throughout this region. The critical role of zinc and iron in the normal function of the lens and retina is well established.[73-77] For example, high concentrations of histochemically reactive zinc have been identified in the mouse and rat retina, with the highest levels localized to the retinal pigment epithelium and the inner segment of the photo receptors.[78-80] These

areas also coincide with increased expressions of the zinc transporters ZnT-3 and ZnT-7,[78,81] thus underscoring the importance of retinal zinc homeostasis, not only for the metalation of Zn-dependent proteins critical to vision,[82,83] but likely also for supporting the role of zinc as a neuromodulator.[84] Similarly, high levels of iron in the retinal epithelium are consistent with the presence of several Fe-dependent enzymes critical for cellular function, most notably RPE, an iron-dependent microsomal enzyme responsible for converting trans-retinyl ester to 11-cis retinol during the visual cycle.[77]

Dorsal to the lens and retina, high concentrations of both zinc and iron define the grey and white matter of the brain, a region that contrasts the low trace metal concentrations found in ventricles. The medulla oblongata (mo), hypothalamus (hy), myelencephalon (my), and mesencephalon (mc) including the cerebellum (cb) as well as the third (tv) and fourth ventricle (fv) can all be distinguished in both elemental maps. Similar to studies performed on human brain tissue,[85,86] the concentrations of zinc and iron show variability as they are heterogeneously distributed throughout different regions of the brain. As a major metal repository and one of the brain structures richest in iron and zinc[85-87] it is not surprising that the cerebellum stands out in both sagittal and transverse sections of the elemental maps. Additionally, intracellular concentrations of zinc and iron are critical for the normal function of the brain,[11,88,89] and are tightly regulated by a number of importers, exporters, and storage proteins. For example, the iron regulatory proteins ferritin and transferrin are found in the grey and white matter of the brain.[88,90] Although iron uptake into the brain remains essential throughout life, it peaks during embryogenesis characterized by rapid growth and development of this organ.[91] Additionally zinc-finger-containing gene *fezl* is expressed in the forebrain during zebrafish embryogenesis and is required to define the developing regions of the telencephalon, diencephalon and hypothalamus[92-94] and Early growth response 1 (Egr1) is strongly expressed at 48 hpf in the forebrain and midbrain, specifically diencephalon,

hypothalamus, and the myelencephalon.[95] This essential growth protein has a highly conserved structure that contains three zinc-finger sequences.[96,97] Egr1 is also expressed in the heart at this stage of embryogenesis[95] which may contribute to the zinc observed in the atrium of the 3D reconstructions.

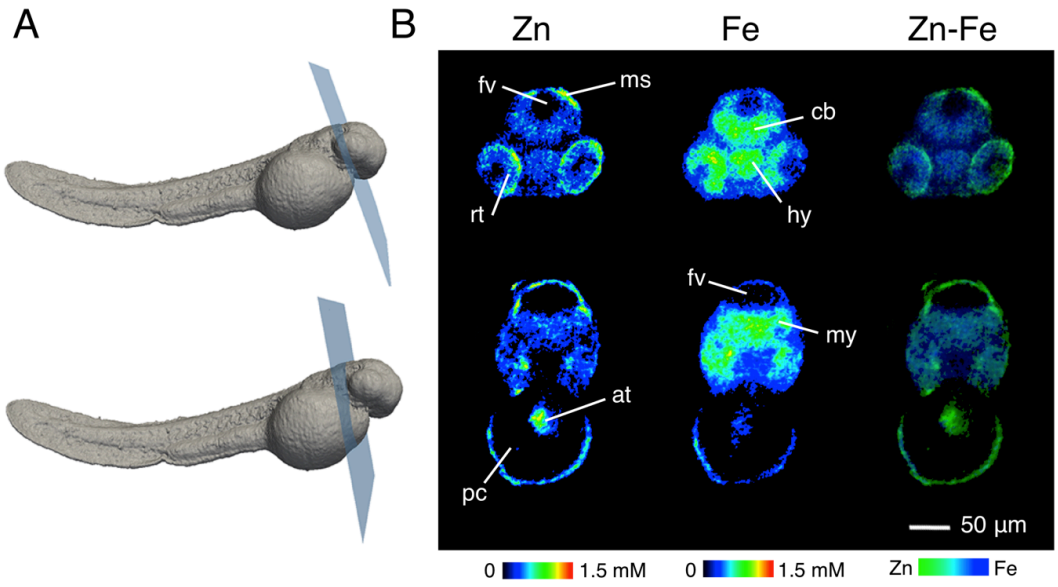

Figure 3.13: Visualization of elemental distribution in a zebrafish embryo (48 hpf) by X-ray fluorescence tomography using MLEM reconstruction. **A.** 3D-rendering of the embryo indicating the spatial orientation of the two virtual transverse slices that are displayed in panel B. Elemental distributions of Zn and Fe for each of the 2 slices. Individual concentration scales for each element are displayed at the bottom of each column. Abbreviations: Fourth ventricle (fv), mesencephalon (ms), retina (rt), cerebellum (cb), hypothalamus (hy), pericardial cavity (pc), atrium (at), and myelencephalon (my). The third column contains false-color overlays of the elemental distributions of Zn and Fe indicating regions of spatial correlation. The concentration scales of each element were normalized and color-coded as Zn (green) and Fe (blue). Areas of spatial correlation appear in the corresponding mixed hue.

Lastly, the posterior body of the embryo is largely defined by the tail and notochord (nc). The notably low metal content in the notochord is an intriguing observation for a structure often characterized as an essential organ in development.[98,99] This finding parallels the low trace metal concentration found in the elemental reconstructions of the embryo at 24 hpf.[65] In contrast to the notochord, the mytome (mt) of the tail appears to be iron rich and a distinct accumulation of zinc is found at the tip of the tail. Both features are in agreement with the previously reported elemental distributions of the 24 hpf embryo.[65]

3.4 Conclusions

The importance of zinc for cellular proliferation and growth is well established.[7] As the maternally derived yolk stores are the primary source of nutrients for the embryo, this pool supplies all developing tissues and organs with zinc, likely orchestrated through an elaborate network of zinc transporters.[63] For example, the reduced expression of ZIP7, a zinc importer of the SLC39 solute carrier family of proteins, led to markedly decreased zinc levels in the eye at 72 hpf whereas the total zinc content of the embryo remained unaltered.[100] In contrast, both iron and copper are more concentrated in the yolk syncytial layer (ysl) surrounding the yolk and yolk extension. This extra-embryonic tissue serves critical functions in cell fate specification, morphogenesis, and nutrient transport.[101] The iron transporters ferroportin1 and transferrin are specifically expressed in the YSL,[68,69] underscoring its role in iron mobilization. Likewise, ceruloplasmin, the major Cu-carrying protein that also assists in iron transport,[102] is localized to the YSL at this stage of development.[103] Furthermore, at 24 hpf, pigment formation is initiated by melanophores, which depend on copper to supply the enzyme tyrosinase involved in melanogenesis.[104,105] The melanophores start to develop dorsolaterally throughout the body of the tail, an area that is also characterized by increased levels of copper. Finally,

the markedly increased levels of zinc and copper at the posterior end of the embryo coincide with areas of progenitor cell differentiation[106] and cellular proliferation,[107] which are responsible for most of the body growth during the pharyngula period.[99]

This study demonstrates that X-ray fluorescence tomography has matured into a powerful technique for the high-resolution 3D visualization of transition metals, even for large specimens such as a zebrafish embryo. The reconstructed elemental densities provided intriguing insights into the 3D distribution of zinc, copper, and iron at these two stages of embryonic development and revealed distinct areas of localizations that could be correlated with characteristic anatomical features. Furthermore, a total zinc content of 7.1 ng and 8.2 ng were calculated based on the data collected for the zebrafish embryos at 24 hpf and 48 hpf, respectively. These values are in good agreement with the average zinc content of ~7.3 ng at 24 hpf reported in the literature.[63] Additionally, the preparation technique, which combines the progressive lowering of temperature method with femtosecond laser sectioning, should be applicable to a wide range of soft tissue specimens.

3.5 Materials and Methods

3.5.1 Sample Preparation

Adult wild-type zebrafish were housed and mated under standard laboratory conditions. Fertilized embryos were harvested and kept in E3 medium (5 mM NaCl, 0.17 mM KCl, 0.4 mM $CaCl_2$ and 0.16 mM $MgSO_4$) at 28.5°C. At 24 hpf, embryos were anesthetized using 0.02% Tricaine, manually dechorionated and fixed using 4% paraformaldehyde in 0.1M sodium phosphate buffer (pH 7.4) at 4°C. After two hours in the fixative, embryos were washed three times with the same buffer, dehydrated in ethanol, and then embedded in Lowicryl K4M resin at -20°C following the progressive

lowering of temperature (PLT) protocol.[108] The polymer block containing the zebrafish embryo was trimmed with a diamond saw (Buehler Isomet 1000, Germany) coplanar to the frontal plane on the ventral side of the embryo. The resulting plane was mounted onto a microscope slide with UV curing glue (Panacol Vitralit, Germany), and 4 contact-free line sections around the embryo were performed with a femtosecond laser system (TissueSurgeon, LLS Rowiak LaserLabSolutions, Germany). Two of the sections were placed on each lateral side at a distance of 60 µm from the embryo, one section at 60 µm from the caudal end and perpendicular to the two lateral sections, and one section at 500 µm from the cranial end of the embryo, again perpendicular to the lateral sections. To remove metal contaminations and ridges from the diamond saw, an additional coplanar section below the ventral side of the embryo was performed at a distance of 60 µm from the embryo. For sample adjustment and quality control, optical coherence tomography (OCT) images were acquired with a spectral radar system (Thorlabs) modified for integration in TissueSurgeon. The peak wavelength of the OCT light source is 930 nm, offering an axial resolution of 5–7 µm and lateral resolution of <5 µm within the focal plane. Brightfield images were acquired with an integrated CCD-camera (768 x 494 pixel size). Illumination was realized with a custom-made condenser and a high power LED at a wavelength of 800 nm for optimal transmission across the NIR-optimized objective lens. The excised sample was attached with epoxy glue along the cranial surface onto an aluminum holder for mounting on the kinematic stage of the SXRF tomography setup.

3.5.2 Instrumentation

Synchrotron radiation X-ray fluorescence (SXRF) tomography data were acquired at the 2-ID-E beamline of the Advanced Photon Source (Argonne National Laboratory, Illinois, USA). The beamline is equipped with an undulator and double

monochromator, which provide high brilliance X-rays with a tunable energy range between 8–20 keV. The X-ray beam is focused to a spot size of 0.6 x 0.5 μm^2 using the first order diffraction peak of a 320 μm diameter Fresnel zone plate (Xradia, Carl Zeiss, Germany). Higher order diffraction peaks and scattered photons are blocked by a 30 μm diameter tungsten pinhole (order sorting aperture), which is positioned 10 mm upstream of the sample. To minimize scatter signals from air and ambient argon fluorescence, the sample is placed inside a helium-filled chamber equipped with a kapton window for beam entrance. The sample is mounted on an aluminum stick and placed onto a kinematic holder controlled by a stack of 3 piezo-encoded stages (Physik Instrumente GmbH, Germany), a rotation stage and two lateral stages for aligning the sample along the tomographic rotation axis. For raster-scanning of the sample, the entire chamber is moved by two additional vertical and horizontal stages, which offer step sizes down to 50 nm, and if desired, travel distances up to several millimeters. For each focused spot, a full fluorescence spectrum is acquired using an energy dispersive silicone drift detector (Vortex ME-4 by SII Nano Technology, Northridge, CA) positioned at 90 degrees to the incident beam. The detector snout is placed inside the sample chamber and covered with an off-center aluminum collimator specifically designed for the geometry of the 4-element fluorescence detector. A second kapton window allows the beam to reach a downstream ion chamber for monitoring the signal intensity after passing the sample and all optical components. The change in signal intensity compared to the upstream ion chamber provides an absorption contrast signal of the sample. At the downstream end of the microprobe the transmitted beam enters a custom-built configured charge-integrating silicon detector, which provides differential phase contrast.[109] All motorized stages are controlled through EPICS (Experimental Physics and Industrial Control System, Argonne National Laboratory).

3.5.3 Data Acquisition

The SXRF tomographic data set of the zebrafish specimen was composed of 60 projections acquired at intervals of 3 degrees covering a total angular space of 180 degrees. To minimize errors introduced through radiation damage and potential registration drifts, the projections were acquired in two batches with a 3 degree offset and 6 degree intervals. For each orientation, the specimen was translated through the stationary beam with excitation at 10 keV and a step size of 2 µm, covering a total scan area of 840 x 1562 µm. To minimize the data collection time, horizontal scans were acquired in a continuous motion mode[110] with an average dwell time of 10 ms per pixel. Composed of ~20 million individual emission spectra, the complete tomographic data set required over 100 hours of beam time.

3.5.4 Data Processing and Tomographic Reconstruction

For each projection angle elemental maps were generated by Gaussian fitting of the averaged raw emission spectra from 3 x 3 adjacent pixels (2D boxcar averaging) using the MAPS software package.[61] The Gaussian peaks were matched to the characteristic X-ray emission lines to determine the fluorescence signal for zinc, copper, and iron. Calibration to elemental densities ρ (µg cm $^{-2}$) was achieved by comparing the fluorescence emission of the sample with that of a thin film standard (Axo Dresden, Germany) relative to the photon flux captured by two ion chambers positioned upstream and downstream of the sample (see also above description of the instrumentation). Due to signal attenuation by the resin, calibration relative to the up- and downstream photon fluxes yielded either underestimated or overestimated densities ρ_{us} and ρ_{ds},

respectively. The two values are related to the linear attenuation coefficient μ_{ex} and attenuation pathlength *l* according to the Beer–Lambert law (1)

$$\rho_{us} = \rho_{ds} \cdot e^{-l\mu_{ex}} \qquad (1)$$

The absorption contrast generated by the sample can be judged based on the ratio between the photon counts of the upstream and downstream ion chambers. Concluding from the transmission profile across the sample, the embedding material is responsible for the majority of the beam attenuation. With excitation at 10 keV, the transmission is reduced to 77% across the pathlength of the Lowicryl matrix, and only lowered to 75% by the yolk, which corresponds to the largest volume of the specimen. For this reason, we approximated the elemental concentrations in the reconstructed model only based on the corresponding linear attenuation coefficients of the matrix and the average attenuation pathlength *l*. The 3D elemental distributions were reconstructed based on downstream-calibrated projections, which were imported into MATLAB (R2012b), normalized to the integrated density averaged over all projections, and processed using custom made MATLAB codes. For reconstructions based on the filtered back projection algorithm, the elemental maps were processed with the *iradon* routine using the ‘‘Ram–Lak’’ ramp-filter as implemented in the MATLAB Image Processing Toolbox. The code for maximum likelihood expectation maximization (MLEM) reconstruction was derived from the standard iterative algorithm[111] employing the *radon* and unfiltered *iradon* MATLAB routines for projection and back-projection, respectively. Prior to processing of the actual experimental data set, the performance of the code was evaluated based on the reconstruction accuracy of a computer generated Shepp–Logan phantom image. To generate volumetric elemental distributions of the zebrafish 24 hpf, sinograms were derived for each of the 781 *y*-positions and the corresponding 2D elemental densities were iteratively reconstructed using the MLEM code. For the

reconstruction of the zinc distribution a total of 70 iterations were employed. To improve signal-to-noise ratios, the iron and copper data sets were processed with smaller iteration numbers of 30 and 15, respectively. Iteration values of 15 for zinc and 7 for iron were used for the 48 hpf embryo. To gauge the quality of the reconstructed volumetric data sets, projections for each of the 60 acquisition angles were computed and the corresponding difference images derived based on the original measured projections. The final elemental distributions were estimated by converting the pixel-based area densities of each slice to voxel-based concentrations, followed by linear scaling.

3.5.5 Data Visualization

All volumetric renderings were generated with the Paraview software package.[112] For this purpose, the reconstructed volumetric data were exported from MATLAB as 32-bit *z*-stacks, converted to 16-bit stacks using ImageJ,[113] and then imported into Paraview for 3D processing and visualization.

3.6 Literature Cited

1. McRae, R., Lai, B. & Fahrni, C.J. Subcellular redistribution and mitotic inheritance of transition metals in proliferating mouse fibroblast cells. *Metallomics* **5**, 52-61 (2013).

2. Miyares, R.L., de Rezende, V.B. & Farber, S.A. Zebrafish yolk lipid processing: a tractable tool for the study of vertebrate lipid transport and metabolism. *Disease Models & Mechanisms* **7**, 915-927 (2014).

3. Blackburn, D.G. Evolution of vertebrate viviparity and specializations for fetal nutrition: A quantitative and qualitative analysis. *Journal of Morphology* **276**, 961-990 (2015).

4. Katoh, Y., Sato, T. & Yamamoto, Y. Determination of multielement concentrations in normal human organs from the Japanese. *Biological Trace Element Research* **90**, 57-70 (2002).

5. Ma, S.M., Lee, S.G., Kim, E.B., Park, T.J., Seluanov, A., Gorbunova, V., Buffenstein, R., Seravalli, J. & Gladyshev, V.N. Organization of the mammalian ionome according to organ origin, lineage specialization, and longevity. *Cell Reports* **13**, 1319-1326 (2015).

6. Falchuk, K.H., Fawcett, D.W. & Vallee, B.L. Role of zinc in cell-division of Euglena-Gracilis. *Journal of Cell Science* **17**, 57-78 (1975).

7. MacDonald, R.S. The role of zinc in growth and cell proliferation. *Journal of Nutrition* **130**, 1500S-1508S (2000).

8. Beyersmann, D. & Haase, H. Functions of zinc in signaling, proliferation and differentiation of mammalian cells. *Biometals* **14**, 331-341 (2001).

9. Cohen, L., Sekler, I. & Hershfinkel, M. The zinc sensing receptor, ZnR/GPR39, controls proliferation and differentiation of colonocytes and thereby tight junction formation in the colon. *Cell Death & Disease* **5**(2014).

10. Plum, L.M., Rink, L. & Haase, H. The essential toxin: Impact of zinc on human health. *International Journal of Environmental Research and Public Health* **7**, 1342-1365 (2010).

11. Beard, J. Iron deficiency alters brain development and functioning. *Journal of Nutrition* **133**, 1468S-1472S (2003).

12. Terrin, G., Canani, R.B., Di Chiara, M., Pietravalle, A., Aleandri, V., Conte, F. & De Curtis, M. Zinc in early life: A key element in the fetus and preterm neonate. *Nutrients* **7**, 10427-10446 (2015).

13. Dreosti, I.E., Record, I.R. & Manuel, S.J. Zinc deficiency and the developing embryo. *Biological Trace Element Research* **7**, 103-122 (1985).

14. Gambling, L. & McArdle, H.J. Iron, copper and fetal development. *Proceedings of the Nutrition Society* **63**, 553-562 (2004).

15. Bedwal, R.S. & Bahuguna, A. Zinc, copper and selenium in reproduction. *Experientia* **50**, 626-640 (1994).

16. Westerfield, M. *The zebrafish book. A guide for the laboratory use of zebrafish (Danio rerio)*, (University of Oregon Press, Eugene, 2000).

17. Bourassa, M.W. & Miller, L.M. Metal imaging in neurodegenerative diseases. *Metallomics* **4**, 721-738 (2012).

18. Fahrni, C.J. Biological applications of X-ray fluorescence microscopy: Exploring the subcellular topography and speciation of transition metals. *Current Opinion in Chemical Biology* **11**, 121-127 (2007).

19. Kosior, E., Bohic, S., Suhonen, H., Ortega, R., Deves, G., Carmona, A., Marchi, F., Guillet, J.F. & Cloetens, P. Combined use of hard X-ray phase contrast imaging and X-ray fluorescence microscopy for sub-cellular metal quantification. *Journal of Structural Biology* **177**, 239-247 (2012).

20. Ortega, R., Deves, G. & Carmona, A. Bio-metals imaging and speciation in cells using proton and synchrotron radiation X-ray microspectroscopy. *Journal of the Royal Society Interface* **6**, S649-S658 (2009).

21. Paunesku, T., Vogt, S., Maser, J., Lai, B. & Woloschak, G. X-ray fluorescence microprobe imaging in biology and medicine. *Journal of Cellular Biochemistry* **99**, 1489-1502 (2006).

22. Qin, Z., Caruso, J.A., Lai, B., Matusch, A. & Becker, J.S. Trace metal imaging with high spatial resolution: Applications in biomedicine. *Metallomics* **3**, 28-37 (2011).

23. McRae, R., Bagchi, P., Sumalekshmy, S. & Fahrni, C.J. In situ imaging of metals in cells and tissues. *Chemical Reviews* **109**, 4780-4827 (2009).

24. Pushie, M.J., Pickering, I.J., Korbas, M., Hackett, M.J. & George, G.N. Elemental and chemically specific X-ray fluorescence imaging of biological systems. *Chemical Reviews* **114**, 8499-8541 (2014).

25. Sugiyama, M. & Sigesato, G. A review of focused ion beam technology and its applications in transmission electron microscopy. *Journal of Electron Microscopy* **53**, 527-536 (2004).

26. Zierold, K. Limitations and prospects of biological electron probe X-ray microanalysis. *Journal of Trace and Microprobe Techniques* **20**, 181-196 (2002).

27. Bertrand, M., Weber, G. & Schoefs, B. Metal determination and quantification in biological material using particle-induced X-ray emission. *Trac-Trends in Analytical Chemistry* **22**, 254-262 (2003).

28. van Hove, E.R.A., Smith, D.F. & Heeren, R.M.A. A concise review of mass spectrometry imaging. *Journal of Chromatography A* **1217**, 3946-3954 (2010).

29. Boxer, S.G., Kraft, M.L. & Weber, P.K. Advances in imaging secondary ion mass spectrometry for biological samples. in *Annual Review of Biophysics*, Vol. 38 53-74 (2009).

30. Becker, J.S., Matusch, A. & Wu, B. Bioimaging mass spectrometry of trace elements - recent advance and applications of LA-ICP-MS: A review. *Analytica Chimica Acta* **835**, 1-18 (2014).

31. Russo, R.E., Mao, X.L., Liu, H.C., Gonzalez, J. & Mao, S.S. Laser ablation in analytical chemistry - a review. *Talanta* **57**, 425-451 (2002).

32. Limbeck, A., Galler, P., Bonta, M., Bauer, G., Nischkauer, W. & Vanhaecke, F. Recent advances in quantitative LA-ICP-MS analysis: challenges and solutions in the life sciences and environmental chemistry. *Analytical and Bioanalytical Chemistry* **407**, 6593-6617 (2015).

33. Pozebon, D., Scheffler, G.L., Dressler, V.L. & Nunes, M.A.G. Review of the applications of laser ablation inductively coupled plasma mass spectrometry (LA-ICP-MS) to the analysis of biological samples. *Journal of Analytical Atomic Spectrometry* **29**, 2204-2228 (2014).

34. Lobinski, R., Moulin, C. & Ortega, R. Imaging and speciation of trace elements in biological environment. *Biochimie* **88**, 1591-1604 (2006).

35. Hare, D.J., Lee, J.K., Beavis, A.D., van Gramberg, A., George, J., Adlard, P.A., Finkelstein, D.I. & Doble, P.A. Three-dimensional atlas of iron, copper, and zinc in the mouse cerebrum and brainstem. *Analytical Chemistry* **84**, 3990-3997 (2012).

36. Roomans, G.M. & vonEuler, A. X-ray microanalysis in cell biology and cell pathology. *Cell Biology International* **20**, 103-109 (1996).

37. Deves, G., Cohen-Bouhacina, T. & Ortega, R. Scanning transmission ion microscopy mass measurements for quantitative trace element analysis within biological samples and validation using atomic force microscopy thickness measurements. *Spectrochimica Acta Part B-Atomic Spectroscopy* **59**, 1733-1738 (2004).

38. Reinert, T., Spemann, D., Morawski, M. & Arendt, T. Quantitative trace element analysis with sub-micron lateral resolution. *Nuclear Instruments & Methods in Physics Research Section B-Beam Interactions with Materials and Atoms* **249**, 734-737 (2006).

39. Carmona, A., Deves, G. & Ortega, R. Quantitative micro-analysis of metal ions in subcellular compartments of cultured dopaminergic cells by combination of three ion beam techniques. *Analytical and Bioanalytical Chemistry* **390**, 1585-1594 (2008).

40. Verissimo, A., Alves, L.C., Filipe, P., Silva, J.N., Silva, R., Ynsa, M.D., Gontier, E., Moretto, P., Pallon, J. & Pinheiro, T. Nuclear microscopy: A tool for and percutaneous absorption imaging elemental distribution in vivo. *Microscopy Research and Technique* **70**, 302-309 (2007).

41. Hong-Hermesdorf, A., Miethke, M., Gallaher, S.D., Kropat, J., Dodani, S.C., Chan, J., Barupala, D., Domaille, D.W., Shirasaki, D.I., Loo, J.A., Weber, P.K., Pett-Ridge, J., Stemmler, T.L., Chang, C.J. & Merchant, S.S. Subcellular metal imaging identifies dynamic sites of Cu accumulation in Chlamydomonas. *Nature Chemical Biology* **10**, 1034-+ (2014).

42. Herzog, R.F.K. & Viehbock, F.P. Ion source for mass spectrography. *Physical Review* **76**, 855-856 (1949).

43. Liebl, H. Ion microprobe mass analyzer. *Journal of Applied Physics* **38**, 5277-& (1967).

44. Wang, H.A.O., Grolimund, D., Giesen, C., Borca, C.N., Shaw-Stewart, J.R.H., Bodenmiller, B. & Gunther, D. Fast chemical imaging at high spatial resolution by laser ablation inductively coupled plasma mass spectrometry. *Analytical Chemistry* **85**, 10107-10116 (2013).

45. Wang, S., Brown, R. & Gray, D.J. Application of laser ablation-ICPMS to the spatially-resolved microanalysis of biological tissue. *Applied Spectroscopy* **48**, 1321-1325 (1994).

46. Giesen, C., Wang, H.A.O., Schapiro, D., Zivanovic, N., Jacobs, A., Hattendorf, B., Schuffler, P.J., Grolimund, D., Buhmann, J.M., Brandt, S., Varga, Z., Wild, P.J., Gunther, D. & Bodenmillerthat, B. Highly multiplexed imaging of tumor tissues with subcellular resolution by mass cytometry. *Nature Methods* **11**, 417-+ (2014).

47. Gray, A.L. Solid sample introduction by laser ablation for inductively couple plasma source-mass spectrometry. *Analyst* **110**, 551-556 (1985).

48. Becker, J.S., Zoriy, M., Dressler, V.L. & Wu, B. Imaging of metals and metal-containing species in biological tissues and on gels by laser ablation inductively coupled plasma mass spectrometry (LA-ICP-MS): A new analytical strategy for applications in life sciences. *Pure and Applied Chemistry* **80**, 2643-2655 (2008).

49. Becker, J.S., Zoriy, M., Wu, B. & Matusch, A. Imaging of essential and toxic elements in biological tissues by LA-ICP-MS. *Journal of Analytical Atomic Spectrometry* **23**, 1275-1280 (2008).

50. Becker, J.S., Zoriy, M., Dobrowolska, J. & Matusch, A. Laser ablation inductively coupled plasma mass spectrometry (LA-ICP-MS) in elemental imaging of biological tissues and in proteomicsw. *Journal of Analytical Atomic Spectrometry* **22**, 736-744 (2007).

51. Kindness, A., Sekaran, C.N. & Feldmann, J. Two-dimensional mapping of copper and zinc in liver sections by laser ablation-inductively coupled plasma mass spectrometry. *Clinical Chemistry* **49**, 1916-1923 (2003).

52. Gao, Y., Liu, N.Q., Chen, C.Y., Luo, Y.F., Li, Y.F., Zhang, Z.Y., Zhao, Y.L., Zhao, B.L., Iida, A. & Chai, Z.F. Mapping technique for biodistribution of elements in a model organism, Caenorhabditis elegans, after exposure to copper nanoparticles with microbeam synchrotron radiation X-ray fluorescence. *Journal of Analytical Atomic Spectrometry* **23**, 1121-1124 (2008).

53. Korbas, M., Lai, B., Vogt, S., Gleber, S.C., Karunakaran, C., Pickering, I.J., Krone, P.H. & George, G.N. Methylmercury targets photoreceptor outer segments. *Acs Chemical Biology* **8**, 2256-2263 (2013).

54. de Jonge, M.D. & Vogt, S. Hard X-ray fluorescence tomography - an emerging tool for structural visualization. *Current Opinion in Structural Biology* **20**, 606-614 (2010).

55. Bleuet, P., Lemelle, L., Tucoulou, R., Gergaud, P., Delette, G., Cloetens, P., Susini, J. & Simionovici, A. 3D chemical imaging based on a third-generation synchrotron source. *Trac-Trends in Analytical Chemistry* **29**, 518-527 (2010).

56. Kim, S.A., Punshon, T., Lanzirotti, A., Li, L.T., Alonso, J.M., Ecker, J.R., Kaplan, J. & Guerinot, M.L. Localization of iron in Arabidopsis seed requires the vacuolar membrane transporter VIT1. *Science* **314**, 1295-1298 (2006).

57. de Jonge, M.D., Holzner, C., Baines, S.B., Twining, B.S., Ignatyev, K., Diaz, J., Howard, D.L., Legnini, D., Miceli, A., McNulty, I., Jacobsen, C.J. & Vogt, S. Quantitative 3D elemental microtomography of Cyclotella meneghiniana at 400-nm resolution. *Proceedings of the National Academy of Sciences of the United States of America* **107**, 15676-15680 (2010).

58. McColl, G., James, S.A., Mayo, S., Howard, D.L., Ryan, C.G., Kirkham, R., Moorhead, G.F., Paterson, D., de Jonge, M.D. & Bush, A.I. Caenorhabditis elegans maintains highly compartmentalized cellular distribution of metals and steep concentration gradients of manganese. *Plos One* **7**(2012).

59. Kirkpatrick, P. & Baez, A.V. Formation of optical images by x-rays. *Journal of the Optical Society of America* **38**, 766-774 (1948).

60. Morawe, C. & Osterhoff, M. Curved graded multilayers for X-ray nano-focusing optics. *Nuclear Instruments & Methods in Physics Research Section a-Accelerators Spectrometers Detectors and Associated Equipment* **616**, 98-104 (2010).

61. Vogt, S. MAPS: A set of software tools for analysis and visualization of 3D X-ray fluorescence data sets. *Journal De Physique Iv* **104**, 635-638 (2003).

62. Ayache, J., Beaunier, L., Boumendil, J., Ehret, G. & Laub, D. *Sample preparation handbook for transmission electron microscopy*, 338 (Springer, 2010).

63. Ho, E., Dukovcic, S., Hobson, B., Wong, C.P., Miller, G., Hardin, K., Traber, M.G. & Tanguay, R.L. Zinc transporter expression in zebrafish (Danio rerio) during development. *Comparative Biochemistry and Physiology C-Toxicology & Pharmacology* **155**, 26-32 (2012).

64. Smith, S.W. Special Imaging Techniques. in *The Scientist and Engineer's Guide to Digital Signal Processing* 423 - 450 (California Technical Publishing, San Diego, California, 1997).

65. Bourassa, D., Gleber, S.C., Vogt, S., Yi, H., Will, F., Richter, H., Shin, C.H. & Fahrni, C.J. 3D imaging of transition metals in the zebrafish embryo by X-ray fluorescence microtomography. *Metallomics* **6**, 1648-1655 (2014).

66. Kimmel, C.B., Ballard, W.W., Kimmel, S.R., Ullmann, B. & Schilling, T.F. Stages of embryonic-development of the zebrafish. *Developmental Dynamics* **203**, 253-310 (1995).

67. Parker, L.H., Zon, L.I. & Stainier, D.Y.R. Vascular and blood gene expression. *Methods in Cell Biology, Vol 59* **59**, 313-+ (1999).

68. Donovan, A., Brownlie, A., Zhou, Y., Shepard, J., Pratt, S.J., Moynihan, J., Paw, B.H., Drejer, A., Barut, B., Zapata, A., Law, T.C., Brugnara, C., Kingsley, P.D., Palis, J., Fleming, M.D., Andrews, N.C. & Zon, L.I. Positional cloning of zebrafish ferroportin1 identifies a conserved vertebrate iron exporter. *Nature* **403**, 776-781 (2000).

69. Mudumana, S.P., Wan, H.Y., Singh, M., Korzh, V. & Gong, Z.Y. Expression analyses of zebrafish transferrin, ifabp, and elastaseB mRNAs as differentiation markers for the three major endodermal organs: Liver, intestine, and exocrine pancreas. *Developmental Dynamics* **230**, 165-173 (2004).

70. Ben-Horin, S., Shinfeld, A., Kachel, E., Chetrit, A. & Livneh, A. The composition of normal pericardial fluid and its implications for diagnosing pericardial effusions. *American Journal of Medicine* **118**, 636-640 (2005).

71. Field, H.A., Ober, E.A., Roeser, T. & Stainier, D.Y.R. Formation of the digestive system in zebrafish. I. Liver morphogenesis. *Developmental Biology* **253**, 279-290 (2003).

72. Soules, K.A. & Link, B.A. Morphogenesis of the anterior segment in the zebrafish eye. *Bmc Developmental Biology* **5**(2005).

73. Ugarte, M., Grime, G.W., Lord, G., Geraki, K., Collingwood, J.F., Finnegan, M.E., Farnfield, H., Merchant, M., Bailey, M.J., Ward, N.I., Foster, P.J., Bishop, P.N. & Osborne, N.N. Concentration of various trace elements in the rat retina and their distribution in different structures. *Metallomics* **4**, 1245-1254 (2012).

74. Ugarte, M., Osborne, N.N., Brown, L.A. & Bishop, P.N. Iron, zinc, and copper in retinal physiology and disease. *Survey of Ophthalmology* **58**, 585-609 (2013).

75. Ugarte, M. & Osborne, N.N. Zinc in the retina. *Progress in Neurobiology* **64**, 219-249 (2001).

76. Ripps, H. & Chappell, R.L. Review: Zinc's functional significance in the vertebrate retina. *Molecular Vision* **20**, 1067-1074 (2014).

77. Moiseyev, G., Takahashi, Y., Chen, Y., Gentleman, S., Redmond, T.M., Crouch, R.K. & Ma, J.X. RPE65 is an iron(II)-dependent isomerohydrolase in the retinoid visual cycle. *Journal of Biological Chemistry* **281**, 2835-2840 (2006).

78. Wang, X., Wang, Z.Y., Gao, H.L., Danscher, G. & Huang, L.P. Localization of ZnT7 and zinc ions in mouse retina - Immunohistochemistry and selenium autometallography. *Brain Research Bulletin* **71**, 91-96 (2006).

79. Akagi, T., Kaneda, M., Ishii, K. & Hashikawa, T. Differential subcellular localization of zinc in the rat retina. *Journal of Histochemistry & Cytochemistry* **49**, 87-96 (2001).

80. Lengyel, I., Flinn, J.M., Peto, T., Linkous, D.H., Cano, K., Bird, A.C., Lanzirotti, A., Frederickson, C.J. & van Kuijk, F. High concentration of zinc in sub-retinal pigment epithelial deposits. *Experimental Eye Research* **84**, 772-780 (2007).

81. Redenti, S. & Chappell, R.L. Localization of zinc transporter-3 (ZnT-3) in mouse retina. *Vision Res* **44**, 3317-21 (2004).

82. Yin, S.J., Chou, C.F., Lai, C.L., Lee, S.L. & Han, C.L. Human class IV alcohol dehydrogenase: kinetic mechanism, functional roles and medical relevance. *Chemico-Biological Interactions* **143**, 219-227 (2003).

83. Huber, A.M. & Gershoff, S.N. Effects of zinc-deficiency on oxidation of retinol and ethanol in rats. *Journal of Nutrition* **105**, 1486-1490 (1975).

84. Redenti, S. & Chappell, R.L. Neuroimaging of zinc released by depolarization of rat retinal cells. *Vision Res* **45**, 3520-5 (2005).

85. Rajan, M.T., Rao, K.S.J., Mamatha, B.M., Rao, R.V., Shanmugavelu, P., Menon, R.B. & Pavithran, M.V. Quantification of trace elements in normal human brain by inductively coupled plasma atomic emission spectrometry. *Journal of the Neurological Sciences* **146**, 153-166 (1997).

86. Duflou, H., Maenhaut, W. & Dereuck, J. Regional distribution of potassium, calcium, and 6 trace-elements in normal human-brain. *Neurochemical Research* **14**, 1099-1112 (1989).

87. Popescu, B.F.G., Robinson, C.A., Rajput, A., Rajput, A.H., Harder, S.L. & Nichol, H. Iron, copper, and zinc distribution of the cerebellum. *Cerebellum* **8**, 74-79 (2009).

88. Beard, J.L., Connor, J.R. & Jones, B.C. Iron in the brain. *Nutrition Reviews* **51**, 157-170 (1993).

89. Bitanihirwe, B.K.Y. & Cunningham, M.G. Zinc: The brain's dark horse. *Synapse* **63**, 1029-1049 (2009).

90. Connor, J.R., Menzies, S.L., Stmartin, S.M. & Mufson, E.J. Cellular-distribution of transferrin, ferritin, and iron in normal and aged human brains. *Journal of Neuroscience Research* **27**, 595-611 (1990).

91. Taylor, E.M. & Morgan, E.H. DEVELOPMENTAL-Changes in transferrin and iron uptake by the brain in the rat. *Developmental Brain Research* **55**, 35-42 (1990).

92. Jeong, J.Y., Einhorn, Z., Mathur, P., Chen, L.S., Lee, S., Kawakami, K. & Guo, S. Patterning the zebrafish diencephalon by the conserved zinc-finger protein Fezl. *Development* **134**, 127-136 (2007).

93. Hashimoto, H., Yabe, T., Hirata, T., Shimizu, T., Bae, Y., Yamanaka, Y., Hirano, T. & Hibi, M. Expression of the zinc finger gene fez-like in zebrafish forebrain. *Mechanisms of Development* **97**, 191-195 (2000).

94. Hirata, T., Nakazawa, M., Muraoka, O., Nakayama, R., Suda, Y. & Hibi, M. Zinc-finger genes Fez and Fez-like function in the establishment of diencephalon subdivisions. *Development* **133**, 3993-4004 (2006).

95. Close, R., Toro, S., Martial, J.A. & Muller, M. Expression of the zinc finger Egr1 gene during zebrafish embryonic development. *Mechanisms of Development* **118**, 269-272 (2002).

96. Drummond, I.A., Rohwernutter, P. & Sukhatme, V.P. The zebrafish Egr1 gene encodes a highly conserved, zinc-finger transcriptional regulator. *DNA and Cell Biology* **13**, 1047-1055 (1994).

97. McMahon, A.P., Champion, J.E., McMahon, J.A. & Sukhatme, V.P. Developmental expression of the putative transcription factor Egr-1 suggests that Egr-1 and C-fos are coregulated in some tissues. *Development* **108**, 281-287 (1990).

98. Stemple, D.L. Structure and function of the notochord: An essential organ for chordate development. *Development* **132**, 2503-2512 (2005).

99. Kanki, J.P. & Ho, R.K. The development of the posterior body in zebrafish. *Development* **124**, 881-893 (1997).

100. Yan, G., Zhang, Y.C., Yu, J.L., Yu, Y., Zhang, F., Zhang, Z.Z., Wu, A.M., Yan, X.H., Zhou, Y. & Wang, F.D. Slc39a7/zip7 plays a critical role in development and zinc homeostasis in zebrafish. *Plos One* **7**(2012).

101. Carvalho, L. & Heisenberg, C.-P. The yolk syncytial layer in early, zebrafish development. *Trends in Cell Biology* **20**, 586-592 (2010).

102. Hellman, N.E. & Gitlin, J.D. Ceruloplasmin metabolism and function. *Annual Review of Nutrition* **22**, 439-458 (2002).

103. Korzh, S., Emelyanov, A. & Korzh, V. Developmental analysis of ceruloplasmin gene and liver formation in zebrafish. *Mechanisms of Development* **103**, 137-139 (2001).

104. Ishizaki, H., Spitzer, M., Wildenhain, J., Anastasaki, C., Zeng, Z.Q., Dolma, S., Shaw, M., Madsen, E., Gitlin, J., Marais, R., Tyers, M. & Patton, E.E. Combined zebrafish-yeast chemical-genetic screens reveal gene-copper-nutrition interactions that modulate melanocyte pigmentation. *Disease Models & Mechanisms* **3**, 639-651 (2010).

105. Setty, S.R.G., Tenza, D., Sviderskaya, E.V., Bennett, D.C., Raposo, G. & Marks, M.S. Cell-specific ATP7A transport sustains copper-dependent tyrosinase activity in melanosomes. *Nature* **454**, 1142-U75 (2008).

106. Martin, B.L. & Kimelman, D. Wnt signaling and the evolution of embryonic posterior development. *Current Biology* **19**, R215-R219 (2009).

107. Sugiyama, M., Sakaue-Sawano, A., Iimura, T., Fukami, K., Kitaguchi, T., Kawakami, K., Okamoto, H., Higashijima, S.I. & Miyawaki, A. Illuminating cell-cycle progression in the developing zebrafish embryo. *Proceedings of the National Academy of Sciences of the United States of America* **106**, 20812-20817 (2009).

108. Armbruster, B.L., Carlemalm, E., Chiovetti, R., Garavito, R.M., Hobot, J.A., Kellenberger, E. & Villiger, W. Specimen preparation for electron-microscopy using low-temperature embedding resins. *Journal of Microscopy-Oxford* **126**, 77-85 (1982).

109. Hornberger, B., de Jonge, M.D., Feser, M., Holl, P., Holzner, C., Jacobsen, C., Legnini, D., Paterson, D., Rehak, P., Strueder, L. & Vogt, S. Differential phase contrast with a segmented detector in a scanning X-ray microprobe. *Journal of Synchrotron Radiation* **15**, 355-362 (2008).

110. Barrea, R.A., Gore, D., Kujala, N., Karanfil, C., Kozyrenko, S., Heurich, R., Vukonich, M., Huang, R., Paunesku, T., Woloschak, G. & Irving, T.C. Fast-scanning high-flux microprobe for biological X-ray fluorescence microscopy and microXAS. *Journal of Synchrotron Radiation* **17**, 522-529 (2010).

111. Zeng, G.L. Medical image reconstruction: A conceptual tutorial. *Medical Image Reconstruction: a Conceptual Tutorial*, 1-198 (2010).

112. Paraview 4.0. (Kitware, Inc., Clifton Park, New York, 2013).

113. Schneider, C.A., Rasband, W.S. & Eliceiri, K.W. NIH Image to ImageJ: 25 years of image analysis. *Nature Methods* **9**, 671-675 (2012).

CHAPTER 4

INVESTIGATING LABILE ZINC POOLS DURING ZEBRAFISH EMBRYOGENESIS

While zinc is recognized for its importance during fertilization and early embryogenesis, it continues to be necessary throughout the life of an organism. For example, some organs such as the prostate, kidney, eye and brain require a higher zinc concentration for their normal function.[1] Given the limited external supply of nutrients during embryogenesis, developing organs most likely redistribute these essential micronutrients from neighboring cells to satisfy their increased demand, thus raising the intriguing and fundamental question of how the limited supply of trace metals in the yolk of a fertilized egg is redistributed in the course of embryonic development.

Despite the established importance of zinc in embryogenesis and development, little is understood regarding the mechanisms of the redistribution and organization of zinc during these vital processes. SXRF microscopy data (Chapter 3) can only provide the total zinc content of the specimen. Similar to the cell culture studies performed in Chapter 2, the next step in understanding zinc distribution is to investigate the labile zinc in comparison to the total zinc information acquired with SXRF microscopy. To further investigate, the Zn(II)-selective fluorescent probe, Chromis1, was used in combination with zebrafish model systems to study the redistribution dynamics of labile Zn(II) pools in a zebrafish embryo during the first 24 hours post fertilization.

4.1 Background

The importance of zinc for cellular proliferation and growth is well established.[2] As the maternally derived yolk stores are the primary source of nutrients for the embryo, this pool supplies all developing tissues and organs with zinc, likely orchestrated through an elaborate network of zinc transporters.[3] For these reasons, synchrotron X-ray

fluorescence (SXRF) tomography was initially utilized to detect total metal content of a developing embryo.[4] The SXRF tomography data discussed in Chapters 3 provided intriguing insight into the total metal distribution of a zebrafish embryo at two different stages of development. In both pharyngula and early hatching periods the SXRF revealed over 80% of the zinc is found in the yolk while copper and iron are predominantly in the body of the embryo, leaving the yolk almost void. Additionally, the highest concentration of zinc is observed in the tip of the tail during both stages of embryogenesis. Presumably, zinc is mobilized and sequestered in to these areas. These two distinct accumulations are indicative of an essential heterogeneous zinc distribution regulated during development.

4.1.1 Zebrafish as a Model System

As previously mentioned in Chapter 3, zebrafish are an ideal model system for studying metal distribution during embryogenesis. Zebrafish embryos develop as lecithotrophic organisms requiring only the nutrition found in their yolk sac for the first 3 - 4 days post fertilization (dpf).[5,6] This closed system presents a unique opportunity to study the distribution of a set metal content, eliminating the need to account for additional nutrition acquired during feeding. The optically clear

Furthermore, during early zebrafish embryogenesis the cell cycle is atypical with varying cycle lengths and division patterns.[7] The initial cleavage events of a fertilized embryo occur in 15 minute intervals. These early divisions are synchronous, rapid, symmetrical and meroblastic, or incomplete.[7] After 2.25 hours the embryo begins to transition out of the cleavage period and into the blastula period. The cleavages are now considered metasynchronous. They no longer occur at the same time; rather they divide in a wave starting at the animal pole in the center on the blastodisc and move outward. Further into this stage of development cell cycle lengthening begins. Not all of the cell

cycles lengthen to the same extent. The cells begin to differentiate as the blastula period continues and the epiboly begins to form.[8]

Experimentally, zebrafish are a very practical tool to use in the lab. Much smaller than the mouse models, zebrafish can be kept in larger quantities. The high fecundity of the zebrafish allows the researcher to collect hundreds of embryos a week.[9] The large size of the embryo permits them to be easily manipulated or microinjected and the fast, external development is advantageous for development studies. Researchers can observe a zebrafish develop from a single cell to a small fish in 24 hours.[8] Lastly, zebrafish embryos are optically translucent, therefore ideal organisms to partner with fluorescent imaging tools.[10]

4.1.2 Zebrafish Embryogenesis

During the first three days post fertilization zebrafish embryos undergo major morphological changes forming organs, tissues, and growing more than triple in size. Starting with a fertilized single cell during the zygote period, zebrafish embryogenesis can be described as a complex array of developmental stages. Subsequent to the zygote period, the cleavage and blastula periods are primarily characterized by the number of dividing cells on top of the yolk. During the successive gastrula period, a thin layer of cells known as the epiboly engulfs the yolk. Transitioning into segmentation at 10 hpf, the tail bud becomes visible and somite sections of the tail start to form. By 24 hpf the embryo exhibits a developed brain with distinguishable lobes and ventricles and the pharyngula period begins during which the fins being to form. As the hatching period begins at 48 hpf, organs, such as the liver and heart, as well as distinct lens and retina of the eye can be observed. Embryogenesis concludes at 72 hpf as the zebrafish transitions from embryo to larva.[8]

What begins as a single cell containing a defined, fixed amount of trace metals develops into a multicellular organism comprised of various cells, tissues, and organs all with varying trace metal requirements.[11,12] Given the limited external supply of nutrients during embryogenesis, developing organs most likely redistribute zinc from neighboring cells to satisfy their increased demand, thus raising the question of how the limited supplies of zinc in a fertilized egg is redistributed in the course of embryonic development.

4.1.3 Previous Fluorescence Microscopy Studies in Zebrafish

As optically transparent organisms, zebrafish have been widely utilized for fluorescence imaging studies. For example, using both a protein-based bioluminescent aequorin imaging method[13-15] and the fluorescent Ca(II) reporter, Calcium Green-1 dextran,[15] extensive research in calcium fluctuations during the fertilization and embryonic development of zebrafish have been reported.[16] These data revealed patterned Ca(II)-mediated intercellular waves permeating each stage of embryogenesis with different concentrations and timing. Activation and fertilization of a zebrafish oocyte triggers a rapid increase of calcium in the oocyte cortex which continues to increase during the first 12-15 minutes post fertilization.[17] During the cleavage period, close spatial correlation between elevated intracellular calcium and the cleavage furrows of the dividing cells is observed.[18] The blastula period is characterized with localized elevations of calcium, otherwise known as calcium spikes, generated in individual cells throughout the blastoderm.[19] Observations of this nature are only possible using an optically transparent, externally developing embryo such as the zebrafish.

Additionally, Zn(II) imaging in live zebrafish embryos has been reported using various membrane-permeable Zn(II) sensors.[20-23] In all studies, zebrafish between 19 hpf – 5 days post fertilization (dpf) were incubated in the fluorescent sensor for 20 – 90

minutes. Ma et al. reports zebrafish 3 dpf were fed a solution containing Zn(II) at varying concentrations. Using the ratiometric luminescent iridium(III) chemosensor, the zebrafish fed with Zn(II) revealed a red-shifted fluorescence emission in the abdomen indicating an accumulation of Zn(II) compared to blue-shifted fluorescence observed in the abdomens of the the control zebrafish. Additionally, the emission shifted back to that of basal conditions after introducing the strong chelator, TPEN, to the imaging solution surrounding the Zn(II)-fed samples.[20]

Using a synthetic Zn(II) sensor (SBD-TPEA) developed from the Zn(II) chelator, *N,N,N'*-tri(pyridin-2-ylmethyl)-ethane-1,2-diamine (TPEA), and fluorophore sulfamoyl-benzoxadiazole, Liu et al. observed two bright regions of fluorescence located between the eyes of zebrafish larva 3 dpf. This fluorescence was also reversible after introducing TPEN to the imaging solution.[21] Xu et al. report the use of a Zn(II) selective, ratiometric probe (ZTRS) developed from an amide-containing Zn(II) receptor and a napthalimide fluorophore. ZTRS consistently indicated red-shifted fluorescence spots in the anterior region of the yolk at various time points between 19 – 54 hpf. These spots increased with the addition of exogenous Zn(II) and disappeared with the addition of TPEN.[22] Similarly, Qian et al. observed the same spotted pattern using a Zn(II) probe termed NBD-TPEA, designed from the fluorophore 4-amino-7-nitro-2,1,3-benzoxadiazole and the chelator TPEA.[23] Additionally, this probe indicated fluorescent spots between the eyes similar to the fluorescence observed with SBD-TPEA.[21]

4.2 Imaging of Labile Zn(II) Pools in Developing Zebrafish Embryos

Chromis1, the Zn(II)-selective, emission ratiometric probe characterized in Chapter 2, is well suited for ratiometric imaging of labile Zn(II) pools in a wide range of biological environments. Taking advantage of the optically transparent phenotype and their external development, zebrafish are ideal model organism to study using a fluorescent probe.[24] Additionally, their ability to progress from a single cell to resembling a fish in the matter of hours permit the study of various developmental changes in a single day.[8]

To enforce a uniform cytosolic distribution of Chromis1 and avoid accumulation within subcellular compartments, an NHS-ester derivative of Chromis1 was conjugated to 70 kDa amino-functionalized dextran (Figure 4.1). Dextran, a branched polysaccharide composed of glucose molecules, is hydrophilic and therefore unable to cross cellular membranes including those of intracellular organelles where a fluorescent probe may otherwise accumulate. Upon microinjection into the single-cell zygote, the probe remains trapped within the cell and will be passed on to the daughter cells upon cell division. In comparison with membrane-permeate AM esters, cell-permeable dyes, dextran conjugated probes show no compartmentalization and have low toxicity.

Fluorescently labeled dextran conjugates have been widely utilized in lineage labeling of zebrafish cells,[25,26] neuronal tracing studies,[27,28] and imaging calcium waves during embryonic development.[15] Calcium Green-1 dextran is the most common calcium imaging dye used in zebrafish.[16,29] Injections of Calcium Green-1 dextran into embryos at the single-cell stage have revealed calcium fluctuations during fertilization, cleavage and blastula period.[15]

The final 70 kDa dextran conjugate contained an average of 10 probe molecules per dextran and is referred to as Chromis1-dextran in the following sections (Figure 4.1).

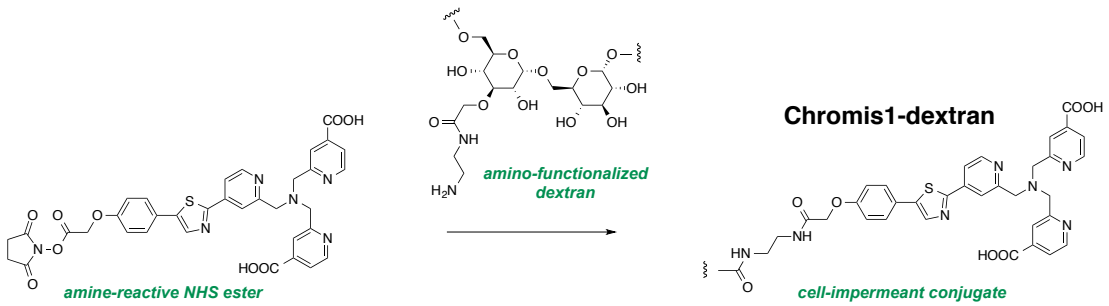

Figure 4.1: Preparation of a 70 kDa dextran conjugate starting from the amine-reactive, NHS-ester functionalized ratiometric Zn(II)-responsive two photon probe. After microinjection, the conjugate cannot cross the plasma membrane and remains trapped within a single cell. Synthesis preformed by Dr. Sumalekshmy Sarojini.

To rule out concerns of hydrolytic cleavage, which would release Chromis1 from the 70 kDa dextran, Chromis1-dextran was co-injected with a rhodamine-dextran conjugate purchased from Invitrogen into a single-cell zebrafish embryo. As in Chromis1-dextran, the rhodamine-dextran was conjugated to a 70 kDa dextran. Indicated in Figure 4.2, the co-injected rhodamine-dextran conjugate and Chromis1-dextran appear to be well distributed throughout the embryo in the blastula stage (4 hpf) and the late segmentation / early pharyngula stage (29 hpf) suggesting the conjugated probe does in fact stay intact. During the blastula stage it is also apparent the neither the rhodamine-dextran conjugate nor Chromis1-dextran have leaked from the blastodisc and into the yolk suggesting the conjugated molecules are prevented from crossing cellular membranes.

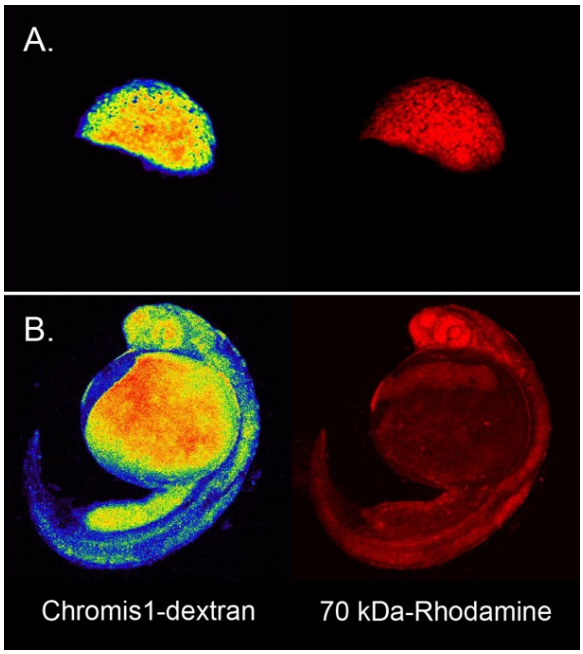

Figure 4.2: Z projection images of Chromis1-dextran and 70 kDa Dextran-Rhodamine co-injection. 4 nL of a 2:1 mixture of Chromis1-dextran: Dextran conjugated rhodamine was injected during the single cell stage of embryogenesis of a wild type zebrafish embryo. **A:** Blastula period, 4 hours post fertilization (hpf), indicates similar distribution of both Chromis1-dextran and 70 kDa dextran-rhodamine. **B:** Pharyngula period, 29 hpf, the dextran-rhodamine conjugation appears evenly distributed throughout the embryos, suggesting the molecule does not form aggregates while the Chromis1-dextran appears to have areas of high concentration indicating labile Zn(II) pools.

4.2.1 Titration Using EDTA In Vivo

Establishing a Zn(II) concentration of a zebrafish embryo is necessary to assess the fractional saturation of Chromis1-dextran in experimental conditions and to better understand the dynamic range of the probe. Without a clear understanding of how much zinc is available for the probe to bind, it is difficult to determine the accuracy of Chromis1-dextran. If there is an abundance of zinc, the probe may be saturated and changes in zinc distribution may be challenging to image. Conversely, if there is very little zinc available the changes may also be difficult to detect.

Conflicting reports cite different amounts of total zinc found inside an entire zebrafish embryo.[3,4,30] Using acid digested oocytes analyzed via atomic absorption spectroscopy, Riggio et al. reports 30 - 100 ng of Zn/oocyte. This amount is size-dependent and appears to increase after fertilization, peaking at 2.45 hpf with over 500 ng of total zinc found in each embryo. This value then decreases over the next two hours, returning to approximately 100 ng per embryo around 5.25 hpf.[30] Conversely, data collected by Ho et al. using inductively coupled plasma - optical emission spectroscopy indicates a much smaller value of 7.5 ng Zn/embryo between 0 - 120 hours post fertilization (hpf).[3] This aligns well with the reported 7.1 ng calculated from the SXRF studies performed on zebrafish 24 hpf and discussed in Chapter 3.[4] Given two of the three independent findings are similar, there is likely 7 - 7.5 ng Zn/embryo.

To verify that the fluorescence emission ratio changes are due to differences in fractional saturation of the probe, the labile Zn(II) pool of embryos at the single-cell stage were titrated with the membrane-impermeant chelator ethylenediaminetetraacetic acid (EDTA). At neutral pH, EDTA exhibits an apparent dissociation constant of 16 fM, which is approximately three orders of magnitude lower compared to the K_d of Chromis1-dextran. Solutions of Chromis1-dextran containing either 200 mM, 400 mM or 500 mM of EDTA were microinjected into the blastodisc of single-cell stage wild type zebrafish embryos. Using the microscope, approximate embryo dimensions were measured. From those measurements, the volume of the single cell on top of the yolk was calculated to be approximately 70 nL. Based on this calculated volume, the approximate volume of 4 nL microinjected based on the instrument parameters, and the concentrations of the prepared EDTA solutions (considering the dilution of EDTA mixing with the 1 mM Chromis1-dextran in a 1:1 ratio) the final intracellular concentrations of EDTA are estimated as 3, 6 and 9 mM, much higher than the calculated final concentration of Chromis1-dextran (50 μM).

Figure 4.3 illustrates the average emission ratio decreased with increasing EDTA concentration from 1.14 (no EDTA) to 0.69 (9 mM EDTA). These data not only confirm that the ratiometric probe Chromis1-dextran is capable of reporting dynamic changes of Zn(II) availability, but also indicate the presence of a sizable pool of labile Zn(II).

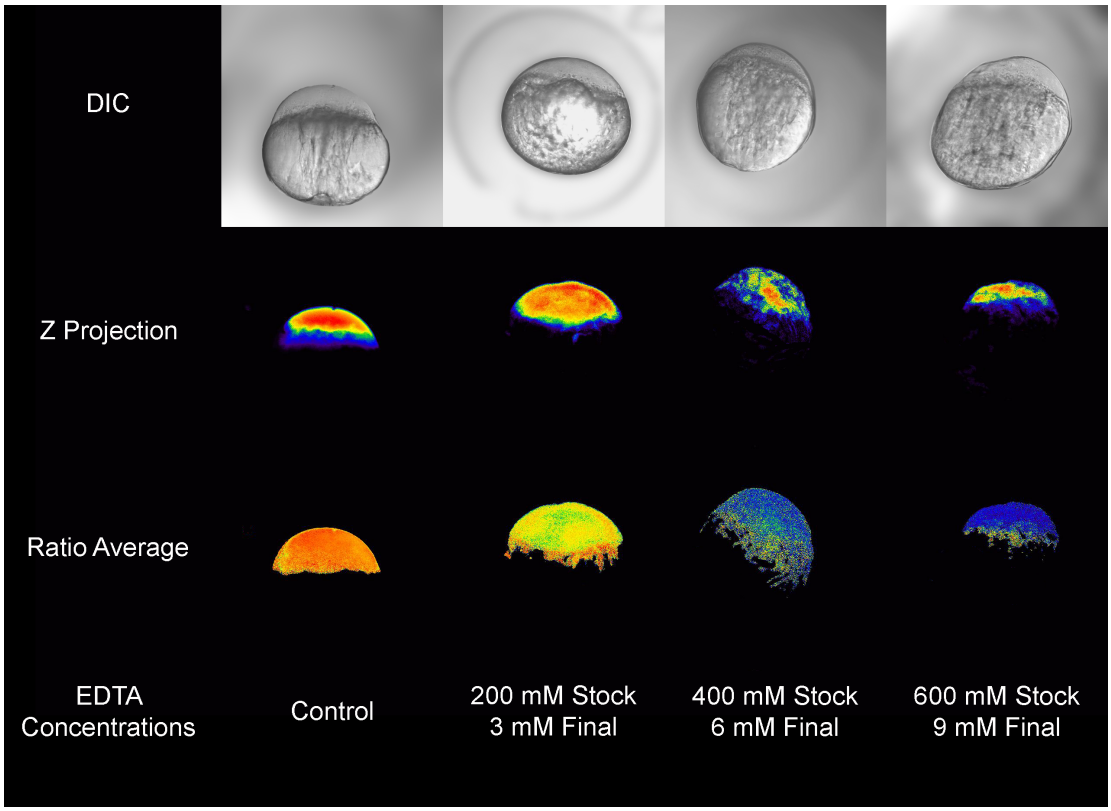

Figure 4.3: High resolution stacks of wild type zebrafish embryos after injection of 1:1 Chromis1-dextran:EDTA mixture. All stacks were obtained within 20 minutes of injection. Only the embryos injected with 200 mM EDTA / Chromis1-dextran developed pass the single cell stage, however they did not survive past 2 divisions. This experiment resulted in a visible drastic drop in saturation as the concentration of EDTA increased.

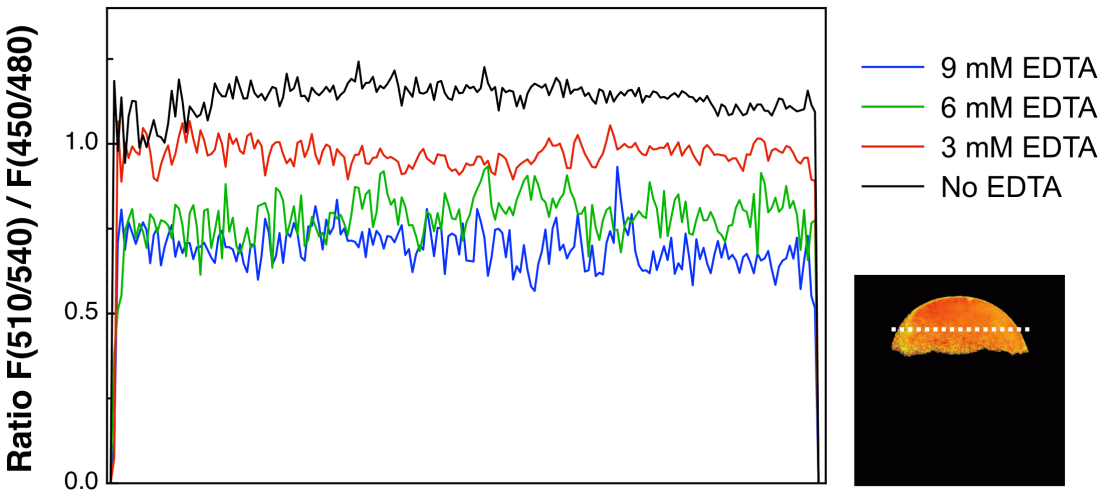

Figure 4.4: Variations in Zn(II) saturation due to concentration of EDTA. High-resolution stacks were imaged (Figure 4.3) and the ratio was calculated on a pixel-by-pixel basis using ImageJ software and the Average Z Projection images. Average ratios were calculated as: no EDTA = 1.14, 3 mM EDTA = 0.96, 6 mM EDTA = 0.77, and 9 mM EDTA = 0.69. Data was collected as indicated on bottom right insert, selecting a single line across each embryo.

4.2.2 Distribution of Labile Zn(II) at Fixed Stages of Development

To explore the distribution of labile Zn(II) pools during early zebrafish embryogenesis, fertilized embryos at the single-cell stage, approximately 15 minutes post fertilization, were microinjected with 4 nL of a 1 mM stock of Chromis1-dextran in physiological buffer (pH 7.2, HEPES, 0.1 M KCl). This results in an approximate 50 μM final probe concentration within the injected cell. For ratiometric two-photon imaging, the embryos were transferred to a glass-bottom Petri-dish containing Danieau's solution and a thin layer of agarose with spherical mounting grooves. Embryonic development was directly followed on-stage by maintaining the ambient temperature at 28°C through a continuous air-flow incubator (Neftek). To minimize movements during image acquisition, approximately 300 μL of tricaine was added to the Petri-dish in order to anesthetize embryos at 19 hpf or later. A multiphoton laser was used to excite at 760

nm, and emission was collected with two band pass filters between 450-480 nm and 510-540 nm, respectively. Figure 4.5 illustrates the ratiometric data for selected development stages in form of projections of high-resolution z-stacks that were acquired with 5 µm spacing.

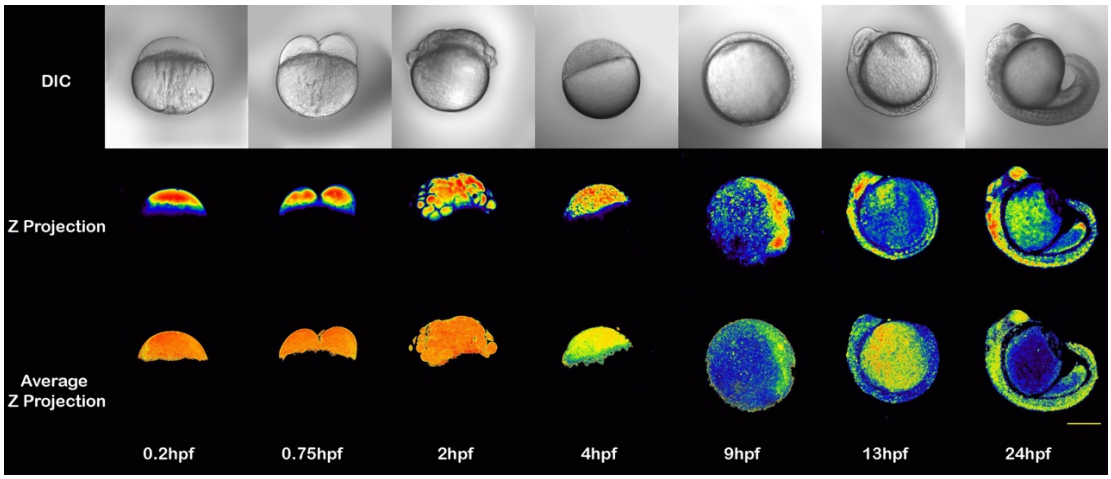

Figure 4.5: Ratiometric imaging of labile Zn(II) pools during the first 24 hours of zebrafish embryogenesis. Each false color image represents a projection using 5 µm ratiometric image slices of a unique embryo (excitation: 760 nm, channels: 450-480 nm and 510-540 nm). DIC: Differential Interference Contrast, projected light image; Z Projection: Average ratio across the entire z-stack, Intensity-corrected z-projection: a corrected average ratio was determined based on the number of z-slices that contained ratiometric data above the noise-threshold. Ratios increase in the order blue-green-yellow-orange-red. Scale bar: 300 µm (hpf = hours post fertilization).

Chromis1-dextran is membrane impermeable and is therefore contained within the blastodisc located at the animal pole of the embryo (0.2 hpf). The projections revealed a homogenous distribution during the zygote that continues through the early stages of embryogenesis. This is consistent with the rapid cell division that occurs during the development of the blastocyte that does not involve a significant change in cell cluster volume. As the cell divides, the probe is evenly distributed into the two daughter

cells (0.75 hpf). The intensity corrected projections reveal a ratio that corresponds to full saturation of the probe, suggesting the presence of a readily available Zn(II) pool that is buffered significantly above the probe's binding affinity. During the late blastula (4 hpf) to early gastrula (5 hpf) period, the high probe saturation and even ratio distribution are no longer observed. During epiboly, which is characterized by a coordinated cell movement around the yolk (9 hpf), distinct areas of higher fractional Zn(II) saturation of the probe appear. Finally, during the segmentation period, starting around 13 hpf, localized pools appear distributed over the entire animal body. Detailed quantitative analysis of the ratiometric data revealed that the fractional saturation of the probe significantly decreased over the first 24 hours, with an average ratio change from 1.1 at the single-cell stage to 0.8 at 24 hpf (Figure 4.6).

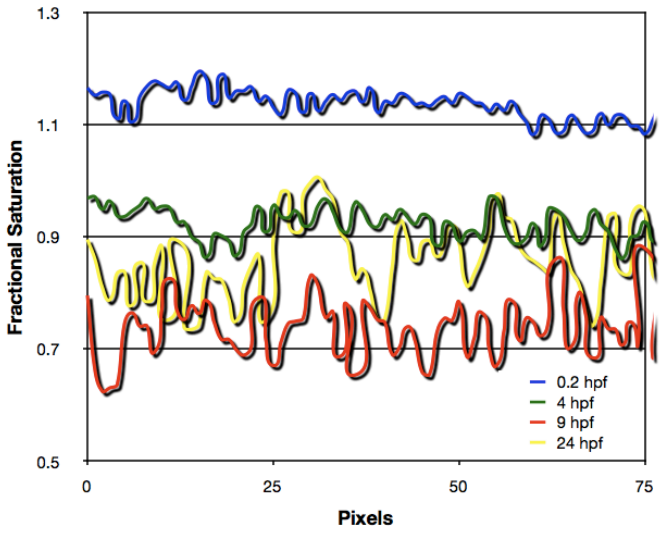

Figure 4.6: Variations in Zn(II) saturation over time. High-resolution stacks were imaged (Figure 4.5) and the ratio was calculated on a pixel-by-pixel basis using ImageJ software and the Average Z Projection images. Four major stages of development are represented here. For these four stages the following average ratios were calculated: 0.2 hpf : 1.12, 4 hpf : 0.95, 9 hpf : 0.81, and 24 hpf : 0.85. Overall, the average ratio decreased from approximately 1.1 - 0.8 over the first 24 hours of development.

4.2.3 Live Imaging of Zn(II) Redistribution During Embryogenesis

To test whether it would be possible to follow the development of the same embryo over an extended time period, ratiometric image stacks composed of 22 frames in 5 minute intervals were acquired over 14 hours, corresponding to a total of more than 3600 individual two-photon scans (Figure 4.7).

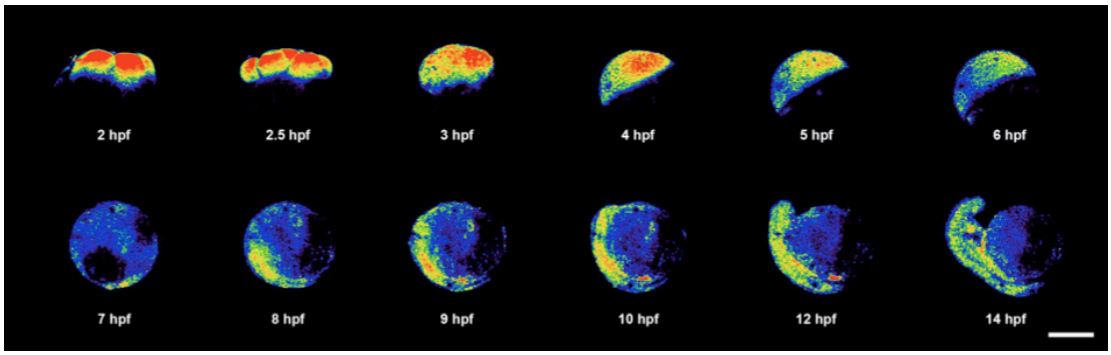

Figure 4.7: Redistribution of labile Zn(II) pools in the course of zebrafish embryogenesis. Chromis1-dextran was injected into a fertilized embryo. A total of 3600 frames (145 stacks) were acquired over 14 hours with two-photon excitation at 760 nm. Each false color image represents a projection of 25 emission ratiometric images (channels: 450-480 nm and 510-540 nm). The labels refer to hours post fertilization (hpf). Ratios increase in the order blue-green-yellow-orange-red. Scale bar: 400 µM.

Similarly to the individual high-resolution stacks, the time-lapse imaging revealed labile zinc appears evenly distributed throughout early developmental stages. As the embryo further develops there is a clear compartmentalization of labile zinc in different regions of the developing fish. Additionally, due to the low-energy excitation at 760 nm, no noticeable damage to the embryo was observed. Furthermore, the fluorescence signal after 14 hours was comparable to previous experiments in individual embryos were imaged at a single developmental stage (Figure 4.5), indicating negligible photodecomposition of the probe.

4.3 Conclusions

Chromis1-dextran permits the dynamic imaging of labile Zn(II) pools in live, developing zebrafish embryos. The live microscopy provided high-resolution images without harming the zebrafish or photobleaching the probe, rendering long acquisition times with a single embryo. Zinc concentrations were evenly distributed throughout the cell during the early stages of embryogenesis, appearing to fully saturate Chromis1 in the single cell. Throughout development there appears to be a redistribution supplying zinc to areas of the zebrafish with a higher demand.

4.4 Materials and Methods

4.4.1 Zebrafish Maintenance and Husbandry

Adult wild-type zebrafish were housed and mated under standard laboratory conditions. Crosses were prepared with 2 males and 2 females separated by a divider. After roughly 16 hours in the crossing tanks the dividers were removed and the zebrafish were allowed to mate. Fertilized embryos fall to the bottom of the mating tank, below a grate. After roughly 100 embryos were deposited, the zebrafish were returned to their storage tanks and the newly fertilized embryos were collected with a net and transported to a portable dish. Fertilized embryos were harvested and kept in E3 medium (5 mM NaCl, 0.17 mM KCl, 0.4 mM $CaCl_2$ and 0.16 mM $MgSO_4$) at 28.5°C.

4.4.2 Live Fluorescence Imaging of Chromis1 in Zebrafish

Collected zebrafish embryos were microinjected with approximately 4 nL of a 1 mM stock of Chromis1-dextran solution prepared in physiological buffer (pH 7.2 HEPES, 0.1 M KCl). Embryos where stabilized in a gel made from low melting agarose poured into a glass bottom dish. Holes were cut into the agarose for the embryo to stay while imaging and 0.02% Tricaine was used to anesthetize the embryos when they were old enough to move. Embryos were maintained in ambient temperature at 28°C through a continuous air-flow incubator (Neftek) or incubation chamber mounted on to the microscope.

The commercially purchased Ethylenediaminetetraacetic acid (EDTA), a metal chelator, was utilized to perform a titration on in vivo. Wild type zebrafish embryos were injected with a 1:1 mixture of Chromis1-dextran and varying concentrations of EDTA solutions. EDTA stock solutions of 200 mM, 400 mM, and 600 mM were individually mixed with one part Chromis1-dextran (1.18 mM) and subsequently injected (4 nL) into embryos at the single cell stage. Assuming a cell volume of approximately 70 nL, the intracellular concentration of EDTA is estimated to be 3, 6, and 9 mM respectively, an amount that is much higher than the approximate intracellular concentration of Chromis1-dextran (50 μM).

4.4.3 Image Processing

The quantitative image analysis software package, Image J,[31] was used to analyze the change in the fluorescence emission ratio of Chromis1 over time.

4.5 Literature Cited

1. Plum, L.M., Rink, L. & Haase, H. The essential toxin: Impact of zinc on human health. *International Journal of Environmental Research and Public Health* **7**, 1342-1365 (2010).

2. MacDonald, R.S. The role of zinc in growth and cell proliferation. *Journal of Nutrition* **130**, 1500S-1508S (2000).

3. Ho, E., Dukovcic, S., Hobson, B., Wong, C.P., Miller, G., Hardin, K., Traber, M.G. & Tanguay, R.L. Zinc transporter expression in zebrafish (Danio rerio) during development. *Comparative Biochemistry and Physiology C-Toxicology & Pharmacology* **155**, 26-32 (2012).

4. Bourassa, D., Gleber, S.C., Vogt, S., Yi, H., Will, F., Richter, H., Shin, C.H. & Fahrni, C.J. 3D imaging of transition metals in the zebrafish embryo by X-ray fluorescence microtomography. *Metallomics* **6**, 1648-1655 (2014).

5. Westerfield, M. *The zebrafish book. A guide for the laboratory use of zebrafish (Danio rerio)*, (University of Oregon Press, Eugene, 2000).

6. Miyares, R.L., de Rezende, V.B. & Farber, S.A. Zebrafish yolk lipid processing: a tractable tool for the study of vertebrate lipid transport and metabolism. *Disease Models & Mechanisms* **7**, 915-927 (2014).

7. Kane, D.A. Cell cycles and development in the embryonic zebrafish. *Methods in Cell Biology, Vol 59: Zebrafish: Biology* **59**, 11-26 (1999).

8. Kimmel, C.B., Ballard, W.W., Kimmel, S.R., Ullmann, B. & Schilling, T.F. Stages of embryonic-development of the zebrafish. *Developmental Dynamics* **203**, 253-310 (1995).

9. Goldsmith, J.R. & Jobin, C. Think small: Zebrafish as a model system of human pathology. *Journal of Biomedicine and Biotechnology* (2012).

10. Ignatius, M.S. & Langenau, D.M. Fluorescent imaging of cancer in zebrafish. *Zebrafish: Disease Models and Chemical Screens, 3rd Edition* **105**, 437-459 (2011).

11. Katoh, Y., Sato, T. & Yamamoto, Y. Determination of multielement concentrations in normal human organs from the Japanese. *Biological Trace Element Research* **90**, 57-70 (2002).

12. Ma, S.M., Lee, S.G., Kim, E.B., Park, T.J., Seluanov, A., Gorbunova, V., Buffenstein, R., Seravalli, J. & Gladyshev, V.N. Organization of the mammalian ionome according to organ origin, lineage specialization, and longevity. *Cell Reports* **13**, 1319-1326 (2015).

13. Webb, S.E., Lee, K.W., Karplus, E. & Miller, A.L. Localized calcium transients accompany furrow positioning, propagation, and deepening during the early cleavage period of zebrafish embryos. *Developmental Biology* **192**, 78-92 (1997).

14. Webb, S.E. & Miller, A.L. Calcium signalling during embryonic development. *Nature Reviews Molecular Cell Biology* **4**, 539-551 (2003).

15. Webb, S.E. & Miller, A.L. Imaging intercellular calcium waves during late epiboly in intact zebrafish embryos. *Zygote* **11**, 175-182 (2003).

16. Kettunen, P. Calcium Imaging in the Zebrafish. *Calcium Signaling* **740**, 1039-1071 (2012).

17. Sharma, D. & Kinsey, W.H. Regionalized calcium signaling in zebrafish fertilization. *International Journal of Developmental Biology* **52**, 561-570 (2008).

18. Chang, D.C. & Lu, P. Multiple types of calcium signals are associated with cell division in zebrafish embryo. *Microscopy Research and Technique* **49**, 111-122 (2000).

19. Reinhard, E., Yokoe, H., Niebling, K.R., Allbritton, N.L., Kuhn, M.A. & Meyer, T. Localized calcium signals in early zebrafish development. *Developmental Biology* **170**, 50-61 (1995).

20. Ma, D.L., He, H.Z., Zhong, H.J., Lin, S., Chan, D.S.H., Wang, L., Lee, S.M.Y., Leung, C.H. & Wong, C.Y. Visualization of Zn2+ ions in live zebrafish using a luminescent iridium(III) chemosensor. *Acs Applied Materials & Interfaces* **6**, 14008-14015 (2014).

21. Liu, Z.P., Zhang, C.L., Chen, Y.C., Qian, F., Bai, Y., He, W.J. & Guo, Z.J. In vivo ratiometric Zn2+ imaging in zebrafish larvae using a new visible light excitable fluorescent sensor. *Chemical Communications* **50**, 1253-1255 (2014).

22. Xu, Z., Baek, K.-H., Kim, H.N., Cui, J., Qian, X., Spring, D.R., Shin, I. & Yoon, J. Zn2+-Triggered amide tautomerization produces a highly Zn2+-selective, cell-permeable, and ratiometric fluorescent sensor. *Journal of the American Chemical Society* **132**, 601-610 (2010).

23. Qian, F., Zhang, C.L., Zhang, Y.M., He, W.J., Gao, X., Hu, P. & Guo, Z.J. Visible light excitable Zn2+ fluorescent sensor derived from an intramolecular charge transfer fluorophore and its in vitro and in vivo application. *Journal of the American Chemical Society* **131**, 1460-1468 (2009).

24. Ko, S.K., Chen, X., Yoon, J. & Shin, I. Zebrafish as a good vertebrate model for molecular imaging using fluorescent probes. *Chemical Society Reviews* **40**, 2120-2130 (2011).

25. Strehlow, D. & Gilbert, W. A fate map for the first cleavages of the zebrafish. *Nature* **361**, 451-452 (1993).

26. Woo, K., Shih, J. & Fraser, S.E. Fate maps of the zebrafish embryo. *Current opinion in genetics & development* **5**, 439-443 (1995).

27. Köbbert, C., Apps, R., Bechmann, I., Lanciego, J.L., Mey, J. & Thanos, S. Current concepts in neuroanatomical tracing. *Prog Neurobiol* **62**, 327-51 (2000).

28. Vercelli, A., Repici, M., Garbossa, D. & Grimaldi, A. Recent techniques for tracing pathways in the central nervous system of developing and adult mammals. *Brain Res. Bull.* **51**, 11-28 (2000).

29. Fetcho, J.R. & Omalley, D.M. Visualization of active neural circuitry in the spinal-cord of intact zebrafish. *Journal of Neurophysiology* **73**, 399-406 (1995).

30. Riggio, M., Filosa, S., Parisi, E. & Scudiero, R. Changes in zinc, copper and metallothionein contents during oocyte growth and early development of the teleost Danio rerio (zebrafish). *Comparative Biochemistry and Physiology C-Toxicology & Pharmacology* **135**, 191-196 (2003).

31. Schneider, C.A., Rasband, W.S. & Eliceiri, K.W. NIH Image to ImageJ: 25 years of image analysis. *Nature Methods* **9**, 671-675 (2012).

CHAPTER 5

CONCLUSIONS AND FUTURE DIRECTIONS

5.1 Probing Labile Zinc Pools in Proliferating Cells

5.1.1 Adjusting the Affinity of Chromis1

As indicated in Chapter 2, no significant changes in labile Zn(II) were detected in dividing 3T3 cells using Chromis1-ester. Both the distribution pattern of total zinc and the 2 to 3-fold increase of zinc observed in the SXRF experiments[1] were absent in labile Zn(II) imaging. These results indicate the influx of Zn(II) observed in SXRF microscopy data is likely bound to ligands with a higher affinity than the Zn(II)-selective fluorescent probe, Chromis1-ester. In order to image the influx of Zn(II) during cell division, higher affinity Zn(II)-selective probes must be used. Efforts of this nature are already underway. Derivatives of Chromis1-ester have been designed and are currently being characterized in solution and in cell culture (Figure 5.1).

5.1.2 Identifying Key Zn(II) Transporters During Mitosis

To further study metal distribution during mitosis, cell populations should be synchronized. Cell synchronization methods such as the Double Thymidine Block or Serum Starvation could interfere with Zn(II) homeostasis, therefore these techniques should be avoided. Alternatively, synchronization using mechanical separation via cellular elutriation is an effective method to isolate mitotic cells without interfering with Zn(II) regulation. Synchronized populations of cells can then be evaluated using mass spectrometry or western blotting approaches to determine if any zinc transporters (ZIPs or ZnTs) are up-regulated as a function of the cell cycle. If so, these specific transporters can be inhibited then SXRF microscopy can be used on individual cells to determine if

these transporters affect the distribution pattern or influence the uptake of zinc during mitosis. For example, zinc transporters ZIP6 and ZIP10 have been identified as two of the most abundantly expressed transporters in an oocyte and are required components of oocyte maturation in meiosis.[2] To determine if ZIP6 and ZIP10 play an important role in mitosis as well, antibodies can target and block these zinc transporters potentially altering zinc homeostasis during cell division. These cells can then be imaged using SXRF microscopy to determine if the absence of function from these specific zinc transporters effect the zinc influx prior to mitosis or the zinc distribution pattern in the individual cell.

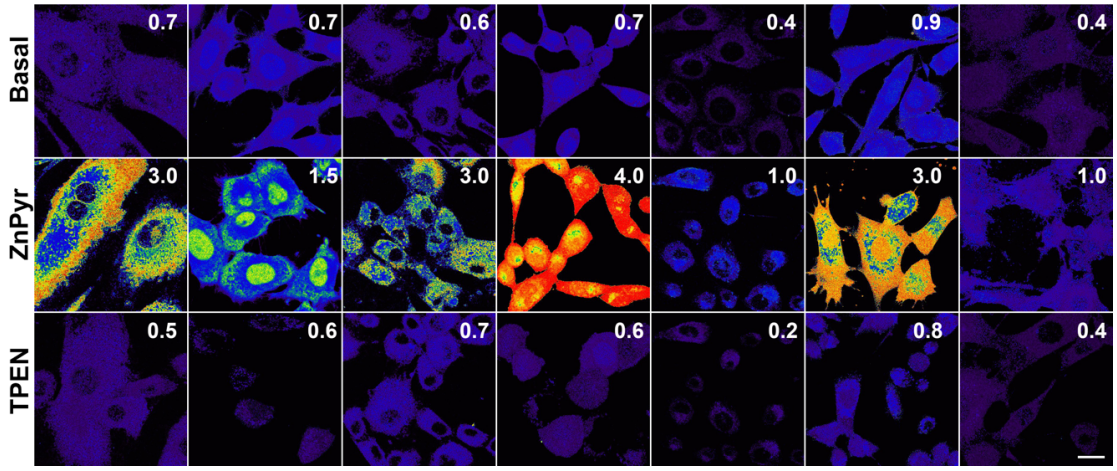

Figure 5.1: Detecting labile Zn(II) using various Chromis1 derivatives. Cells were treated with various Chromis1 derivatives. The first column is Chromis1-ester, the second column is Chromis1-AM ester, and the remaining 5 columns are derivatives with unpublished structures. Ratio scale is from 0 – 4.0 for all images. Cells were imaged in basal conditions (top row), followed by perfusion of 100 μM $ZnSO_4$: 10 μM pyrithione (middle row) and finally 100 μM TPEN (bottom row). The various derivatives have different binding affinities and therefore result in different reported ratio changes even when introduced to a constant concentration of exogenous zinc or TPEN.

5.2 3D Imaging of Transition Metals in the Zebrafish Embryo by SXRF

5.2.1 Improved SXRF Microtomography Using Kirkpatrick-Baez Mirror Optics

The beamline, 2-ID-E (Advance Photon Source, Argonne National Laboratory, Argonne, IL), used to collect the original X-ray fluorescence data of the 24 and 48 hpf zebrafish embryos has limitations restricting the possible resolution. While this system offers highly focused optics allowing for high spatial resolution of a typical sample, the photon flux is limited. Therefore, larger biological samples such as a zebrafish embryo is unable to utilize this high spatial resolution. To achieve a higher resolution possible at 2-ID-E would require inhibitive long data acquisition times. For this reason, the 24 hpf embryo required 2-3 μM step sizes despite the beam focused to 300 nm, consequentially under-sampling the elemental content. Using a larger sample such as the 48 hpf embryo resulted in an even lower signal to noise ratio and longer data acquisition times. The copper data collected for this sample had such a high signal to noise ratio, the information was unusable. For these reasons, the micro-focusing Kirkpatrick-Baez (K-B) mirror optics are a suitable solution. The two curved mirrors of the K-B optics system work to directly focus the beam and allow for a tunable spot size to achieve optimum focus at different wavelengths.[3] This optical configuration allows the user access to optimize the final focus spot in order to establish either high flux or ultimate spatial resolution. The 13-ID-E beamline of the Argonne National Lab is equipped with K-B mirror optics and incorporates an advanced direct-drive rotary stage with an air-bearing and ferro-fluid seal to provide a frictionless, ultra-smooth and precise movement of the sample which is critical for microtomography.

To demonstrate the advantages of using the K-B mirror optics for our larger samples, a tomographic data set of a 24 hpf embryo was collected on the 13-ID-E beamline. Transverse brain sections from reconstructions of 24 hpf embryos collected

using both 2-ID-E (A) and 13-ID-E (B) are compared in Figure 5.2. The level of detail and clarity offered from the 13-ID-E beamline using the K-B mirror optics is apparent by eye. While the lobes and ventricles of the brain can be distinguished in the 2-ID-E data set obtained via Fresnel zone plate, the optic cup and lens are hardly noticeable at all. The K-B mirror optics offer clear separation of the various lobes and ventricles of the brain. In Figure 5.2, the diencephalon, mesencephalon, cerebellum, third ventricle and fourth ventricle are well established. Furthermore, the level of detail seen in the optic cup and lens of the eye is significantly improved. The resolution offered using the K-B mirror optics offers a more detailed look into the anatomy of the zebrafish embryo using x-ray fluorescence.

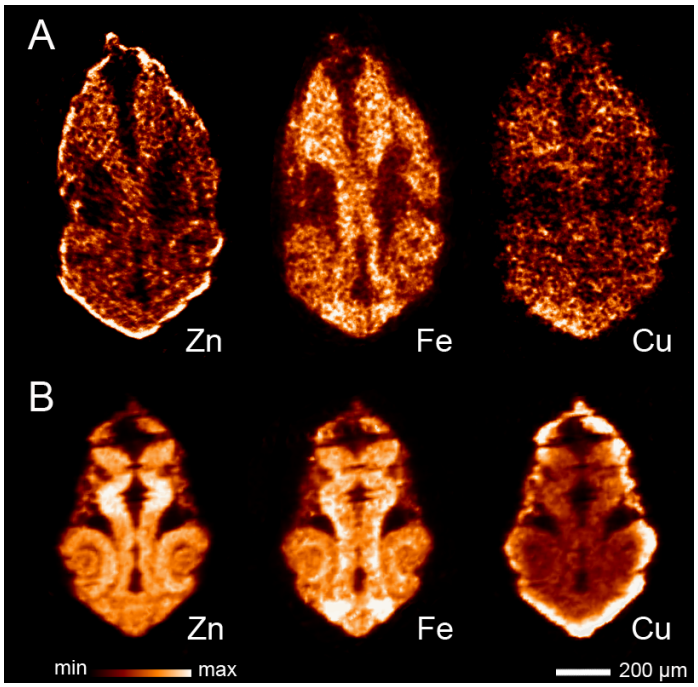

Figure 5.2: Comparison of Fresnel zone plate and K-B mirror optics demonstrated via transverse sections of the zebrafish brain, 24 hpf. **A:** Data collected using the 2-ID-E beamline with Fresnel zone plate. While some anatomical features can be distinguished, the signal to noise ratio interferes with observing details. **B:** Data collected using the 13-ID-E beamline with K-B mirror optics permits imaging clear details of anatomical features.

These methods should also be used to detect the total zinc throughout all stages of development to create a further understanding of the metal distribution throughout the first few days of embryogenesis. Previous attempts to prepare early stage embryos for SXRF microscopy using PLT methods described in Chapter 3 failed. The embryos can not be dechorionated at early stages, leaving the chorion to fold into the embryo during the processes. Additionally, the fragile embryos fall apart. Sample preparation techniques must be further developed in order to perform SXRF microtomography on early stage embryos.

5.2.2 Investigating the Increased Zinc Levels in the Zebrafish Retina

The zebrafish retina is a prominent feature observed in both the total zinc maps of the SXRF reconstructions (Chapter 3) and the labile zinc distribution using Chromis1-dextran (Chapter 4). Numerous ZIP and ZnT transporter proteins have been identified in the retina. ZIP1, ZIP2, ZIP3, ZIP4, ZIP12, ZnT3, ZnT6 and ZnT7 have all been identified in human retinal pigment epithelium (RPE) cells.[4,5] In addition to ZnT3, ZnT6, and ZnT7, ZnT8 and Metallothionein are found throughout many other layers of the retina in both mouse and human models.[4,5] Using Chromis1-dextran with zebrafish models containing morpholino knockdowns of individual zinc transporters, key transporters can be identified. These knockdown models could also be used in SXRF microtomography to determine a change in total zinc versus labile zinc as seen with Chromis1-dextran. Understanding zinc homeostasis in the retina can lead to a better understanding of zinc's role in the vision cycle and how this process is regulated.

5.2.3 Investigating the Increased Total Zinc Levels in the Zebrafish Tail Bud

Sagittal sectioning of the reconstructed 3D metal distribution maps of the zebrafish embryo 24 hpf revealed a distinct accumulation of zinc at the tip of the tail, mostly localized to peripheral cell layers (Chapter 3, Figure 3.10).[6] This area exhibits the highest concentration of zinc within the embryo, raising the question of what is occurring in the tip of the tail during this stage of development that requires so much zinc?

The zebrafish body develops in an anterior-to-posterior progression.[7,8] It is also believed that a population of stem cells resides in the tail bud.[9] How these unspecified cells determine their fate during development is unknown. Interestingly, the high concentration of zinc and copper is observed at the tip of the tail where these proposed stem cells are located during a time (24 hpf) the tail is undergoing much of its development.

A possible approach in the investigation of the zinc and copper at the tail bud involves exploring the relationships these transition metals have with the canonical Wnt signaling pathway. Canonical Wnt signaling has many roles in embryogenesis including acting as a critical component in the posterior development of the vertebrate embryonic body.[10,11] This signaling pathway affects the progenitor cell differentiation occurring at the tip of the tail.[12] The proteins involved in this pathway are specifically expressed in the tail bud, in the same region the increased concentrations of zinc and copper are observed. By performing SXRF microtomography on transgenic zebrafish lacking function of the Wnt pathway[12] a possible link with zinc and copper could be determined.

5.3 Correlating Zn(II) Distribution with Proliferating Cells During Embryogenesis

To further investigate the temporal changes of both labile and total metal compared to areas of proliferating activities in a developing zebrafish, zinc, iron and copper reconstructions can be compared to the cell-cycle progressions in a single embryo. To do so, the non-invasive Fluorescence Ubiquitination Cell Cycle Indicator (FUCCI) developed by Miyawaki and coworkers can be utilized to identify cells in specific stages of the cell cycle.[13] The FUCCI system takes advantage of a fluorescent protein based sensor using fluorescent markers fused to different regulators of the cell cycle, Cdt1 and geminin. These two regulators are complementary in their production and degradation throughout the cell cycle. By tagging Cdt1 and geminin with red and green fluorescent proteins, respectively, their cell-cycle dependent oscillations can be followed in live cells. During the G1 phase of the cell cycle, geminin is proteolytically degraded allowing only Cdt1 tagged with the red fluorescent protein to be imaged. Conversely, Cdt1 is proteolytically degraded during the S, G2 and M phases allowing geminin tagged with green fluorescence to be imaged. During the G1/S transition both proteins are present in the cell yielding yellow fluorescent nuclei due to the overlay of the two fluorescent signals.[13]

Miyawaki and colleagues further developed the FUCCI system by creating a transgenic FUCCI zebrafish known as zFucci, granting the ability to examine cell cycle behavior in vivo.[14] This transgenic line of zebrafish begin FUCCI expression at approximately 12 hpf and allow the observation of dynamic patterns of cell-cycle progression in several parts of the developing embryo. This particular line of fish allows for use of both Chromis1-dextran and SXRF to compare the labile zinc pools, total zinc, and cell-cycle progression all in a single embryo.

As an initial approach, fish from the transgenic zFucci line Tg(EF1α:mAG-zGem(1/100)) expressing green fluorescence in S/G2/M phase nuclei and Tg(EF1α:mKO2-zCdt1(1/190)) expressing red fluorescence in G1 phase nuclei were

crossed to produce embryos containing both red and green fluorescence markers. Embryos were harvest and allowed 24 hours to develop. Embryos were imaged prior to fixation to identify cells in specific stages of the cell cycle in the 24hpf embryos (Figure 5.3). Lastly, the embryos were fixed in 4% paraformaldehyde overnight before undergoing low-temperature embedding and excision via femtosecond laser sectioning just as the previous samples were prepared.

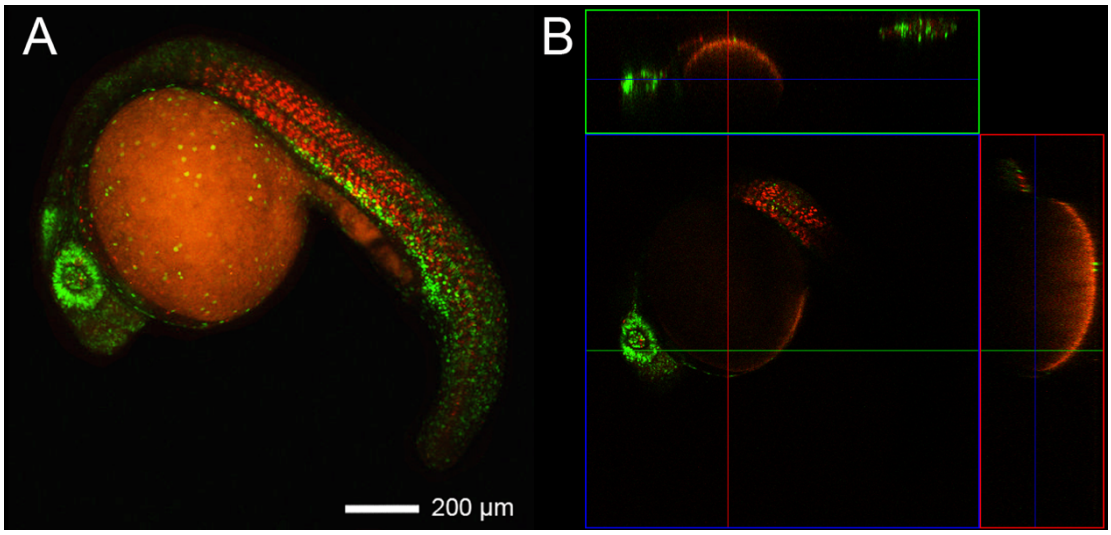

Figure 5.3: Transgenic zFucci imaging pre-fixation. Embryos were immediately fixed with 4% paraformaldehyde and underwent PLT methods in order to embed the embryos for SXRF microtomography. Expression level pattern in zFucci was limited by unexpected self-absorption which prevented imaging the entire fish.

5.4 Literature Cited

1. McRae, R., Lai, B. & Fahrni, C.J. Subcellular redistribution and mitotic inheritance of transition metals in proliferating mouse fibroblast cells. *Metallomics* **5**, 52-61 (2013).

2. Kong, B.Y., Duncan, F.E., Que, E.L., Kim, A.M., O'Halloran, T.V. & Woodruff, T.K. Maternally-derived zinc transporters ZIP6 and ZIP10 drive the mammalian oocyte-to-egg transition. *Molecular Human Reproduction* **20**, 1077-1089 (2014).

3. Kirkpatrick, P. & Baez, A.V. Formation of optical images by x-rays. *Journal of the Optical Society of America* **38**, 766-774 (1948).

4. Ugarte, M. & Osborne, N.N. Recent advances in the understanding of the role of zinc in ocular tissues. *Metallomics* **6**, 189-200 (2014).

5. Leung, K.W., Liu, M.G., Xu, X.M., Seiler, M.J., Barnstable, C.J. & Tombran-Tink, J. Expression of ZnT and ZIP zinc transporters in the human RPE and their regulation by neurotrophic factors. *Investigative Ophthalmology & Visual Science* **49**, 1221-1231 (2008).

6. Bourassa, D., Gleber, S.C., Vogt, S., Yi, H., Will, F., Richter, H., Shin, C.H. & Fahrni, C.J. 3D imaging of transition metals in the zebrafish embryo by X-ray fluorescence microtomography. *Metallomics* **6**, 1648-1655 (2014).

7. Martin, B.L. & Kimelman, D. Wnt signaling and the evolution of embryonic posterior development. *Current Biology* **19**, R215-R219 (2009).

8. Gomez, C., Ozbudak, E.M., Wunderlich, J., Baumann, D., Lewis, J. & Pourquie, O. Control of segment number in vertebrate embryos. *Nature* **454**, 335-339 (2008).

9. Wilson, V., Olivera-Martinez, I. & Storey, K.G. Stem cells, signals and vertebrate body axis extension. *Development* **136**, 1591-1604 (2009).

10. Schier, A.F. & Talbot, W.S. Molecular genetics of axis formation in zebrafish. *Annual Review of Genetics* **39**, 561-613 (2005).

11. Martin, B.L. & Kimelman, D. Regulation of canonical Wnt signaling by Brachyury is essential for posterior mesoderm formation. *Developmental Cell* **15**, 121-133 (2008).

12. Martin, B.L. & Kimelman, D. Canonical Wnt signaling dynamically controls multiple stem cell fate decisions during vertebrate body formation. *Developmental Cell* **22**, 223-232 (2012).

13. Sakaue-Sawano, A., Kurokawa, H., Morimura, T., Hanyu, A., Hama, H., Osawa, H., Kashiwagi, S., Fukami, K., Miyata, T., Miyoshi, H., Imamura, T., Ogawa, M., Masai, H. & Miyawaki, A. Visualizing spatiotemporal dynamics of multicellular cell-cycle progression. *Cell* **132**, 487-498 (2008).

14. Sugiyama, M., Sakaue-Sawano, A., Iimura, T., Fukami, K., Kitaguchi, T., Kawakami, K., Okamoto, H., Higashijima, S.I. & Miyawaki, A. Illuminating cell-cycle progression in the developing zebrafish embryo. *Proceedings of the National Academy of Sciences of the United States of America* **106**, 20812-20817 (2009).